2014

Scanning Probe Investigations of Magnetic Nanoparticles, Protein Binding and the Synthesis of Rare Earth Oxide Nanoparticles Using Nanoscale Lithography

Lauren Elizabeth Englade-Franklin
Louisiana State University and Agricultural and Mechanical College, lengla5@lsu.edu

SCANNING PROBE INVESTIGATIONS OF MAGNETIC NANOPARTICLES, PROTEIN BINDING AND THE SYNTHESIS OF RARE EARTH OXIDE NANOPARTICLES USING NANOSCALE LITHOGRAPHY

A Dissertation

Submitted to the Graduate Faculty of the
Louisiana State University and
Agricultural and Mechanical College
in partial fulfillment of the
requirements for the degree of
Doctor of Philosophy

in

The Department of Chemistry

by
Lauren Elizabeth Englade-Franklin
B.S., Louisiana Tech University, 2009
August 2014

ACKNOWLEDGMENTS

First, I give thanks to God for giving me the strength and the guidance necessary to complete this journey. The road on this path has been a trying one, but the Lord has given me the opportunity to learn and grow from this experience. He has provided me with the perseverance, character, and hope (Romans 5:3-4) I needed during this time and throughout my entire life. “I can do all things through Christ who strengthens me.” (Philippians 4:13)

Second, I’d like to thank my advisor, Dr. Jayne C. Garno. She has truly given me the encouragement, inspiration, and guidance needed during my time at LSU. I’d like to thank her for affording me the opportunity to work in her group, and for playing an instrumental role in my academic success. She is truly a woman who cares about the success of her students. I’d also like to thank Dr. Julia Chan, my collaborator and committee member. She has been a blessing as both a mentor and a role model during my graduate career. Thank you to my committee members Dr. Justin Ragains, Dr. Georgios Veronis, and Dr. Donghui Zhang for reviewing my dissertation and providing valuable feedback.

To the Garno group (both past and present), the blood, sweat, and tears we shared will always be held close to my heart. It was truly a pleasure to work for a group with such a nurturing and collaborative spirit. I will miss all of the tailgates, lunches, group parties, and conference trips we’ve shared over the years. I hope to stay in touch with each of you, and wish you all the success in the future. Specifically, I like to acknowledge my colleagues, Dr. Tian Tian, Dr. Gregory Morrison, Dr. ChaMarra Saner, and Dr. Kathie Lusker. Each of you has played an integral role in my research in some way, and for that I will be forever grateful. More importantly, you have each become a friend, and I can’t express how much this means to me personally.

To my parents Mary Lubrano and David Englade, I must say thank you for always putting up with me! Your love and support have led me to where I am today. Mom, you are the strongest woman I have ever met. Thank you for always standing up for what is right, and being the amazing role model you are. You've always been there for me, and I can't tell you how much I love you. Dad, you have pushed me to always succeed and never give up. Thank you for teaching me what is worth fighting and working for in life, I love you. I would also like to thank my siblings and step parents, Raymond Lubrano, Laura Ladner, Hannah Ryan, Riley Englade, and Ray Ray Lubrano. The good times and smiles you give me keep me positive when times get tough. To my unborn sibling Peanut (Kinsley Englade), I can't wait to make these same happy memories with you. Laughter and happiness from you all are the hope that keeps me motivated. To my in-laws, grandparents, aunts and uncles, and cousins, your support and prayers have kept me going through this time and I can't thank you enough for always being there for me. Your wisdom and love have been an invaluable asset to my success. I can't express how much I enjoy having such a large and loving family.

Finally, I would like to express my gratitude and love to my amazing husband, CJ Franklin. You truly do possess the patience of Job. Your acceptance and support over the last five years has kept me on the right path. Thank you for always believing in me when I lost faith in myself. All of your sacrifices have not gone unnoticed, and I want to acknowledge and thank you for allowing me to achieve my dreams. You are not just my husband and partner, but also my best friend. I love you.

TABLE OF CONTENTS

LIST OF TABLES

LIST OF FIGURES

LIST OF ABBREVIATIONS

ABBREVIATION	NAME
AFM	Atomic force microscopy
AC-AFM	Alternating contact atomic force microscopy
FFT	Fast Fourier transform
MAC mode	Magnetic AC mode
MPTMS	Mercaptoproplytrimethoxysilane
MSM-AFM	Magnetic sample modulation atomic force microscopy
OTS	Octadecyltrichlorosilane
PEG silane	2-[Methoxy-(polyethyleneoxy)propyl] trichlorosilane
REO	Rare earth oxide
SAM	Self-assembled monolayer
SEM	Scanning electron microscopy
SPM	Scanning probe microscopy
STM	Scanning tunneling microscopy
TEM	Transmission electron microscopy
XRD	X-ray diffraction
YTCA	Yttrium trichloroacetate

ABSTRACT

Approaches to prepare spatially selective surfaces were developed in this dissertation for constructing assemblies of biomolecules and inorganic materials. Nanoscale surface patterns of organic thin films were prepared using particle lithography combined with organosilane chemistry. Biological and inorganic nanomaterials can be patterned with tailorable periodicities, which can be controlled by selecting the diameter of mesospheres used as surface masks. The surface platforms of well-defined nanopatterns are ideal for high resolution investigations using scanning probe microscopy (SPM). Local measurements of surface properties combined with visualization of the steps of chemical reactions at the molecular level were accomplished.

Fundamental studies of the chemical steps for patterning proteins are critical for the integration of biomolecules into miniature biological-electronic devices for protein sensing. Rare earth oxide (REO) nanomaterials have useful properties such as upconversion, catalysis, and magnetism. For commercial applications REO nanomaterials should have well defined sizes and be arranged as surface arrays.

Sample characterizations were accomplished with selected modes of SPM. Scanning probe studies can be used to probe the morphological and physical properties of samples, when discrete arrangements of nanomaterials are prepared. Atomic force microscopy (AFM) can be used to analyze many types of samples in ambient and liquid environments. Arrays of protein nanopatterns were fabricated using the spatial selectivity of chemical patterns prepared with particle lithography. The steps for patterning protein and protein binding were visualized with AFM. The protein arrays were tested for the selectivity of binding IgG to evaluate if protein function was retained.

Studies were conducted with selected systems of inorganic and magnetic nanoparticles using SPM. Synthesis of rare earth nanoparticles was accomplished using a novel approach with organosilane surface templates. Surface changes during the steps of crystallization and solid state synthesis were captured using AFM. The magnetic sample modulation (MSM) mode of AFM was used to characterize the vibrational response of magnetic nanoparticles to externally applied electromagnetic fields. An investigation of nanoparticle size versus the amplitude of oscillation response was measured with MSM-AFM. Approaches for high-throughput patterning of biomolecules and nanoparticles as well as a method for the template-directed synthesis of rare earth oxide materials will be described.

CHAPTER 1: INTRODUCTION

Approaches were developed in this dissertation to prepare spatially selective surfaces for constructing assemblies of biomolecules and inorganic materials by combining particle lithography with molecular self-assembly. The surface platforms are potentially useful for applications as biosensors, surface supported catalysts, optical filters, and light emitting arrays. The patterned arrays also serve as test platforms for fundamental investigations of newly designed materials using atomic force microscopy (AFM). With particle lithography, the spacing between nanopatterns is controlled by selecting the diameter of mesospheres used as surface masks. Measurements with AFM provide molecular-level views of nanostructures and insight into the processes of chemical assembly and surface binding.

1.1 Nanoscale studies using scanning probe microscopy (SPM)

The scanning probe microscope (SPM) has been used for imaging and measurements at the nanoscale since 1981.[1] Images of the atomic detail of nanoscale materials has been useful for applications in biology,[2, 3] materials science,[4, 5] and molecular electronics.[6, 7] Since its invention, developments for SPM instrumentation have advanced and now encompass more than 50 different modes for imaging and measurements. Newer SPM modes provide capabilities of probing not only morphology, but also electronic and spectral properties of nanomaterials. *In situ* measurement modes can be used for time-resolved studies of molecules in selected environments. In Chapter 2, the history of SPM will be described as well as the operation for measurement modes used in this dissertation. Self-assembly and particle lithography will also be described as a means of preparing samples for AFM studies.

1.2 Dynamic measurements for imaging magnetic nanomaterials with AFM[8]

Magnetic sample modulation combined with contact mode atomic force microscopy (AFM) provides a sensitive way to detect the vibration of magnetic nanomaterials at the level of individual nanoparticles or ferroproteins. Rather than using a coated AFM probe as a magnetic sensor, our strategy is to use a non-magnetic probe for contact mode AFM to characterize the vibration of superparamagnetic nanomaterials responding to the flux of an AC electromagnetic field. We refer to this hybrid imaging and measurement mode as magnetic sample modulation AFM (MSM-AFM). An alternating electromagnetic field induces the actuation of magnetic and superparamagnetic nanomaterials that are attached to surfaces, and the AFM tip is used to detect the sample vibration. For MSM-AFM, an oscillating magnetic field is produced by applying an AC current to a wire coil solenoid placed under the sample stage. The AFM is configured for contact mode imaging, and the probe is scanned slowly across the vibrating samples. Selected parameters of frequency and magnetic field strength can be tuned to study dynamic changes in the vibrational response of samples.

1.3 Studies of the vibrational resonance of magnetic nanoparticles using MSM-AFM

Due to quantum confinement, nanoparticles exhibit unique physical and mechanical properties that are attributable to nanoscale dimensions as compared to the bulk materials. Studies of the magnetic response of metal nanoparticles were accomplished using a hybrid imaging approach of magnetic sample modulation AFM (MSM-AFM). These studies reveal how the composition and size of the nanoparticles affects their vibration in response to a magnetic field.

Nanoparticles of $FeNi_3$ prepared by microwave synthesis were characterized with tapping-mode atomic force microscopy (AFM) and X-ray diffraction. Studies of the magnetic

response of the nanoparticles were accomplished using MSM-AFM. The MSM imaging mode provides characterizations at the level of individual nanoparticles for detecting changes in vibrational resonance signatures in response to an AC electromagnetic flux, as well as revealing differences in vibration amplitude versus size. Results will be presented which demonstrate the measurement capabilities of MSM-AFM for characterizations of intermetallic nanoparticles of $FeNi_3$.

Cube shaped iron oxide nanoparticles were received from Argonne National Lab and imaged using atomic force microscopy. In Chapter 4 results from tapping-mode AFM characterizations of the nanoparticles will be presented along with magnetic mapping using MSM-AFM.

1.4 Fibrinogen nanopatterns prepared by ozone lithography with organosilanes[9]

An approach was developed based on particle lithography to prepare spatially selective surface platforms of organosilanes that are suitable for nanoscale studies of protein binding. Particle lithography was applied for patterning fibrinogen, a plasma protein that has a major role in the clotting cascade for blood coagulation and wound healing. Surface nanopatterns of mercaptosilanes were designed as sites for the attachment of fibrinogen within a protein resistant matrix of PEG-silane. Preparing site-selective surfaces was problematic in our studies, because of the self-reactive properties of PEG-organosilanes. Certain organosilanes presenting hydroxyl head groups will cross-react to form mixed surface multilayers. We developed a strategy with particle lithography using masks of silica mesospheres to protect small, discrete regions of the surface from cross reactions. Images acquired with AFM disclose that fibrinogen attached primarily to the surface areas presenting thiol head groups, which were surrounded by PEG-silane. The activity for binding anti-fibrinogen was further evaluated using *ex situ* AFM studies,

confirming that after immobilization the fibrinogen nanopatterns retained capacity for binding IgG. Studies with AFM provide advantages of achieving nanoscale resolution for detecting surface changes during steps of biochemical surface reactions, without requiring chemical modification of proteins or fluorescent labels.

1.5 New approach to synthesize nanoparticles of rare earth oxides

We introduce an approach to synthesize rare earth nanoparticles using high temperature reactions without aggregation of the nanoparticles. The dispersity of the nanoparticles is controlled at the nanoscale by using small organosilane molds as reaction containers. Zeptoliter reaction vessels prepared from organosilane self-assembled monolayers (SAMs) were used for the surface-directed synthesis of rare earth oxide (REO) nanoparticles. Nanopores of octadecyltrichlorosilane were prepared on Si(111) using particle lithography with immersion steps. The nanopores were filled with a precursor solution of erbium and yttrium salts to confine the crystallization step to occur within individual zeptoliter-sized organosilane reaction vessels. Areas between the nanopores were separated by a matrix film of octadecyltrichlorosilane. With heating, the organosilane template was removed by calcination to generate a surface array of erbium-doped yttria nanoparticles. Nanoparticles synthesized by the surface-directed approach retain the periodic arrangement of the nanopores formed from mesoparticle masks. While bulk rare earth oxides can be readily prepared by solid state methods at high temperature (>900 ^{o}C), approaches for preparing REO nanoparticles are limited. Conventional wet chemistry methods are limited to low temperatures according to the boiling points of the solvents used for synthesis. To achieve crystallinity of REO nanoparticles requires steps for high temperature processing of samples, which can cause self-aggregation and dispersity in sample diameters. The facile steps

for particle lithography address the problems of aggregation and the requirement for high temperature synthesis.

1.6 Synopsis

Particle lithography combined with self-assembly can be used to generate nanostructures with designed interfaces and sizes. The surface arrays demonstrated in this dissertation include nanoscale protein arrays, rare earth oxide arrays, magnetic nanoparticle platforms, and patterned surfaces of self-assembling molecules. For investigations using AFM, controlling the size and orientation of samples on surfaces provides advantages for nanoscale measurements. In Chapter 8, the main results of this dissertation are presented along with a discussion of future directions for research experiments.

CHAPTER 2: ATOMIC FORCE MICROSCOPY

2.1 Background and history of scanning probe microscopy

Scanning probe microscopy (SPM) is a technique used to obtain 3-D images of surface morphology and surface properties with high resolution. For modes of SPM, a sharp probe is scanned across a surface while interactions between the probe and the sample are measured and recorded as digital images. Surface properties that can be measured with SPM include magnetism, friction, elastic compliance, conductance, morphology, and spectroscopic properties.[10-14] The first SPM methods developed were scanning tunneling microscopy (STM)[1]and atomic force microscopy (AFM).[15]

The visualization of individual atoms and atomic vacancies within an atomic lattice was achieved with the invention of the STM by Binnig and Rohrer at IBM.[1, 16] Prior to 1981, the atomic structure of materials was only discernable through X-ray diffraction (XRD). Binnig and Rohrer won the Nobel Prize in physics in 1986 for this achievement. Today, STM is routinely used to image surfaces with atomic resolution.[17-19] The principle of STM is based on monitoring tunneling current between the sample and a sharp wire made of a conductive material, usually tungsten or a platinum alloy.[20] The tip is scanned at a discrete distance of 1-2 nm from the surface in "non-contact" mode. When a voltage is applied to the sample, electrons tunnel through the potential energy barrier and causes current to flow between the tip and sample during scanning. A map of sample topography can be generated by holding the current constant and tracking the tip as it moves vertically to compensate for changes in tunneling current due to local surface topography. The STM probe must be scanned extremely close to the sample surface because the probability of electron tunneling between the tip and sample exponentially decays as the tip-sample distance increases. While the distance-dependence provides high resolution with

STM, it has the limitation that measurements require atomically flat and conductive samples. The invention of AFM overcomes the limitation of requiring conductive surfaces.

The atomic force microscope was invented in 1986 by Binnig, Quate, and Gerber.[15] With AFM, diverse samples could be imaged with high resolution in ambient environments. Atomic resolution of a graphite surface was demonstrated using AFM in ambient air in 1987.[21] The operating principle of AFM is based on tracking the movement of a sharp tip as it is scanned in a raster pattern across a surface. The displacement of the probe is based on tip-surface interactions during a scan. The first AFM instrument was operated using a probe constructed of a small diamond glued to gold foil. As the diamond tip was raster scanned across the surface, the movement was monitored by measuring the tunneling current between the gold foil and another wire (in a manner similar to STM). In more recent instrument designs, an optical lever setup is used to monitor tip movement during a scan rather than tunneling current.[22, 23] Sub-angstrom resolution can be achieved with the optical deflection configuration when working with insulating samples and probes. The first commercial AFM instrument was released in 1988 by Park Scientific Instruments. The most commonly used tips for AFM are made from microfabricated silicon or silicon nitride.[24]

Characterizations with AFM have been applied for samples such as self-assembled monolayers (SAMs),[25, 26] polymers,[27, 28] nanoparticles,[29, 30] proteins,[31, 32] DNA,[33, 34] and cells.[35, 36] The resolution achieved with AFM is 0.1 nm for the x and y directions (depending on tip radius), and 0.01 nm in the z direction.[37-39] Unlike scanning electron microscopy (SEM) and transmission electron (TEM) which provide 2D maps of surface morphology, images acquired using AFM contain 3D topographical information about samples. For electron microscopy, samples must be coated with a conductive metal for imaging in vacuum environments, which limits the types of

samples that can be imaged. With AFM, any sample surface which is relatively flat can be imaged in ambient air, liquid environments or in vacuum, requiring little sample preparation. The AFM can be used for *in situ* investigations of the self-assembly of molecules in liquid environments.[40-42] The ability to probe and manipulate biological samples in a native liquid environment such as aqueous buffers with molecular resolution is useful for biochemical studies.[43]

2.2 Imaging principle of atomic force microscopy

For AFM measurements, a sample is characterized by scanning a sharp tip attached to a cantilever across the sample surface as shown in Figure 2.1. Interactions between the probe and the sample will cause the tip to deflect and twist, these forces change the deflection of the laser signal and can be monitored using a position sensitive detector. Images are generated by plotting voltage changes of cantilever deflection versus the position of the tip.

The tips for AFM characterizations have specific shapes, spring constants, and composition depending on the selected measurement mode. Tips are chosen based on the type of sample to be probed and the tip-sample interaction under investigation. The tips most commonly used for AFM imaging are made of Si or Si_3N_4. Digital AFM images are a convolution of the geometry of both the sample and tip. The dimensions of the tip will generally define the lateral resolution of the AFM image.[44, 45] The effects of tip-sample convolution can be minimized by using a sharp AFM probe or by using deconvolution algorithms.[46, 47] Commercially available tips have diameters of 5-40 nm and are manufactured using microfabrication technologies. Etching processes can be used to make Si and Si_3N_4 tips with 5 nm diameter. For high resolution imaging of individual proteins, carbon nanotubes have been attached to the apex of the tip.[48] Typical

diameters of carbon nanotube tips are 2 nm, however are limited to investigations in tapping-mode.[48]

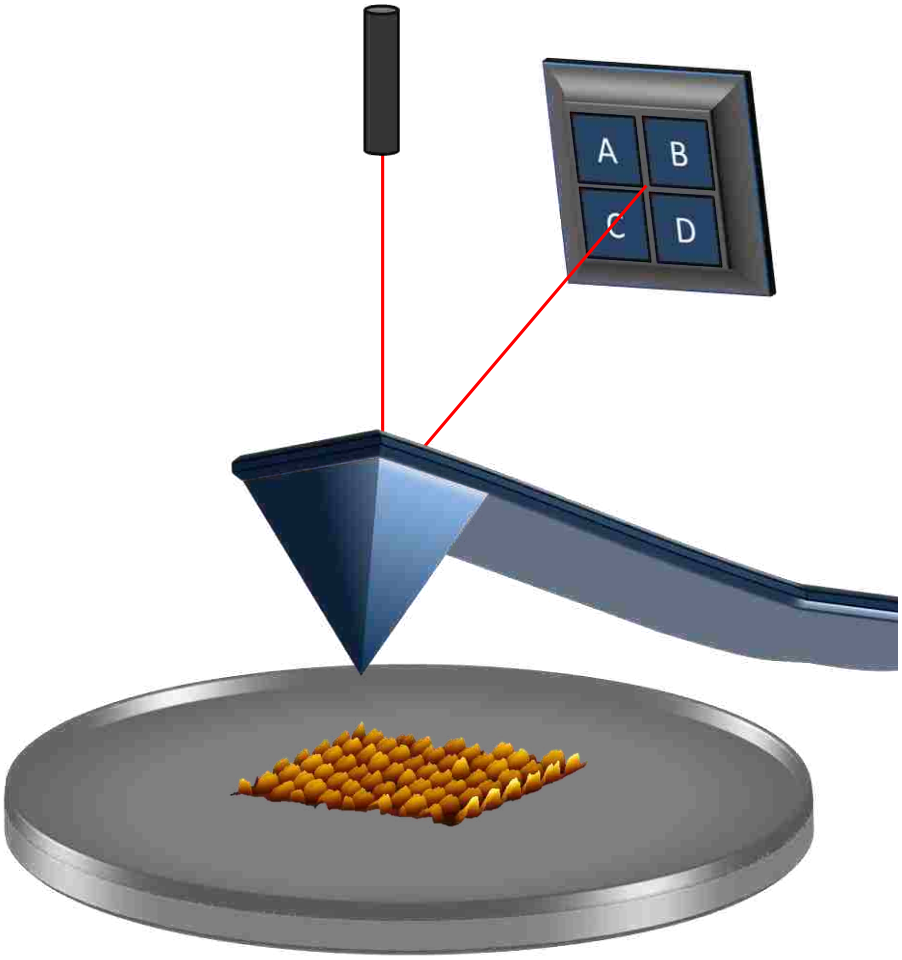

Figure 2.1 Operation of the atomic force microscope shown with optical lever setup.

The movement of an AFM tip across the sample in the x, y, and z directions is controlled through a piezoceramic transducer. When the tip is mounted on the piezotube, the setup is known as a scan-by-tip configuration. An alternative configuration scans the sample against a stationary probe, referred to as the scan-by-sample system. The tip-mounted scanner was used for studies included in this dissertation. Piezoelectric materials used to fabricate AFM piezoscanners include barium titanate and lead zirconate titanate which expand and contract when a potential is applied.

Several piezo designs have been constructed for AFM scanners, however the most commonly used design for commercial AFM instruments is the tube scanner.[49] Surrounding the outside of the tube, four or more electrodes translate the tip in the x and y directions. The movement in the z direction is controlled by a single inner electrode.[50] The inherent nonlinearities and hysteresis of piezotube scanners under applied potentials can cause artifacts in AFM images. By applying a sawtooth voltage to the x piezo element and a voltage ramp to the y piezo, the tip traces a raster scanning pattern over the sample surface to produce an image. In the z direction, a feedback loop is used to control the voltage applied to the z electrode. As the tip is scanned across the surface, a voltage is applied to the z electrode to maintain constant force between the tip and sample. The setpoint used for feedback can be modified to include cantilever deflection for static modes, or amplitude and frequency for oscillating AFM modes. Topography images are generated by using a calibrated sensitivity value to convert piezo voltage to real height data.

The changes in deflection or torsional movement of the AFM tip are monitored using an optical deflection set up, shown in Figure 2.1.[23] Other methods such as STM,[15] interferometry,[51] and crystal oscillators[52] can be used to track the tip position which are less common. Before AFM imaging, a red diode laser (670 nm typically) is positioned onto the back of a reflective cantilever. A coating of aluminum or gold on the backside of the cantilever is used to reflect the laser onto the center of a four quadrant photodiode detector. Small changes in cantilever deflection due to surface topography will lead to vertical displacements of the laser spot on the position sensitive photodiode. Also, torsional twisting of the AFM tip due to friction will influence the lateral motion of the laser spot on the detector. The photodetectors within the four quadrants are used to sensitively track the movement of the AFM tip. The data is compiled to generate 3D images that represent the tip-sample interactions as a function of the tip position.

Tip-surface interactions mapped with AFM include topography,[15, 53] friction,[54] elasticity,[55] conductivity,[56] magnetism,[57, 58] piezoresponsiveness,[59] and electrostatics.[60] There are over 50 different modes of AFM that probe tip-sample interactions. Several common modes of SPM are listed in Table 2.1. The SPM modes used in this dissertation are denoted by an asterisk.

Table 2.1 SPM imaging and measurement modes.

Imaging mode	**Feedback**	**Information obtained**	**Probe type**	**Refs.**
Contact mode*	cantilever deflection	topography and lateral force	Si or Si_3N_4	15
AAC tapping-mode*	cantilever amplitude	topography and phase	Si or Si_3N_4	61
MAC tapping-mode*	cantilever amplitude	topography and phase	Magnetically coated cantilever	62
Magnetic sample modulation AFM*	cantilever deflection	topography, amplitude and phase (of magnetic nanoparticles)	Si or Si_3N_4	63
Magnetic force microscopy	interleave mode	Topography and magnetic dipole information	Magnetically coated probe	57
Kelvin probe microscopy	interleave mode	surface work function	Conductive probe	64
Conductive probe AFM	cantilever deflection	surface conductivity	Conductive probe	56

2.3 Force spectroscopy measurements with AFM

Force spectroscopy measurements enable a quantitative measurement of the interactions between the tip and the sample. A force-distance curve can be used to measure the strength of

tip-sample interactions.[65, 66] It is also possible to measure local properties of materials using force spectroscopy such as adhesion,[67, 68] elasticity,[69, 70] and bond rupture values.[71] A force-distance curve is acquired by applying a triangular waveform voltage to the z piezoelement within the tube scanner to enalbe an approach-retreat cycle. In this cycle, the tip is forced to approach and come into contact with the sample before being retracted. The deflection voltage is monitored during the cycle to obtain the deflection versus distance curve. Deflection voltage can later be converted to force using the deflection sensitivity (from the slope of the deflection-distance curve) and Hooke's Law (Eq. 1).

$$F = -kx \qquad Equation\ 1$$

The force exerted by the tip can be modeled using Hooke's law (eq. 1) where F is equal to the force applied to the tip from the sample, k is the spring constant of the probe's cantilever *w*here x is the cantilever deflection. According to the Hooke's model, the force of the AFM tip will change proportionally with tip displacement.

An example of a force-distance curve is shown in Figure 2.2. During the approach and retract cycle, the tip will sense both attractive and repulsive forces. In region I, no deflection of the AFM cantilever is observed because the tip is far away from the sample. Upon approaching the sample, the tip will snap into contact with the surface due to attractive Van der Waals and electrostatic interactions between the sample and tip, which leads to the small dip found in region II. In region III of the force-distance curve, the tip is in contact with the sample and slowly begins to feel a repulsive force from the sample as it presses more into contact with the surface. Short range repulsive forces between the tip and sample will cause the cantilever to bend as shown in region IV at a maximum deflection value as set by the user. There is usually a hysteresis observed for regions II and IV, because tips are not perfectly symmetric. Once the

maximum deflection value is reached, the tip begins the retraction cycle. In region V, the tip adhesive forces maintain tip-sample contact which leads to a minimum deflection single. This long range attractive force is usually caused by a contamination layer and capillary interactions between the tip and sample. Imaging in liquid will minimize this region of the force-distance curve. Once the distance between the tip and the sample becomes large enough to overcome the attractive forces, the tip will snap out of contact with the surface and return to zero deflection (region VI).

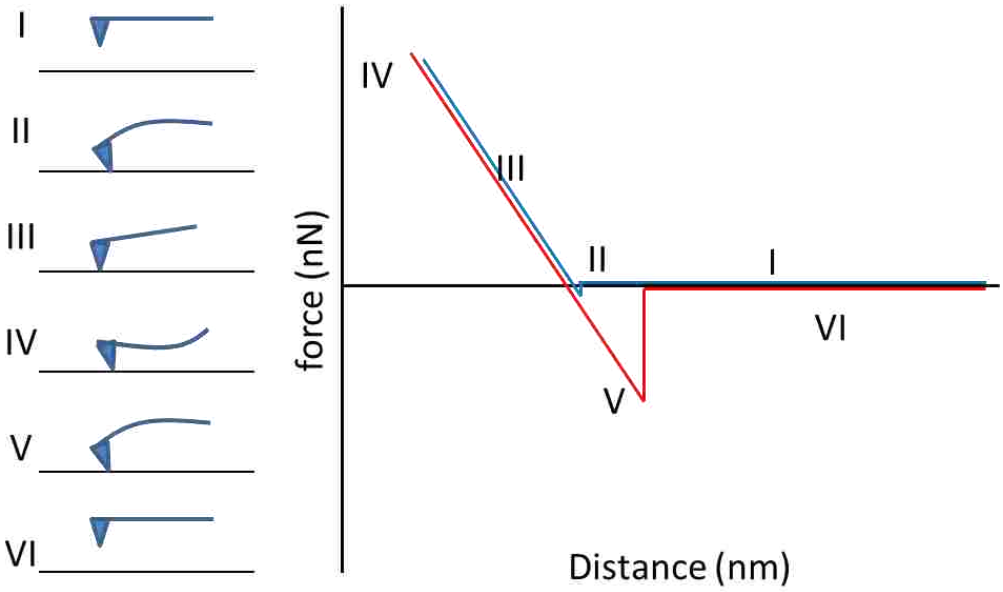

Figure 2.2 Force distance curve showing tip-sample interactions during an approach (blue) and retract (red) cycle.

2.4 Contact mode atomic force microscopy

The first AFM images published in 1986 by Binnig et al. were acquired using contact mode.[15] Contact mode AFM is the easiest mode of operation and has routinely been used to resolve atomic lattices. During scanning, the AFM tip remains in continuous contact with the surface. The feedback loop for contact mode operation maintains a constant force between the tip

and the sample. As changes in force cause a change in the deflection of the cantilever, this is sensed by the PSD. A voltage adjustment is applied to the z piezo electrode to compensate for the change in force by vertically adjusting the position of the AFM probe. Topography images are generated from plotting the z piezo voltage adjustments.

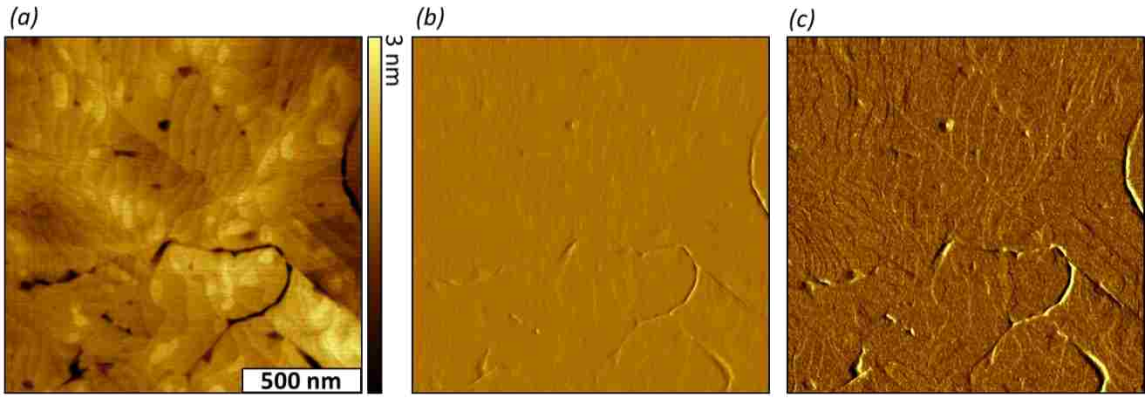

Figure 2.3 Contact mode images of 111-tris(mercaptomethyl)heptadecane on Au(111) acquired in ethanol. *(a)* Topography, *(b)* deflection or error signal, and *(c)* lateral force image.

Three types of images can be acquired simultaneously with contact mode AFM: topography, deflection, and lateral force as shown in Figure 2.2. The images reveal details of a gold surface coated with 1,1,1-tris(mercaptomethyl)heptadecane and were acquired in ethanol using contact mode. When imaging in liquid the force between the tip and sample are greatly reduced to minimize sample perturbation.[72] The local topography of the gold surface is shown in Figure 2.2a, where protruding surface features are represented by a lighter color. Overlapping step edges and terraces which are characteristic of the underlying gold surface are clearly visible in the 1.5×1.5 μm^2 topography image. The AFM deflection image (Figure 2.2b) represents the error signal associated with the AFM feedback loop. When scanning parameters are optimized, very little signal should be apparent in the deflection image. Since the feedback loop cannot instantaneously compensate for changes in tip-sample forces some contrast will be observed,

however deflection images are rarely reported. As the tip is scanned across the surface, frictional forces influence the lateral tip movement depending on the chemistry of the surface. Frictional forces cause a torsional twisting of the cantilever and produce lateral motion of the deflection signal on the PSD. Lateral force images (Figure 2.2c) are used to distinguish differences of chemical functionalities at the interface. Quantitative measurements of nanoscale friction can be extracted from lateral force images.[54, 73]

2.5 Intermittent contact or tapping-mode atomic force microscopy

Occasionally the shear forces exerted between the tip and the sample can damage the probe or sample when operating in contact mode. Clearly resolved images are difficult to acquire when there is stick-slip adhesion for soft or sticky samples. Oscillating modes of AFM such as tapping-mode were invented to eliminate shear forces for problematic samples. For tapping-mode, also known as intermittent contact or acoustic atomic force microscopy (AC AFM), the tip is driven to oscillate at or near its natural resonance frequency. This dynamic mode of AFM is particularly useful when imaging soft, delicate samples such as proteins on a solid substrate. An example of the differences between contact mode and tapping-mode AFM is shown for topography images of fibrinogen on mica in Figure 2.3. The contact mode image exhibits horizontal lines which are artifacts caused by stick-slip adhesion and displacement of the protein (Figure 2.3a). Individual proteins can easily be resolved in the tapping-mode image (Figure 2.3b) due to the elimination of shear force.

Two distinct mechanisms have been developed to drive the actuation of the AFM tip for tapping-mode. For acoustically driven vibration (AAC AFM) the tip is attached to a small piezoceramic actuator to cause mechanical vibration of the AFM tip. This setup can be problematic when imaging in liquids. Vibration of both the liquid and the liquid cell assembly

make it difficult to locate and select a resonance frequency for imaging.[74] Selective vibration of the tip can be achieved by applying an AC magnetic field to a magnetic lever (MAC AFM). If the cantilever is coated with a magnetic material, the tip will be driven to vibrate to minimize problems for imaging in liquids.[61, 62] The feedback loop for AC AFM is operated by maintaining constant amplitude of the probe oscillation.

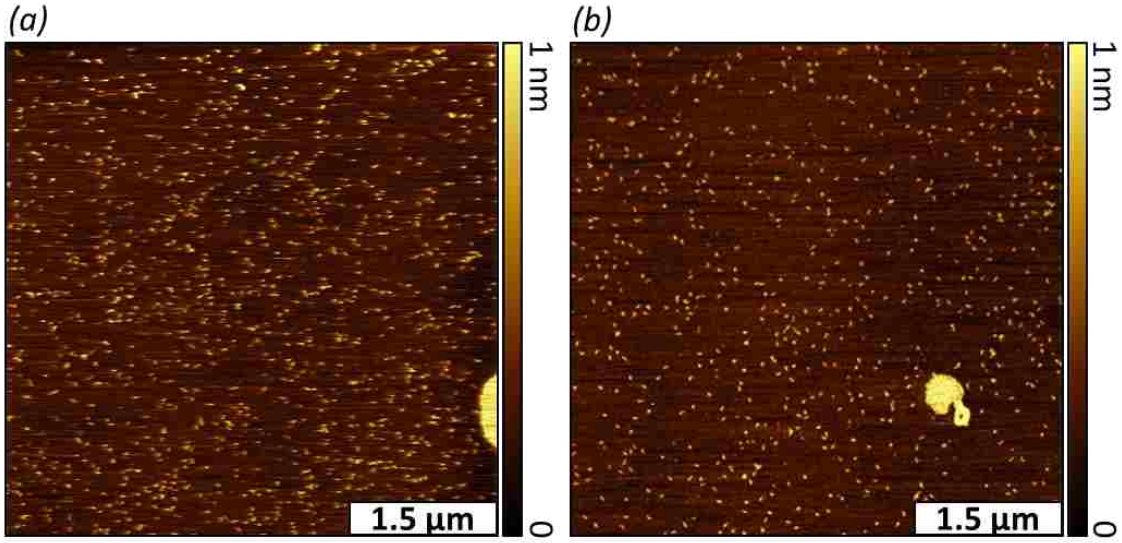

Figure 2.4 Improvements in resolution for imaging fibrinogen on mica(0001) imaged in ambient air using contact versus intermittent contact mode of AFM. *(a)* Contact mode topography frame; *(b)* tapping-mode image.

Three information channels can be simultaneously acquired using tapping-mode AFM, topography, amplitude and phase, as shown in Figure 2.5. Ring nanostructures of polyethylene glycol (PEG) silane rings were prepared using particle lithography.[75] Details of the sample morphology are revealed in the topography frame (750×750 nm^2) of Figure 2.5a, which are indistinguishable from contact mode images. The amplitude channel (Figure 2.5b) is derived from the changes in the amplitude of oscillation of the probe. Amplitude is used for instrument feedback in AC AFM, therefore the amplitude frames are not publishable. Changes in the phase of tip oscillation with respect to the driving signal are plotted as a phase image (Figure 2.5c). The

change in the phase of oscillation arises from changes in the energy dissipation between the sample and the probe.[76, 77]

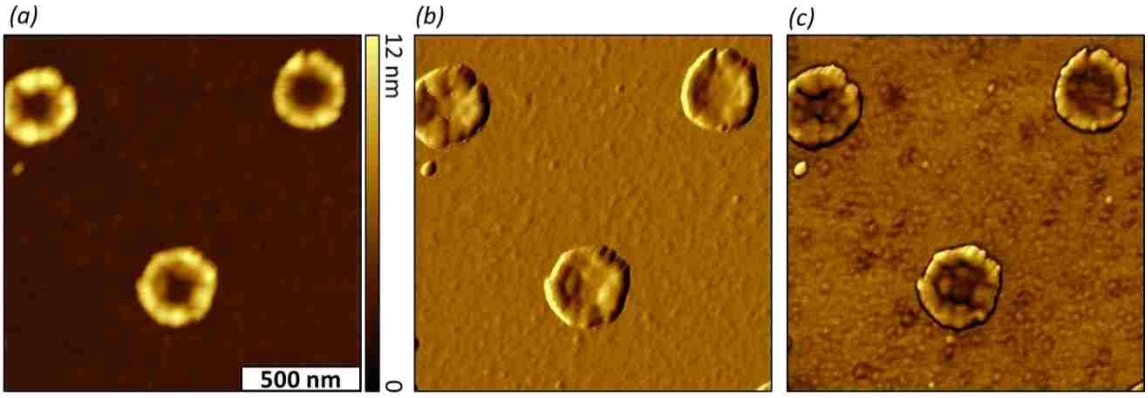

Figure 2.5 Tapping-mode images of PEG-silane nanorings on silicon prepared with particle lithography. Images were acquired in air. *(a)* Topography shown with simultaneously acquired *(b)* amplitude and *(c)* phase.

During tapping-mode operation, changes in the local adhesion, viscoelasticity, and slope (contact area between the tip and sample) of the sample will cause changes in phase of the tip oscillation.[78] Phase images are useful for discriminating the domains of phase separated polymeric samples where the domains may be similar in height and not resolved in topography images. The viscoelastic properties of the separated domains can be detected in AFM phase images.[79-81]

2.6 Structure and chemistry of organothiol and organosilane self-assembled monolayers

Self assembled monolayers were used to direct the deposition of proteins, nanoparticles, and inorganic salts on surfaces to prepare well-defined nanostructures for SPM studies. The methods for selectively positioning nanomaterials on surfaces are based on designed chemical interactions. The term self assembled monolayers (SAMs) refers to molecules which spontaneously form ordered molecular assemblies at a surface.[82, 83] The spontaneous assembly is driven by the affinity of a reactive headgroup for the surface while interactions between

neighboring molecules drive the organization of the assembly in the lateral directions. Advantages of SAMs include ease of preparation and the ability to design surface chemistry at the interface. An endgroup present on the self-assembling molecules can be used to tailor surface properties. The interfacial chemistry of SAMs has been used for applications in protective coatings for molecular device fabrication[84, 85] and biosensing chips.[86] Organothiols form well-ordered assemblies on coinage metal surfaces due to the affinity of the sulfur headgroup to the surface.[87, 88]

Organothiol SAMs can be prepared by immersing a clean gold substrate into a dilute solution of the thiol molecule in ethanol (~10^{-5} M) or 2-butanol. Over a few hours, alkanethiol molecules will physisorb to the surface in a lying down orientation. As the density of molecules increases on the surface, van der Waals interactions between adjacent hydrocarbon backbones cause the molecules to adopt a standing orientation. Reorganization of the molecules occurs until a densely packed film is formed.[26] Alkanethiol SAMs are crystalline films that adopt a commensurate ($\sqrt{3}\times\sqrt{3}$)R30° lattice on Au(111) with backbones tilted approximately 30° from surface normal (Figure 2.6a).[82, 83, 89] Mixed monolayers of *n*-alkanethiols on gold have been used to selectively attach proteins,[41] calcite crystals,[90] metals,[91] and cells.[92] Organothiols have the advantage of assembling on a conductive gold substrate which is beneficial for molecular electronic applications; however, films prepared from *n*-alkanethiols are not chemically stable with exposure to heat, light or oxidation.

Organosilane SAMs self-organize on hydrophilic surfaces that present free hydroxyl groups. Examples of substrates used to prepare organosilane SAMs include silicon oxide,[93, 94] quartz,[95, 96] and aluminum oxide.[97, 98] The structure of an organosilane SAM is presented in Figure 2.6b. While *n*-alkanethiol SAMs are known to be densely packed and well-ordered, *n*-

alkylsilane SAMs are more disordered. The surface density of organosilane SAMs depends sensitively on preparation parameters such as immersion time, temperature, humidity, and solvent choice.[99-101] Organosilane SAMs are thermally stable and chemically robust due to the covalent nature of the siloxane network which links the molecules to the substrate and to neighboring molecules. Covalent bonds that makeup the siloxane networks are formed through condensation reactions between neighboring silanol molecules (Si-OH) and free hydroxyl groups present on the substrate. Due to the high reactivity of the silanol group, silanes are functionalized with trichloro or trialkoxy headgroups. Before condensation occurs, a hydrolysis step converts the parent molecule to a trisilanol. Trace amounts of water are necessary to initiate the hydrolysis of silanes to silanols.[102] Too much water will cause polymerization of the silanes, and may generate multiple layers to form on the substrate. During preparation of organosilane SAMs, control of reaction conditions is critical for film quality. Because of the properties of organosilanes, surface architectures can be prepared by controlling the presence of water on the support surface.[75] Organosilane SAMs can be prepared through the vapor phase or the solution phase. In solution, the substrate is immersed in a 0.1% solution of silane in a dry solvent such as bicyclohexyl or toluene for a few hours. To deposit molecules from a vapor phase, heat can be applied to a substrate placed within a sealed jar containing neat silane solution.

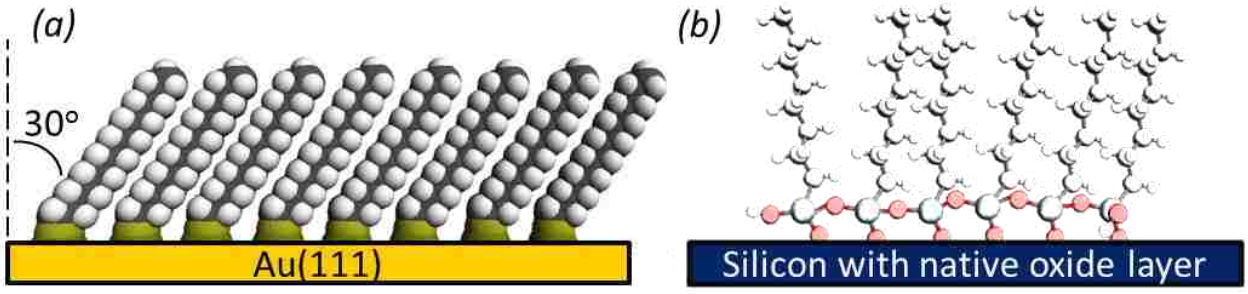

Figure 2.6 Two types of self-assembled monolayers. *(a)* Alkanethiol SAM of Au(111). *(b)* Organosilane SAM of the native oxide layer of silicon.

2.7 Particle lithography

Methods to fabricate chemically patterned surfaces of SAMs with sub-micron resolution include electron beam lithography,[103, 104] microcontact printing,[105] scanning probe lithography (SPL),[106-108] and particle lithography.[109-111] Approaches with particle lithography provide high-throughput capabilities to generate nanoscale features.[112] The first illustration of particle lithography demonstrated the fabrication of an array of plasmonic silver triangles, reported by Deckman and Dunsmuir in 1982.[112, 113] Particle lithography has been used to pattern nanomaterials such as nanoparticles,[114] proteins,[115] organosilanes,[116] and metals.[117, 118]

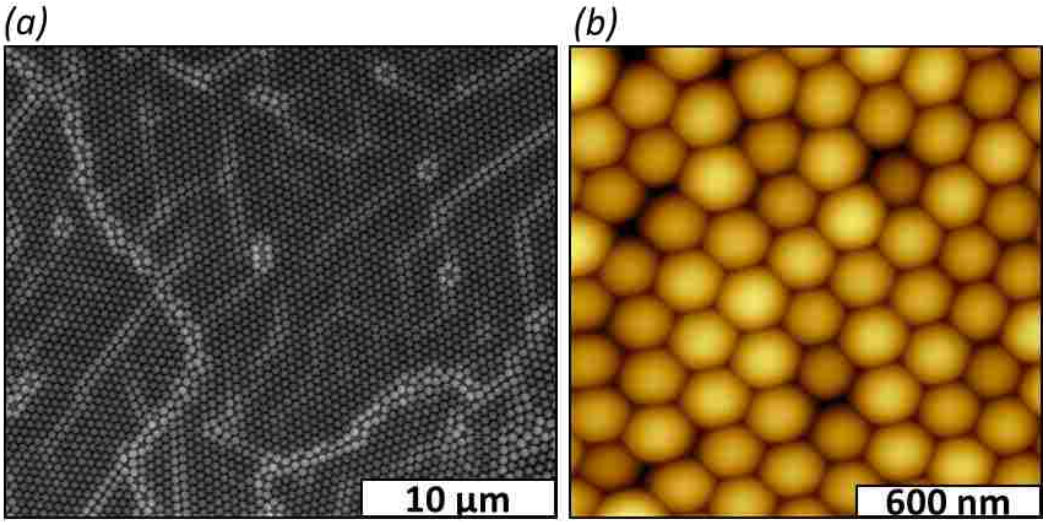

Figure 2.7 Mesosphere template of 300 nm latex used for particle lithography. *(a)* Long range order over tens of microns shown in the 80 × 80 µm^2 SEM micrograph; *(b)* hexagonal arrangement of the mesospheres is apparent in the AFM topograph.

By naturally drying a suspension of polystyrene latex or silica mesospheres on a flat surface, convective and capillary interactions drive the spheres to form a crystalline array. The surface coating of mesospheres provides a surface mask or template for nanoscale lithography. Tapping-mode images of a film of 300 nm polystyrene latex formed on mica are shown in Figure 2.7. The film of mesospheres exhibit long range order for domains as wide as 30 µm, as seen in

the SEM of Figure 2.7a.While individual spheres are difficult to resolve at this magnification, the white lines present in the image show the domain boundaries of the packed spheres. The close-packed arrangement of monodisperse silica or latex mesoparticles is demonstrated in the AFM topography frame in Figure 2.7b. The terminal groups of patterned SAMs prepared by particle lithography provide spatial selectivity to direct the adsorption of other nanomaterials to build surface architectures.[119, 120]

CHAPTER 3: DYNAMIC MAGNETIC CHARACTERIZATIONS AT THE NANOSCALE: A NEW MODE FOR AFM IMAGING WITH MAGNETIC SAMPLE MODULATION (MSM-AFM)[8]*

3.1 Introduction

Magnetic sample modulation (MSM) combined with contact mode atomic force microscopy (AFM) provides a sensitive way to detect the vibration of magnetic nanomaterials at the level of individual nanoparticles or ferroproteins. Rather than using a magnetically coated AFM probe as a sensor, the strategy is to use a non-magnetic probe for contact mode imaging to characterize the vibration of nanomaterials responding to the flux of an AC electromagnetic field. The hybrid mode of imaging under electromagnetic flux is referred to as magnetic sample modulation AFM (MSM-AFM). An alternating electromagnetic field drives the actuation of magnetic and superparamagnetic nanomaterials that are attached to surfaces, and the AFM tip is used to detect the vibration of the samples. For MSM-AFM, an oscillating magnetic field is produced by applying an AC current to a wire coil solenoid placed under the sample stage. The AFM is configured for contact mode imaging, and the probe is scanned slowly across the vibrating samples. Selected parameters of frequency and magnetic field strength can be tuned to study dynamic changes in the vibrational response of samples.

The MSM-AFM imaging mode has been used successfully to detect the vibration of nanomaterials with dimensions less than 1.0 nm[121] and has been applied for measurements with ferritin, an iron-containing protein.[63] Dynamic measurements can be accomplished by changing the modulation frequency and the strength of the applied electromagnetic field. With MSM-AFM, responses of both the amplitude and phase signal along with spatial maps of the

* Chapter 3 previously appeared as Englade-Franklin, L. E.; Serem, W. K.; Daniels, S. L.; Garno, J. C. Dynamic magnetic characterizations at the nanoscale: A new mode for AFM imagaing with magnetic sample modulation (MSM-AFM), 2014. It is reprinted by permission of Nova Science Publishers (see page 122).

topography channel can be collected simultaneously. The hybrid approach of combining MSM with contact mode AFM provides nanoscale characterizations for detecting the changes in vibrational resonance signatures, differences in vibrational amplitude versus size, and coupling effects of the magnetic response due to the proximity of adjacent magnetic nanomaterials.

Scanning probe microscopy (SPM) encompasses surface measurements to visualize and study the surface properties of nanomaterials with molecular resolution.[15, 122] Modes of SPM have been developed to measure material properties at the nanoscale, including magnetic forces. To measure magnetic forces, SPM modes include magnetic force microscopy (MFM),[57, 123-127] magnetic resonance force microscopy (MRFM),[128-132] and magnetic sample modulation (MSM).[133, 134] A comparison of several SPM imaging modes that use magnetic probes is presented in Table 3.1, including MAC-mode AFM.[57, 62, 125-132, 134-137] Although MAC-mode is not actually used to measure magnetic forces, the electromagnetic actuation of a probes with magnetic coatings is used to achieve tapping-mode characterizations.[138]

Magnetic force microscopy and MRFM are operated in non-contact mode and sense small magnetic forces between the tip and sample probed at relatively large distances (20-200 nm). [58, 139, 140] Magnetic resonance force microscopy produces images using magnetic resonance at the nanoscale.

The resonance signatures and electronic spins of magnetic nuclei in samples are captured using MRFM. Magnetic force microscopy (MFM) is used to map domains and polarities of magnetic samples. Although MAC-mode is listed in Table 3.1, this mode is not actually used for measuring magnetic forces.

A magnetic coating is required for the top-side of MAC-mode probes to drive the actuation of the probe for tapping-mode AFM studies. The tip is actuated by an AC

electromagnetic field which is generated from a wire coil solenoid located in the sample stage or scanner nose cone. With MAC-mode, the tip is driven to gently tap the sample as a means to improve the resolution of AFM for studies of soft and sticky samples such as biological materials.

Table 3.1 Scanning probe imaging modes used for magnetic measurements

SPM Mode	Operation	Type of Probe	Information Obtained	Types of samples	Resolution	Ref.
Magnetic Force Microscopy, MFM (1987)	lift-mode noncontact force-deflection feedback	magnetic tip	magnetic mapping; information about dipole orientation	magnetic samples	~ 25 nm	5-10
Magnetic Resonance Force Microscopy, MRFM (1992)	non-contact force-deflection feedback	magnetic tip	magnetic resonance images; including resonance signatures and electronic spins	samples that contain atoms with magnetic nuclei	< 10 nm	11-15
Magnetically Actuated Cantilever, MAC-mode (1996)	tapping-mode amplitude feedback	magnetic tip	high resolution tapping-mode images of samples	nonmagnetic samples; suitable for tapping-mode in liquids	< 1 nm	17-20
Magnetic Sample Modulation AFM (2009)	contact mode force-deflection feedback	*nonmagnetic* tip, with a soft cantilever	magnetic mapping; studies of magnetic response with changes in magnetic field strength and frequency	magnetic, paramagnetic, superparamagnetic nanomaterials	< 1 nm	2, 16

The strategy of the conventional SPM imaging mode for magnetic detection known as magnetic force microscopy (MFM) [57, 124, 141-144] is quite different from the magnetic sample modulation mode. For MFM, one must use an AFM tip with an underside coated with a magnetic material to sense the relatively weak long-range forces of magnetic areas of surfaces operating over distances of 50-200 nm. The strength of the magnetic field of the sample must be strong enough to deflect or attract a micrometer-sized cantilever to enable mapping of the magnetic domains with MFM. However, the MFM approach provides a means to map the strength and polarity of the magnetic field at certain distances, (e.g. 50, 100, 150 nm) from the surface. When the tip is attracted towards the surface, dark contrast is generated in images; as the tip is repelled by the sample, brighter contrast results. Thus, MFM indicates the relative strength and polarity of magnetic regions.

For operation with magnetic force microscopy (MFM) little modification of the AFM instrument is required. A magnetically coated tip (underside of the probe) is used to detect long range magnetic forces of surface domains. An initial topographic scan is used to obtain a line profile of the sample, and then the probe is lifted from the surface for a second scan to measure magnetic forces. At a certain distance above the sample, lift mode (also called interleave mode) is used to retrace the probe along the memorized topography profile to construct an image of magnetic forces. During the second pass, the magnetic probe will either be attracted towards or repelled by the sample, according to the polarity of the magnetic field to generate a map of the forces of magnetic domains. The limitation of MFM detection intrinsically depends on the size and spring constant of the magnetic lever. The topography resolution is generally poor with MFM, since the magnetic coatings on the underside of the tips results in probes that are blunt and bulky. Magnetic coatings increase the diameter of the apex of the AFM probes, and therefore

decrease the resolution that can be achieved.[145, 146] Also, depending on the nature of the sample, magnetized probes may attract and remove magnetic nanomaterials from the surface.

In a few cases, specially engineered probes have been used to attain greater sensitivity for MFM studies. A single ferritin molecule was attached to the end of a functionalized AFM probe to obtain a resolution of 10 nm using MFM by Kim et al.[147] Tips fabricated through a method of facing target sputtering (FTS) have a narrow tip apex on the order of 20 nm, compared to 50 nm for commercially available MFM probes.[148] The FTS fabricated probes were shown to achieve 12 nm lateral resolution for MFM studies.

Magnetic sample modulation has several advantages compared to conventional SPM magnetic imaging modes. Since the probe is operated in contact mode without a bulky coating on the underside of the tip, MSM-AFM is more sensitive to surface topography. Rather than respond to magnetic forces of the sample, for MSM-AFM the tip is used as a force and motion sensor to detect how the sample responds to an external magnetic field. Magnetic coatings of MFM tips are prone to wear off or oxidize, and therefore cannot be used for extended times. Over time, the thin magnetic films of the probes lose strength and need to be remagnetized. Also, for the purpose of calibration, it is difficult to actually measure the strength of the magnetic field for such ultrasmall probes which are a few microns in length.

3.2 Operating principle for magnetic sample modulation AFM (MSM-AFM)

Changes in vibrational response ranging from ferromagnetism to superparamagnetism can be detected with MSM-AFM. Operating in direct contact mode, a nonmagnetic probe is used to map the locations and motion of nanomaterials that are driven to vibrate on surfaces. A solenoid underneath the sample stage generates an oscillating electromagnetic field that causes magnetic nanomaterials to vibrate. With MSM-AFM the size and location of magnetic domains

can be detected, as well as acquiring information of the magnetic response and mechanical resonances of sample vibration.

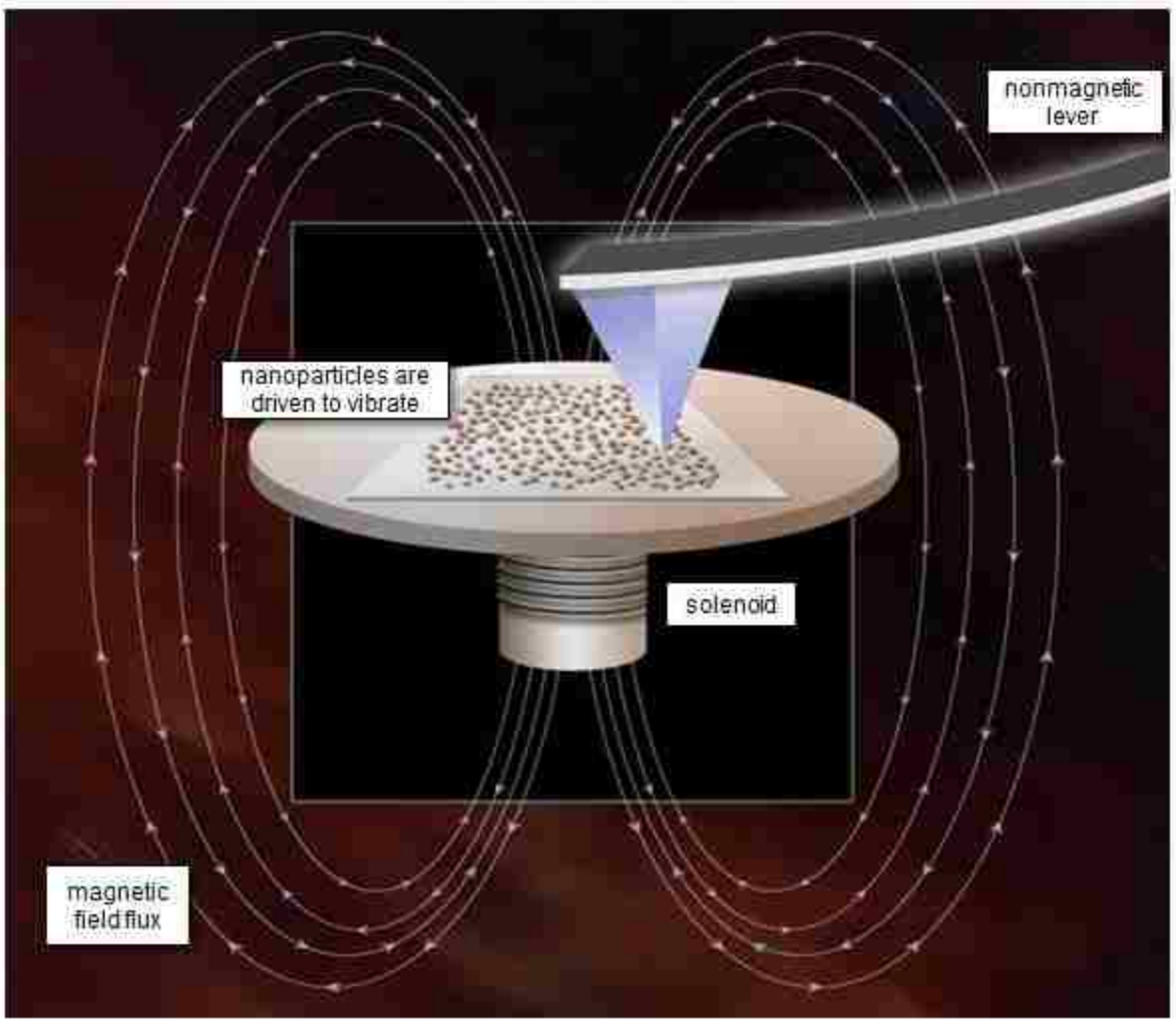

Figure 3.1 Concept for magnetic sample modulation (MSM-AFM). A non-magnetic AFM tip responds to the physical vibration of nanoparticles on a surface as a mechanism for sensing magnetic domains. The flux of the magnetic field generated by a solenoid underneath the sample induces nanoparticles to vibrate. *Reprinted with permission from reference 57.*

The sensitivity of lock-in detection enables magnetic domains as small as 1 nm to be detected with MSM-AFM. Dynamic studies of single nanoparticles can be accomplished by parking the probe on nanostructures and sweeping the field strength and frequency parameters.

For the MSM-AFM imaging mode, non-magnetic levers and probes are required for direct contact mode scanning under the condition of magnetic actuation of the sample.

Essentially, MSM-AFM enables the visualization of how nanomaterials respond to the flux of an applied AC electromagnetic field. When samples are exposed to an alternating field, certain magnetic nanomaterials are induced to vibrate. By slowly scanning an AFM probe across a vibrating sample, the frequency and amplitude of the motion of the sample is tracked by changes in deflection of the tip. The concept for MSM-AFM imaging is shown in Figure 3.1. The AFM probe is much larger than the nanomaterials, thus it is important to use a soft cantilever with a relatively small force constant (e.g. 0.005-0.01 N/m). The amplitude and phase components of the tip motion are tracked during the scan by a lock-in amplifier to generate spatial maps of the magnetic domains. Magnetic areas can be mapped with exquisite resolution because of the high sensitivity of lock-in detection.

The instrument set-up for MSM-AFM is a hybrid of contact mode AFM combined with selective actuation of magnetic samples. A typical approach for imaging first involves acquiring conventional contact mode topography images. Next, the same area of the surface is scanned again, however with an oscillating electromagnetic field applied by the solenoid within the sample stage. The polarity, oscillation and flux of the magnetic field is generated and controlled by selection of parameters for the AC current applied to a wire coil solenoid, which is placed under the sample stage. When an electromagnetic field is applied to samples, only the magnetic domains vibrate, providing selective contrast for areas that are in motion. The differences for images with and without an applied magnetic field are used to map the response of magnetic samples. Changes in the phase and amplitude of vibrating nanomaterials are mapped, relative to the driving AC signal. Since a lock-in amplifier is used to acquire the amplitude and phase components of the deflection signals, exquisite sensitivity is achieved for slight changes in tip movement. Using MSM-AFM, responses of both the amplitude and phase signal acquired

simultaneously with the topographic channel, as well as spectra of the vibrational response can be mapped with angstrom resolution.

Oscillating magnetic fields can be applied to samples using a “MAC-mode” sample plate accessory (Figure 3.2). For operating the MAC-mode sample stage, an AC current is applied to a coil of wire, which produces an oscillating magnetic field. When a wire is formed into a loop or several loops to form a coil, a magnetic field develops that flows through the center of the loop or coil along its longitudinal axis and circles back around the outside of the loop or coil, as shown in Figure 3.2b. The magnetic field lines circling each loop of wire combines with the fields from the other loops to produce a concentrated field down the center of the coil. The AC current generates a magnetic field which alternates in polarity and strength which can increase or decrease in strength according to the frequency and amplitude parameters of the driving current.

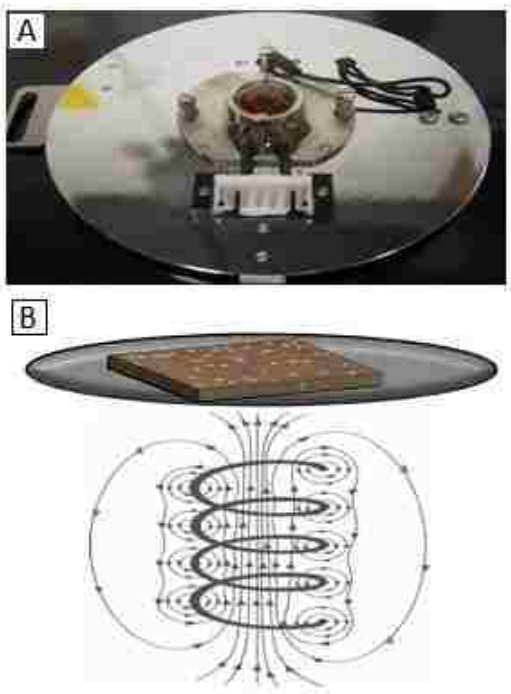

Figure 3.2 An alternating electromagnetic field is applied to samples for MSM-AFM studies. *(a)* Photograph of the underside of a MAC-mode sample plate incorporating a wire coil solenoid used to generate an electromagnetic field (Agilent, Inc.). *(b)* Electromagnetic field lines generated by a solenoid.

The strength of the magnetic field of the solenoid increases proportionately as the current is increased. In comparison to conventional macroscopic magnetic measurement approaches, the field strength for MSM-AFM is on the order of 0.05 to 0.6 Tesla. In the MAC-mode stage, samples are placed close to one end of the solenoid to experience the strongest flux of the AC electromagnetic field.

For the instrument set-up of MSM, positional feedback for the scanner is unchanged and force-deflection settings typical for scanning in contact mode are used for topographic data acquisition. The positional feedback loop for MSM-AFM is the same as that used for force modulation and contact mode AFM; however the vibration of the sample is detected using channels of a lock-in amplifier. To obtain digital channels for the amplitude and phase components of the tip motion, an auxiliary output channel from the quadrant photodiode of the AFM scanner is directed to input channels of a lock-in amplifier, using the driving AC waveform as a reference. When an AC current is applied to the solenoid, the frequency of the AC field causes a switching of the north and south poles of the magnetic field produced by the solenoid to create a flux. Magnetic nanomaterials on the surface are driven to align with the flux of the switching magnetic field to induce vibration. Thus, the periodic motion of the sample vibration can be tracked by changes in the deflection of the tip. The changes in phase angle and amplitude as the tip interacts with the vibrating sample are plotted as a function of tip position to create MSM-phase and MSM-amplitude images. Topography images can be influenced by sample motion, detected by a broadening of the surface features, and changes in lateral force frames may also be apparent.

The imaging frequency and strength of the AC field should be chosen to generate tip-sample resonance. The parameters are evaluated for each individual experiment by sweeping a

range of frequencies and plotting the amplitude response. Control sweeps are done while the probe is disengaged from the surface to ensure that the tip does not respond to the AC field. When the AFM tip is not in contact with the vibrating sample, no peaks should be observed in the spectra. When the tip is placed in contact with a vibrating area of the sample, the spectra will reveal several prominent resonance peaks which can be used for imaging. Typically, frequencies with higher amplitude are chosen for characterizations. Different locations of the sample will produce changes in the characteristic resonance profiles, depending on the sizes and shapes of the nanomaterials.

Example images and spectra from an MSM-AFM experiment are shown in Figure 3.3 for a sample of $FeNi_3$ nanoparticles prepared on mica. Using the same AFM probe, conventional contact mode AFM images are shown in the top row of Figure 3.3, and the same area was imaged with an electromagnetic field applied when acquiring images shown in the second row. Bright spots pinpoint the locations of individual nanoparticles in the topography frame of Figure 3.3a; the nanoparticles are well dispersed throughout the 5×5 μm^2 area. When a magnetic field was not present (Figures 3.3a-c), there is no contrast apparent in the amplitude and phase channels. However, when the field was turned on (Figures 3.3d-f) the phase and amplitude images disclose the positions of vibrating nanoparticles with exquisite sensitivity. In fact, very small nanoparticles which cannot be resolved at this magnification in topography frames (Figures 3.3a and 3.3d) are easily distinguished in MSM-amplitude and MSM-phase images.

Beyond capabilities for mapping magnetic domains, MSM-AFM protocols have been developed to obtain dynamic information about the vibrational resonances of samples with changes in frequency and magnetic field strength.[121]

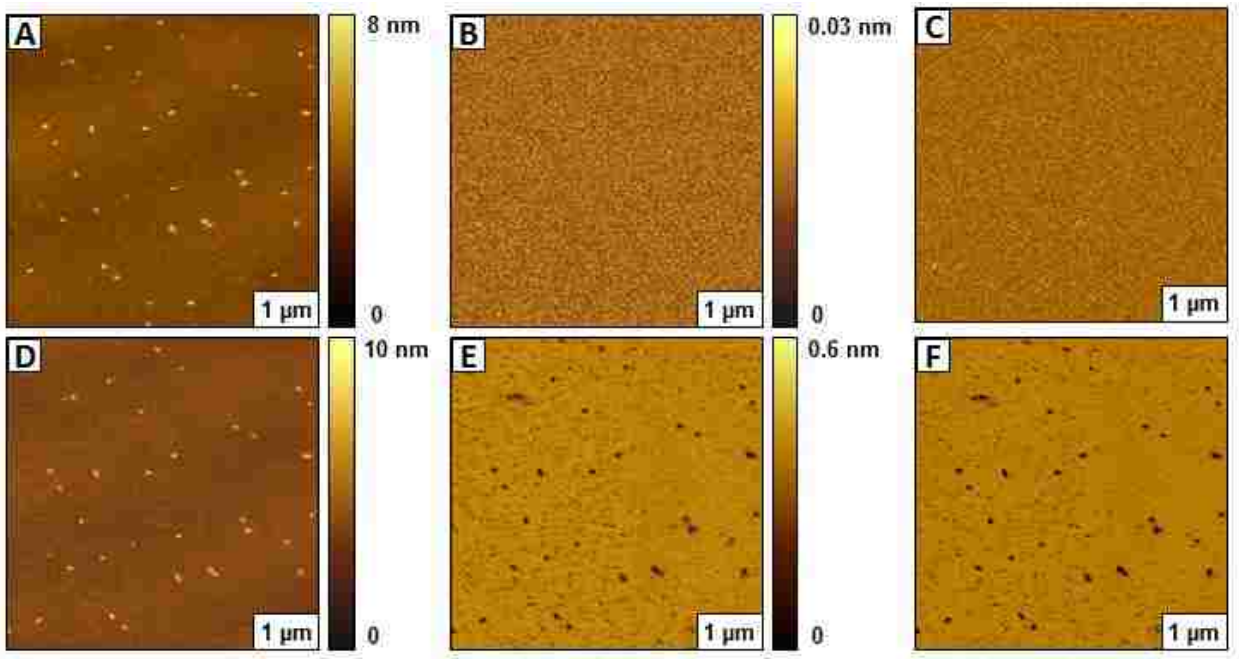

Figure 3.3 Nanoparticles of $FeNi_3$ prepared on mica substrates imaged with MSM-AFM. *(a)* Topograph in the absence of an AC field; simultaneously acquired *(b)* MSM-amplitude and *(c)* MSM-phase images. When an AC field is applied: *(d)* Topograph *(e)* MSM-amplitude and *(f)* MSM-phase images. *Reprinted with permission from reference 57.*

Dynamic experiments are accomplished by acquiring frequency sweeps at specific areas of the sample with designed parameters. Protocols can be designed to investigate how changes in the sizes of nanoparticles affect the amplitude of vibrational response, or to detect differences for nanomaterials with changes in magnetic field strength. Nanomaterials that have been investigated using MSM-AFM include iron oxide and intermetallic nanoparticles,[121, 149] magnetic nanostructures patterned on surfaces,[134] and ferroproteins.[133]

3.3 Characterization of magnetic nanoparticles with MSM-AFM

3.3.1 Nanoparticles and size-scaling limits of superparamagnetism

Unique magnetic phenomena are associated with nanoparticles which are different than properties of bulk materials.[150, 151] Basically, the physics and properties of magnetic nanostructures cannot necessarily be inferred from scaled down properties of a bulk material. As

particle sizes become smaller, more of the atoms of a nanoparticle are surface atoms; therefore surface and interface effects predominate.[152] Quantum effects which are related to completion of shells in systems with delocalized electrons are also observed for magnetic nanomaterials, depending on size.[151] Ferromagnetic nanomaterials exhibit an intense magnetic field when an external magnetic field is applied, but in a bulk sample the material will usually be nonmagnetic because of the random orientation of spin domains. A small externally imposed magnetic field can cause the magnetic domains to align to become magnetized. Ferromagnets will remain magnetized after exposure to an external magnetic field. Size scaling relationships can be used to tailor magnetic properties of materials from the bulk ferromagnetic level to the superparamagnetic regime. For scaling effects of nanomagnetic materials, precise knowledge of the relationships between particle shape and size, surface structure and the resulting magnetic properties is incomplete. Differences in the magnetic properties for materials with nanoscale dimensions are not well defined even for simple nanoparticles composed of pure materials such as Fe, Co, or Ni, whereas the bulk magnetic properties are well understood.

Superparamagnetism is an example of the interesting size-dependent phenomena of magnetic nanoparticles. Nanoparticles with superparamagnetic behavior are similar to paramagnetic substances which lose their magnetization when the magnetic field is removed; however superparamagnetic particles exhibit a much higher magnetic moment.[153, 154] Superparamagnetic nanoparticles do not retain any magnetism after removal of the magnetic field, which is a critical requirement for biomedical applications of magnetic resonance imaging (MRI) contrast agents.[155]

Nanotechnology has made it possible to synthesize and specifically tailor the magnetic properties of nanoparticles for certain applications.[156-158] Magnetic nanoparticles have been used

in high-density data storage devices,[159] ferrofluids,[160-162] and magnetic refrigeration systems.[163] Magnetic nanoparticles are critical for biomedical applications such as magnetic resonance imaging,[164-167] hyperthermic treatment for malignant cells,[168, 169] magnetic separations,[164, 170] site specific drug delivery [164] and the manipulation of cell membranes.[156] Nanoparticles have been conjugated with DNA, peptides and antibodies to generate magnetic nanoparticle bioconjugates with hybrid functionalities.[164, 166, 170-174] The size affects both physical and pharmacokinetic properties of nanoparticles.[155]

The size limit for magnetic nanoparticles is the superparamagnetic limit. When only a single domain is present in a small ferromagnetic or ferrimagnetic material, all of the magnetic spins are aligned within the nanomaterial.[175] In the absence of an outside field, superparamagnetic nanoparticles exhibit no magnetism and have paramagnetic behavior due to fast thermal flipping of the magnetic spins within the single-domain particle. When an outside magnetic field is applied, the spins of the particle will align with the magnetic field. Magnetic sample modulation (MSM-AFM) offers the capability of detecting and imaging the response of ferromagnetic and paramagnetic nanomaterials in an external magnetic field, as well as superparamagnetic nanomaterials. Examples will be presented for two systems of nanoparticles, cobalt nanoparticles (2 nm) and intermetallic FeNi3 nanoparticles as small as 0.8 nm.

3.3.2 Magnetic mapping of superparamagnetic cobalt nanoparticles

Combining nanolithography with AFM characterizations is a practical strategy for analysis of surface properties at the nanoscale. For studies with MSM-AFM, the cooperative effects of adjacent nanoparticles can influence measurements of magnetic response. Therefore, test platforms of samples were prepared using approaches of particle lithography to define the arrangement of nanoparticles. Particle lithography is a nanofabrication approach used to organize

nanomaterials on surfaces, based on simple steps of mixing, drying and rinsing with templates of larger mesospheres of latex or silica.[119, 176, 177] An approach coined as "two particle" lithography has been used to organize nanoparticles on surfaces with minimal steps of sample preparation. [114] For this method of nanopatterning, two types of particles were used, larger spheres such as latex or silica (diameters ranging from 200 to 500 nm) provided a structural template to guide the deposition of smaller metal nanoparticles, with sizes smaller than 20 nm.

Cobalt nanoparticles (2.0 ± 0.3 nm diameter) were synthesized using templates of DNA plasmids to generate monodisperse sizes and shapes as previously reported.[178] Views of ring arrangements of cobalt nanoparticles are shown Figure 3.4 that were prepared by particle lithography with 500 nm latex spheres. Individual cobalt nanoparticles are not easily distinguished within the tightly packed rings at this magnification (4×4 μm2) in the topography frame of Figure 3.4a. However, the areas of mica surrounding the rings reveal a few individual nanoparticles. An interesting capability of MSM-AFM is the option to turn the magnetic field on and off during the process of a scan as shown in Figures 3.4a-c. The simultaneously acquired MSM-amplitude and MSM-phase images (Figures 3.4b and 3.4c, respectively) reveal the arrangement and shapes of the cobalt nanoparticles when the electromagnetic field is activated at the midpoint of the scan. In the presence of an alternating magnetic field, the nanoparticles vibrate which can also affect the resolution of the topography frame (Figure 3.4a). Of course, in the absence of an applied AC field, no contrast is observed in the upper half of the MSM-amplitude and MSM-phase channels. The dark bands of the topography frames at the sides of taller features which run in a horizontal direction are an imaging artifact attributable to mathematical flattening steps of digital image processing. The bands are not scratches or indentations of the mica substrate.

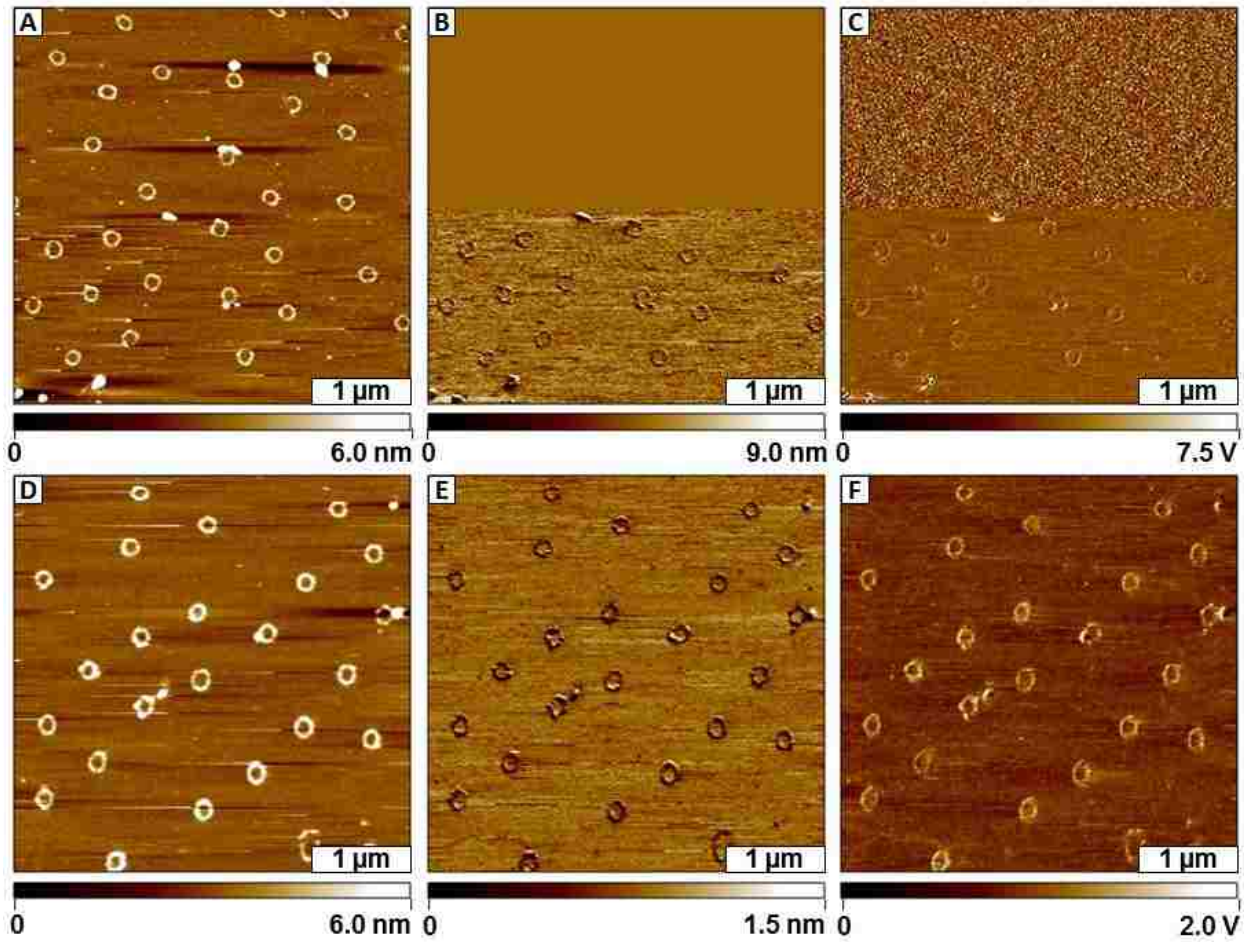

Figure 3.4 Rings of cobalt nanoparticles prepared on mica substrates imaged using MSM-AFM. Effects of switching on the electromagnetic field midway through a scan viewed with *(a)* Topography, *(b)* MSM-amplitude, and *(c)* MSM-phase channels. Complete scan in the presence of an AC field: *(d)* Topograph; *(e)* MSM-amplitude and *(f)* MSM-phase frames. *Reprinted with permission from reference 150.*

Images of cobalt nanoparticles acquired with the magnetic field turned on throughout the entire scan are shown in Figures 3.4d-f. During MSM-AFM experiments, the ring arrangements of cobalt nanoparticles are preserved despite the vibration and motion of nanoparticles. The superparamagnetic nanoparticles of cobalt were induced vibrate in response to the flux of the magnetic field according to the frequency and amplitude of the driving AC signal sent to the solenoid. The resonance frequency and field strength applied to generate MSM-AFM images for Figure 3.4 were 116 kHz and 0.2 Tesla, respectively. The tip is driven to vibrate when it

encounters vibrating nanoparticles. Changes in the motion of the tip-surface contact are compared to the driving signal and are digitally plotted in amplitude and phase channels to generate surface maps of magnetic response. The amplitude and phase images disclose differences in tip motion between areas with the cobalt nanoparticles and bare regions of the surface (Figures 3.4e and 3.4f), which demonstrates the mapping capabilities of the MSM-AFM imaging mode.

3.3.3 Studies of intermetallic $FeNi_3$ nanoparticles using MSM-AFM

Intermetallic nanoparticles of $FeNi_3$ were synthesized using microwave chemistry for studies with MSM-AFM.[121] Although single component nanoparticles have been well studied, the potential of intermetallic systems remain to be investigated.[179] Microwave heating enables precise and reproducible control of synthetic parameters such as temperature and pressure within the reaction vessel. Nanoparticles synthesized by microwave irradiation are typically highly monodisperse with overall small sizes.[180-183] For studies with MSM-AFM, nanoparticles of $FeNi_3$ were rapidly synthesized in aqueous media using microwave heating.[121, 184] Samples for AFM studies were prepared by depositing a drop of a dilute solution of nanoparticles on mica surfaces, which were then dried. The strength of the magnetic field can be systematically increased during scans, to view surface changes according to effects of field strength (Figure 3.5). In the dynamic MSM-AFM experiment, the magnetic field strength was changed to settings of 0.05 T, 0.2 T, and 0.3 T at selected intervals during the scan. As the magnetic field strength was increased, more nanoparticles can be resolved in the MSM-amplitude and MSM-phase views of Figures 3.5b and 3.5c, respectively. Interestingly, the smallest of nanoparticles become visible at higher field strength. Although the nanoparticles probably respond to the lower field strength, a certain threshold energy is required to influence the motion of the much larger AFM tip. These results

suggest that smaller nanoparticles require greater field strength to influence the tip motion. Note that nanoparticles that are invisible in the topography image at this magnification are clearly detected in MSM-amplitude and MSM-phase frames, showcasing the capabilities of high sensitivity with MSM-AFM.

Interestingly, at the highest field strength setting of 0.3 T there is a contrast reversal for some of the larger nanoparticles in the MSM-phase image. The color scale flips so that the nanoparticles are bright, particularly for the larger aggregates of nanoparticles that are clustered together on the surface. The MSM-phase image does not scale with magnetic response; rather it indicates a change in phase angle of the reference and measured signals. This suggests that there is a shift or broadening of the vibrational resonance with magnetization – the properties of the samples do not change, rather the resonance of the vibrational response is broader with increased vibrational motion.

The size scaling effects of magnetic response of the $FeNi_3$ nanoparticles was evaluated quantitatively in Figure 3.5d. A plot of amplitude displacement of the AFM tip versus the nanoparticle size at varying magnetic field strengths is shown in Figure 3.5d to evaluate the scaling relationship between the nanoparticle size and the amplitude response that is detected by the AFM tip. Using the data from a single MSM-amplitude frame, the scaling behavior for 30 nanoparticles was plotted for measurements at 0.2 T and 0.3 T. At the lower field strength (circles) there is little difference in amplitude for particles ranging from 0.5 to 5 nm in diameter. However, when the field is ramped up to 0.3 T, the larger nanoparticles experience greater vibrational amplitude, and the mass magnetization effects for larger nanoparticles becomes apparent when the diameter is larger than 3 nm (diamonds). The sizes of the nanoparticles were determined from the topography frames by imaging the samples with the magnetic field turned

off, so that sample vibration did not influence the measurement. A subsequent scan was taken of the same area when the magnetic field was turned on for measuring amplitude.

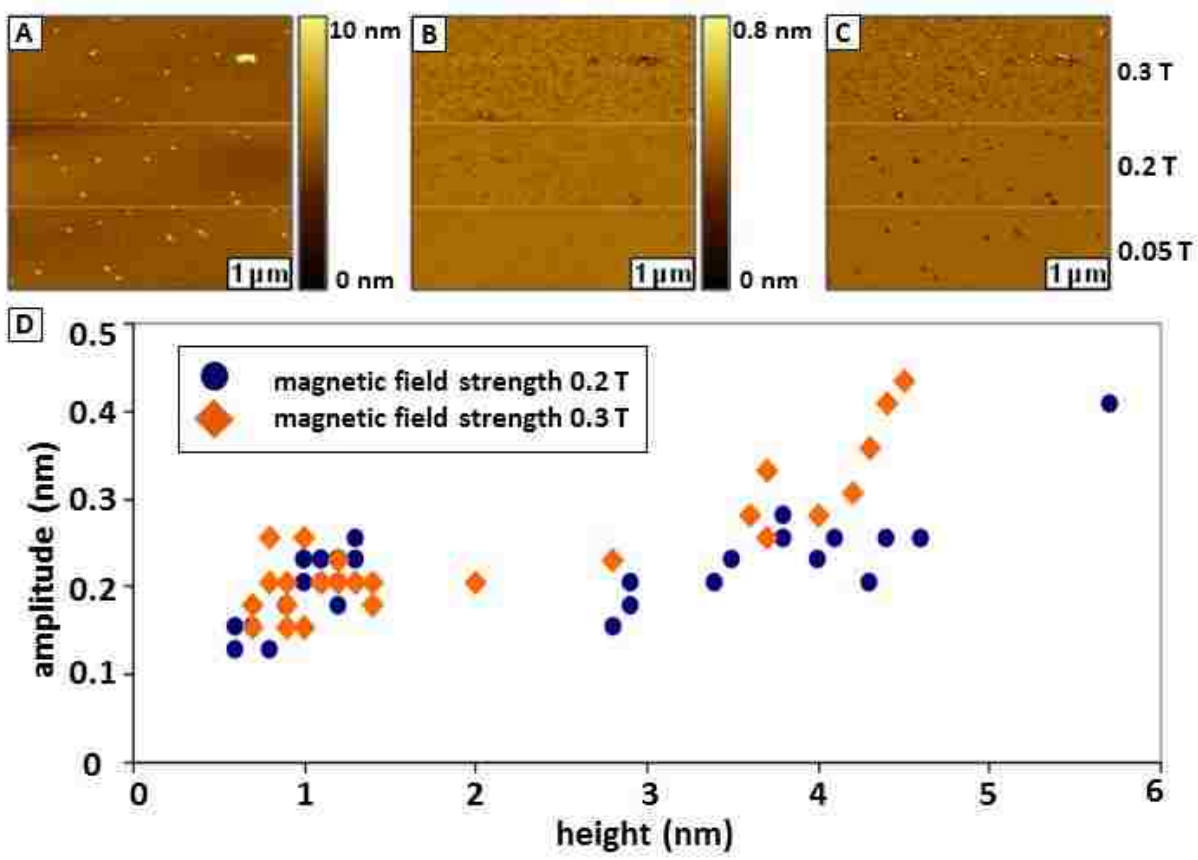

Figure 3.5 Nanoparticles of $FeNi_3$ prepared on mica substrates imaged with MSM-AFM using different field strengths. *(a)* Topograph and simultaneously acquired *(b)* MSM-amplitude and *(c)* MSM-phase frames. *(d)* Plot of the changes in tip displacement amplitude for different sizes of nanoparticles. *Reprinted with permission from reference 57.*

3.4 MSM-AFM Studies of iron oxyhydroxide nanostructures prepared by electroless metal deposition

Since MSM-AFM investigations rely on the vibration and movement of the sample for magnetic studies, imaging nanoparticles that are loosely bound on a flat surface can be challenging. At higher field strengths, the nanoparticles may vibrate too much and become displaced from the surface.

To address this problem, a possible strategy is to anchor nanomaterials to the endgroups of self-assembled monolayers (SAMs) to provide a robust chemical linkage to the surface.[134, 185] Organosilane SAMs were used as linker groups for anchoring metal deposits and yet still enabled

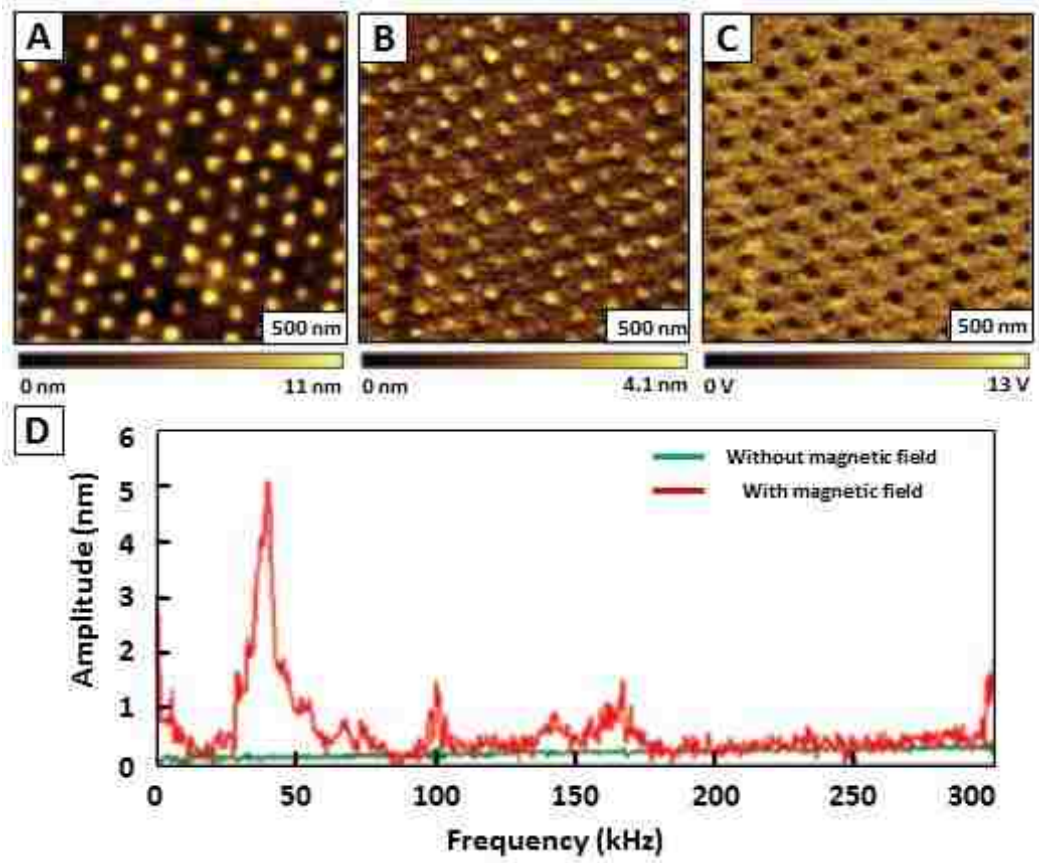

Figure 3.6 Nanostructures of iron oxide hydroxide prepared on organosilane nanopatterns imaged using MSM-AFM. Images acquired in the presence of a magnetic field: *(a)* Topography; *(b)* MSM-amplitude and *(c)* MSM-phase image. *(d)* Spectra from a frequency sweep when the tip was placed in contact with a vibrating area of the sample. *Reprinted with permission from reference 135.*

a spring-like response for the motion of nanoparticles for MSM-AFM investigations. Iron most commonly exists as oxide, hydroxide, and oxyhydroxide in forms including iron (II) oxide (wustite), iron (II, III) oxide (magnetite), iron (III) oxide (maghemite and hematite), and iron (III) oxide hydroxide (lepidocrocite).[186] For the next example, paramagnetic iron oxide

hydroxide (lepidocrocite) was patterned onto multifunctional silane SAMs for MSM-AFM studies (Figure 6).

An array of Fe_3O_4 deposits prepared on organosilane nanopatterns is demonstrated in Figure 3.6 for MSM-AFM studies. Regular rows of metal dots are observed throughout areas of the surface arranged with a periodicity of 208 ± 12 nm. The height of the iron oxide hydroxide nanostructures measured 10 ± 3 nm, and the lateral dimensions of the dots measure 56 ± 10 nm. The topograph shown in Figure 3.6a is representative of multiple areas of the patterned sample. The sample was prepared with nanopatterns of mercaptopropyltrimethoxysilane (MPTMS) within a matrix SAM of methyl-terminated octadecyltrichlorosilane (OTS) to spatially direct the electroless deposition of iron. The nanodots of iron oxyhydroxide deposits attached selectively to the sulfur-terminated sites of MPTMS, and are surrounded by a resist layer of OTS.

For characterization of the nanodots with MSM-AFM, a frequency of 42 kHz and field strength of 0.29 T was applied for the results of Figure 3.6. The topography frame of Figure 3.6a provides information of the sizes, shapes and arrangement of the nanodots within an area of 2×2 μm2 showing 117 nanostructures. The MSM-amplitude and MSM-phase images clearly resolve the locations of magnetic areas of the sample (Figures 3.6b and 3.6c). The amplitude response correlates with the magnitude of the tip deflection in the z-direction, on the order of 1 to 4 nm.

A representative frequency spectra obtained with MSM-AFM is shown in Figure 3.6d. To acquire such spectra, the tip was parked on a specific location of the vibrating sample to map changes in tip deflection (amplitude) during a sweep of selected frequencies. Depending on the size and composition of the areas where the tip is placed, the frequency sweeps provide a way to detect mechanical tip-sample resonance. Such spectra provide a convenient means to evaluate the experimental parameters for choosing the optimal driving frequency and field strength for

MSM-AFM imaging with high sensitivity. The resonance spectrum in Figure 3.6d displays multiple broad peaks in the presence of an applied AC electromagnetic field (red line) when placed in contact with the metal nanostructures. When the tip does not have a field applied there were no prominent peaks (green line). In this example, the maximum resonance was detected at 42 kHz, which is different than the natural resonance of the cantilever (28 kHz). The frequency chosen for imaging samples with MSM-AFM should be selected at a resonance band to obtain high sensitivity.

3.5 Superparamagnetic nanostructures of ferritin studies with MSM-AFM

The iron storage protein ferritin is an excellent nanoscale model biomaterial because of unique properties and exquisitely regular, small dimensions.[187] The protein ferritin has dual functions of iron storage and release for maintaining appropriate levels of iron in blood. Since first isolated over 70 years ago, the structure of ferritin, the composition of the outer shell, and the function and properties of ferritin have been well characterized.[188-190] Ferritin is a globular protein consisting of a nearly spherical shell. The 450 kDa protein cage of ferritin has an inner diameter of 6-8 nm, which can contain up to 4500 iron atoms.[191] The iron atoms encapsulated by ferritin are temporarily stored as iron (III) oxy-hydroxide. Each Fe (III) atom is surrounded by six oxygen atoms. Studies of the magnetic properties of the iron core of ferritin have shown that the electron spin magnetic moment of the individual Fe (III) ions within the core are antiferromagnetically coupled (spin paired), which gives superparamagnetic behavior.[192]

Magnetic modes of scanning probe microscopy have been used to study ferritin. Since the core contains superparamagnetic iron oxide, ferritin has not been a significant focus for MFM studies. However, it has been demonstrated that MFM can be applied to study the properties of superparamagnetic nanoparticles when an external field is applied to the sample. The feasibility

of MFM for detecting 10 nm superparamagnetic iron oxide nanoparticles within ferritin was demonstrated by Schreiber, et al. by applying an in-plane external magnetic field to the sample.[193] A magnetic field of a few tens of millitesla was found to be sufficient to induce a stable magnetic dipole in ferritin to enable imaging with MFM at room temperature.

Ferritin, when deposited on a surface, tends to aggregate and form clusters. Self-aggregation of biomolecules on surfaces can be problematic for nanoscale measurements with AFM. Surface aggregation prevents the scanning probe from penetrating between protein clusters, thus the true morphology of the individual molecules maybe difficult to resolve. Nanolithography provides advantages for AFM measurements, offering approaches to isolate and segregate individual proteins and nanoparticles. Reproducible test platforms of proteins and nanoparticles can be prepared using particle lithography, to enable ultrasensitive surface measurements with SPM.[114, 194-196]

The response of the ferritin to an actuated magnetic field was investigated using MSM-AFM by Daniels, et al.[133] Examples of ring nanostructures of ferritin prepared with particle lithography are demonstrated in Figure 3.7, prepared from 500 nm silica mesospheres.[133, 195] To prepare the surface structures, monodisperse beads of colloidal silica were mixed with an aqueous solution of ferritin (5 mg/mL) and deposited directly on freshly cleaved mica(0001).[195] As the solution dried, the mesospheres assembled into a close-packed crystalline layer with ferritin molecules surrounding the base of the spheres in the meniscus sites. The template of silica beads was selectively removed by rinsing with water; however, the proteins persisted and remain attached to the substrate to form a periodic arrangement of ring structures for a single protein layer. The diameter of the mesospheres and the ratio of proteins to mesospheres determine the surface coverage and density of protein nanostructures.[194, 195]

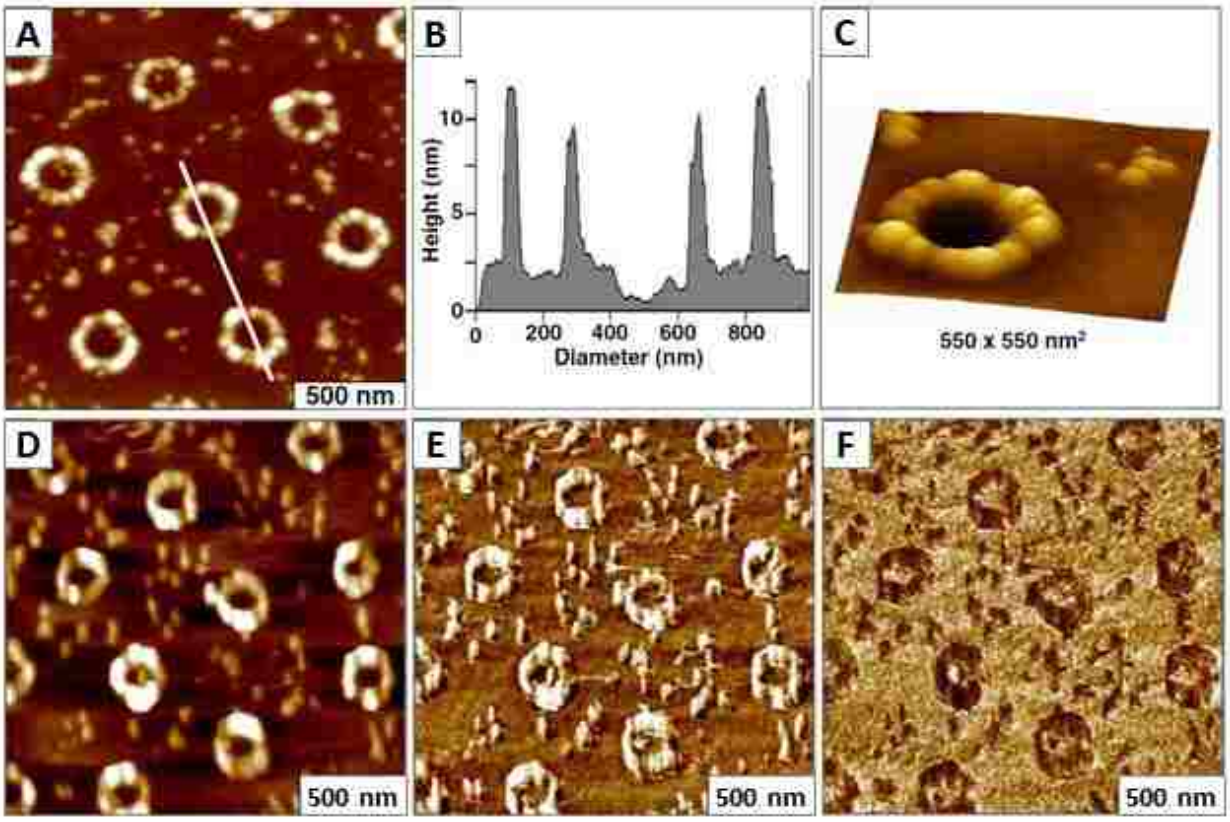

Figure 3.7 Arrangement of ferritin rings prepared on mica substrates using particle lithography. *(a)* Topography image acquired with tapping-mode AFM; *(b)* corresponding height profile; *(c)* close up view of a single ring of ferritin. MSM-AFM images indicate the vibration of ferritin in the presence of an AC magnetic field. *(d)* Topograph; *(e)* corresponding MSM-amplitude, and *(f)* MSM-phase images. An applied AC electromagnetic field measuring 0.2 T at 96 kHz was used to acquire MSM-AFM images d-f. *Reprinted with permission from reference 64.*

Seven rings of ferritin arranged in a hexagonal pattern are shown in the tapping-mode topography frame of Figure 3.7a. A few isolated proteins are randomly located in areas between the rings. Rings of protein formed within the 2×2 μm2 area are spaced with an average periodicity measuring 500 ± 36 nm, which matches the diameter of the silica mesospheres used as a surface template.

A representative line profile across two of the patterns (Figure 3.7b) indicates the height measures 11 ± 2 nm, which closely matches the expected size (10-12 nm) of ferritin reported previously.[187, 197] A single ring nanopattern is viewed in Figure 3.7c, comprised of approximately

16 individual ferritin molecules. Depending on the iron content encapsulated within the nanocage of the protein shell, the sizes and shapes of ferritin are not perfectly uniform, as evidenced in the AFM topography frames. The regular arrangements of protein rings prepared with particle lithography provide a useful test structure for studies with MSM-AFM.

The iron cores of ferritin provide a natural, well-defined reference sample for magnetic AFM studies. The location of ferritin molecules can be sensitively detected using MSM-AFM. When a modulated electromagnetic field is applied to the sample, the proteins are induced to vibrate according to the corresponding rhythm and periodicity of the electromagnetic field (Figure 3.7d). The AFM tip operated in contact mode serves as a force and motion sensor to detect the vibration of the sample. Ferritin is driven to vibrate according to designated experimental settings in response to the electromagnetic field, and therefore needs to be securely anchored to the surface to prevent displacement. A requirement for imaging with MSM-AFM is that the sample be movable without detaching from the surface. The core of ferritin is encapsulated by a protein cage, which remains securely attached to the surface. Comparing the topography frames before and after sample modulation (Figure 3.7a compared to Figure 3.7d) the sample motion leads to a broadening effect. The surface features appear to be wider and taller when vibrating. The vibration of the samples causes a distortion and elongation of the true dimensions of ferritin; thus, the field must be turned off for accurate topography characterizations.

The location of the ferritin rings as well as individual molecules located between the rings can be readily detected in both MSM-amplitude and MSM-phase frames, which are acquired concurrently with the topography channel. The changes in phase angle and amplitude of

the motion of the tip as it interacts with the vibrating sample can be plotted pixel-by-pixel as a function of tip position to generate MSM-phase and MSM-amplitude images.

The specific motion tracked with MSM-amplitude and MSM-phase images are shown in Figures 3.7e and 3.7f, respectively.[133] Phase and amplitude images can be used to distinguish the magnetic and nonmagnetic areas of the sample. Phase images with MSM are generated by mapping changes in the response of the AFM tip compared to the reference sine waveform applied to drive the sample modulation. Amplitude frames display changes in the magnitude of the tip oscillation compared to the reference signal. The magnitude of the changes in the amplitude response corresponds to changes in the tip deflection in the z-direction. The amplitude response was scaled in nm, to indicate the relative changes in tip displacement as the probe interacts with vibrating nanostructures.

3.6 Dynamic studies with MSM-AFM

The parameters of frequency and field strength can be systematically changed during scans with MSM-AFM. For example, as the field strength is gradually increased, the images disclose further details of the response of smaller nanomaterials (Figure 3.8). Iron oxide nanoparticles were deposited within surface patterns of an octadecyltrichlorosilane SAM. The topography frame reveals rows of surface deposits, which are barely resolvable based on differences in height (Figure 3.8a).

The locations of the clusters of nanoparticles are displayed more clearly in the simultaneously acquired lateral force frame (Figure 3.8b). Depending on the size of the nanoparticles, smaller nanomaterials can be detected at higher field strengths, as revealed in the MSM-amplitude and MSM-phase channels of Figures 3.8c and 3.8d.

The amplitude images scale proportionately to the strength of the applied electromagnetic field, increasing intensity is detected for the image contrast as the field is ramped. However, the MSM-phase images do not scale accordingly; the image sections at the highest field strengths of 0.23 and 0.27 T were weaker in intensity than at 0.12-0.18T. Thus an increase in amplitude does not necessarily lead to larger shifts in the phase angle of the vibration of the samples measured by a lock-in detector.

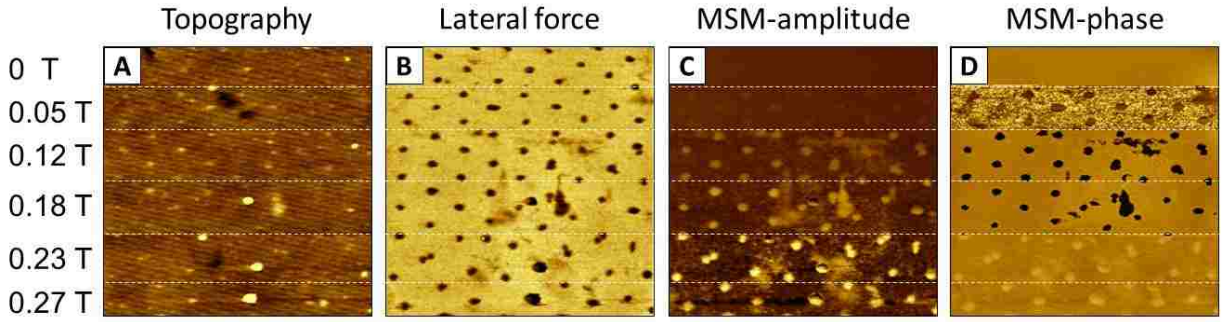

Figure 3.8 The sensitivity of MSM-AFM increases as the field strength is increased during a scan. Clusters of iron oxide nanoparticles were arranged in a periodic pattern using OTS surface templates. White lines were drawn on top of the images to indicate the points at which the field strength was changed. *(a)* Topography frame, 2×2 μm^2; *(b)* corresponding lateral force channel; *(c)* MSM-amplitude and *(d)* MSM-phase images.

Another capability for MSM-AFM protocols is to park the tip in contact with a vibrating area of the surface to acquire frequency spectra for individual nanocrystals at different field strengths, as shown in Figure 3.9. Sufficient force must be applied to the tip to hold the probe in contact with the vibrating nanoparticle. Typically, the spectra will reveal a prominent resonance peak and multiple smaller peaks, depending on the complexity of the sample. In the example of Figure 3.9, a cluster of several iron oxide nanoparticles produced complicated spectra of multiple resonance peaks. However, as the field strength was ramped, the peak locations broaden but do not change position. The field-dependent spectra indicate the physical resonances of the

vibration of both the tip and sample, profiling the magnetic response of individual nanoparticles or clusters of nanoparticles directly beneath the AFM probe.

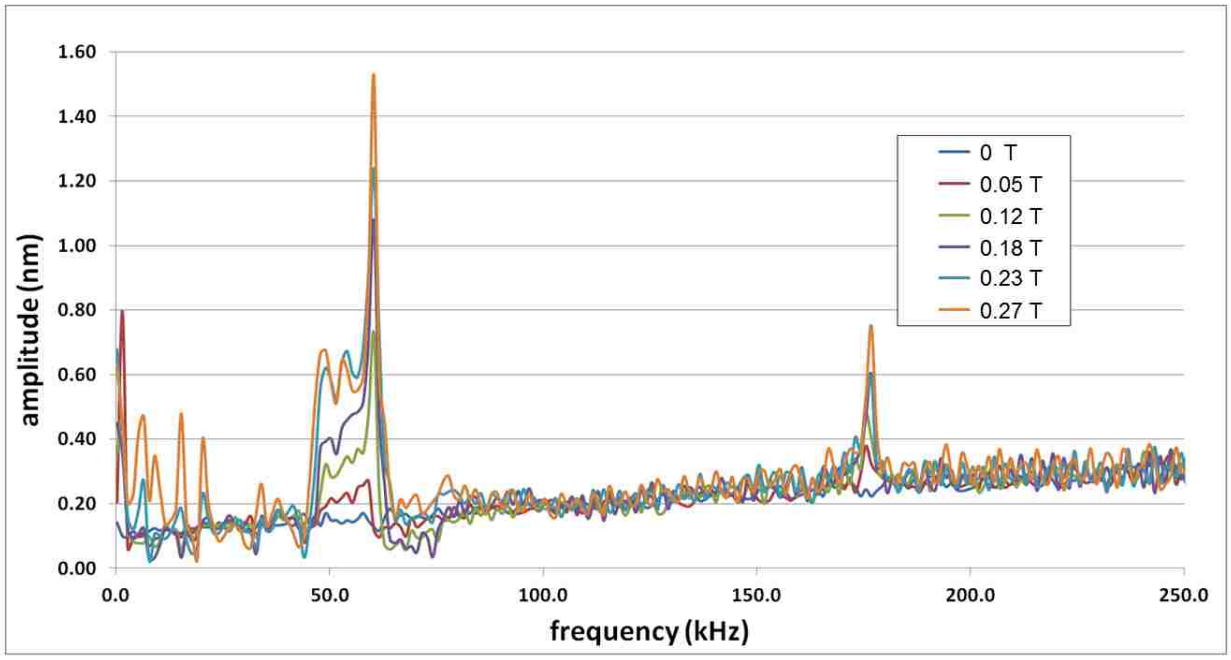

Figure 3.9 Representative frequency spectra acquired with the sample shown in Figure 8. As the electromagnetic field strength is successively increased, the amplitude of the resonance peaks increased proportionately and became broader. However, at higher fields the peaks did not shift position.

3.7 Prospectus for future investigations with MSM-AFM

Magnetic sample modulation can be applied for studies of magnetic nanoparticles, iron-containing proteins and magnetic nanostructures. In addition to mapping magnetic nanomaterials with exquisite resolution, MSM-AFM can be used to acquire dynamic information regarding how the samples respond to an external magnetic field with frequency changes. Future directions for studies with MSM-AFM studies will be to measure and model how the mechanical vibration signatures of nanoparticles change with composition, size, and magnetic field parameters, e.g. frequency, field strength. Also, it should be possible to study the cooperative effects of coupling between adjacent nanoparticles within discrete arrangements on surfaces using MSM-AFM.

Magnetic bioconjugate nanoparticle labels can be used to study uptake, immune response and certain types of bioactivity at the level of individual cells, using MSM-AFM. Essentially, labels of fluorescent materials in bioassays could be exchanged with magnetic tags for more sensitive imaging and visualization of biological processes, at the resolution limits of scanning probe microscopy. A key strategy for MSM-AFM experiments was to use particle lithography to prepare arrays of nanostructures as well-defined test platforms with tunable sizes and spacing. Millions of nanostructures can be prepared reproducibly on surfaces with relatively few defects to enable multiple successive measurements with different imaging modes of AFM. Custom test platforms were prepared using particle lithography to facilitate AFM characterization at the level of individual nanoparticles or proteins.

When conducting AFM experiments, the dynamic conditions of the applied field strength, the force applied to the AFM probe and the frequency parameters can be systematically varied to visualize changes in the magnetic response using MSM-AFM for characterizations at the level of individual nanoparticles or nanostructures. Changes of certain experimental parameters such as the driving frequency and the applied magnetic field strength directly influence the vibrational response of samples when imaging with MSM-AFM.

The results at the level of single nanoparticle measurements suggest intriguing possibilities for characterizations with MSM-AFM and add a magnetic dimension to scanning probe methods for identification of magnetic nanomaterials. Although we have not satisfactorily addressed the question of whether MSM-AFM imaging can be used to discriminate differences in magnetic response for nanoparticles of different composition, it is clear that changes for different sized nanoparticles can be quantitatively evaluated. As with most measurements, the very small sizes of the nanoparticles pose a challenge for surface measurements, however, the

results establish a precedent for detecting magnetic response of individual nanoparticles using MSM-AFM. We anticipate that using AFM tips with softer spring constants will provide a means to more clearly resolve differences for magnetic nanoparticles of different composition and size. In future experiments strategies will be developed to analyze mixtures of magnetic and non-magnetic nanomaterials or mixtures with different types of magnetic character, e.g. superparamagnetic versus ferromagnetic. Further quantitative protocols will be developed for obtaining frequency sweeps with individual nanoparticles of different sizes under selected conditions of AC field strength and load force.

CHAPTER 4: INVESTIGATION OF MAGNETIC NANOPARTICLES USING MSM-AFM

4.1 Introduction

The magnetic properties of nanomaterials are size dependent, and do not necessarily scale down proportionately compared to bulk materials. As materials shrink to smaller and smaller sizes, most of the atoms become surface atoms causing surface effects to dominate properties.[151] Physical relationships such as the size, morphology, and surface structure determine the magnetic properties of the nanoparticles. Fundamental magnetic properties such as blocking temperature, magnetic susceptibility, and coercivity are all influenced by size effects.[198-200] Investigations of magnetic nanomaterials are often based on studying properties for an average of multiple measurements. Relatively small changes in size have been known to sensitively affect the absorbance wavelength of CdSe quantum dots.[201] A change in size of only 1.5 nm can shift the absorbance wavelength by 40 nm. The ability to assess magnetic properties of nanomaterials on the basis of an individual nanoparticle will provide insight into how size scaling influences the properties of nanomaterials.

High resolution investigations of the surface properties and morphology of individual nanomaterials are routine characterizations with modes of scanning probe microscopy (SPM).[15, 122] The modes of SPM can be categorized by the types of forces that are measured (i.e. adhesion, repulsion, electrostatic, friction, electrical, chemical, and magnetic). Magnetic forces of samples are most commonly probed using magnetic force microscopy (MFM) mode of AFM. Magnetic sample modulation AFM (MSM-AFM) has been demonstrated to overcome the resolution limits associated with MFM. Operated in conventional contact mode, a non-magnetic lever is used as a force and motion sensor to detect the movement of the magnetic nanomaterials.[133, 134] An AC electromagnetic field is applied to the sample with a solenoid placed beneath the sample stage.

The magnetic nanomaterials of the sample are selectively driven to vibrate. As the AFM tip comes into contact with a vibrating nanomaterial, the vibration of the sample is sensed by the AFM probe. Changes in the amplitude and phase of the tip motion are sensitively detected with a lock-in amplifier and compared to the driving signal to generated MSM amplitude and phase images.

Two samples of nanoparticles were characterized with MSM-AFM. The first sample consists of 0.8 nm $FeNi_3$ nanoparticles synthesized with microwave heating. The second sample consists of iron oxide nanoparticles which are larger in size at 18 nm. Dynamic and static measurements of the magnetic nanostructures were acquired using MSM-AFM.

4.2 Nanoparticles of $FeNi_3$

4.2.1 Microwave synthesis and characterization of iron nickel nanoparticles

Iron nickel has previously been synthesized through both coprecipitation and solvothermal methods to produce spheres,[202] dendrites,[203] and platelets.[204] Microwave synthetic methods are solvothermal methods that generate more even heating with precise control over pressure and temperature.[179, 205-207] Control of synthesis parameters produces nanoparticles with better monodispersity than hotplate methods. A hydrothermal method of synthesis was used to synthesize $FeNi_3$ nanoparticles using microwave heating.[184]

Water is used as a solvent to generate high temperatures and pressures with hydrothermal methods.[208, 209] Higher temperatures and pressures increase the solubility of metal precursors, and enhance the effect of reducing agents by decreasing reduction potentials (E_o). For example, hydrazine hydrate (E_o=-0.2) can be used to reduce iron (II) (E_o= -0.4) in sealed reaction vessels at 180 C.[184] Hydrothermal methods are used to prepepare nanoparticles that are crystalline and do not require further annealing. Microwave irradiation has recently been shown to produce

highly monodisperse particles with short reaction times.[182] Microwave heating enables precise control of temperature parameters to achieve uniform and rapid heating of the reaction solution. Hydrothermal synthesis was accomplished in a sealed microwave vessel, monitoring the temperature and pressure within the container with sensors. The solution was assembled under an argon atmosphere to prevent forming magnetite (Fe_3O_4). Metallic precursors include both Fe^{2+} and Ni^{2+} sources mixed in a 1:3 ratio, respectively. Hydrazine hydrate was used as a reducing agent under basic conditions at a reaction temperature of 180 C.

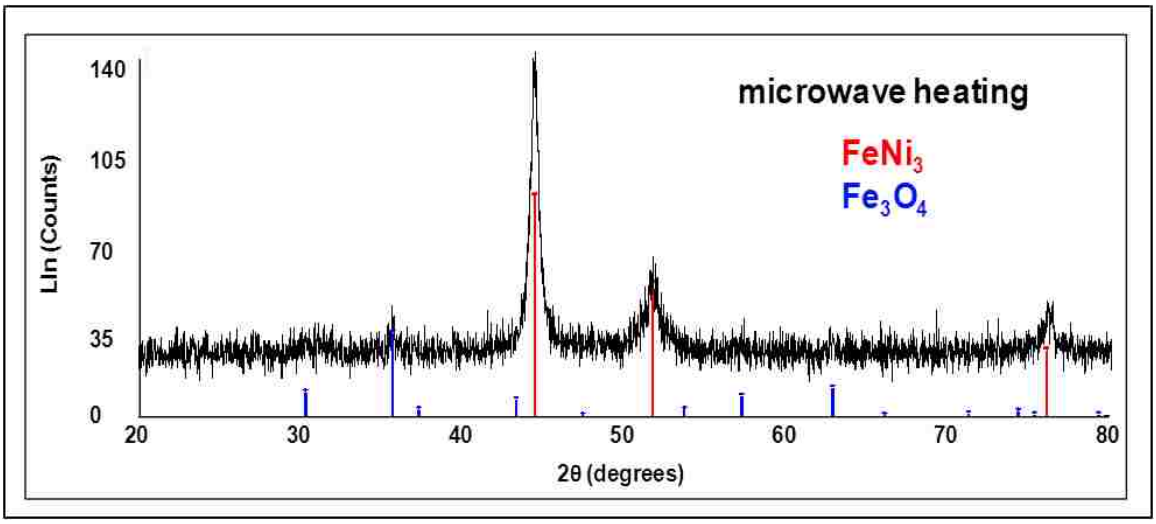

Figure 4.1 XRD spectrum of $FeNi_3$ nanoparticles prepared by microwave heating.

The nanoparticles were identified to be crystalline $FeNi_3$ using powder X-ray diffraction (XRD). An example powder diffraction pattern for the microwave synthesis of $FeNi_3$ is shown in Figure 4.1. The red lines indicate peaks at 2θ = 44.2, 52.5, and 76.2 degrees for the indexed spectra of the $FeNi_3$ phase. Blue peaks at 2θ = 30.1, 35.4, and 62.5 degrees index the peaks associated with Fe_3O_4 (magnetite- a common contaminant found with Fe nanoparticle reduction). The amount of magnetite present after heating has been reduced by using an Fe^{2+} metal precursor with an inert atmosphere. Broader peaks in the XRD spectrum indicate the presence of nanosized particles and dimensions can be estimated with the Debye- Scherrer equation.[210] According to

this formula, the particles shown in Figure 1 have an average size of 30 nm for the (111) plane, and a size of 46 nm for the (002) plane.

Tapping mode (AC AFM) was used to determine the size of the nanoparticles on a local scale. Samples for AFM studies were prepared by dispersing the nanoparticles in water and placing a 15 µL of the solution onto freshly cleaved mica(0001) substrates. Representative topography images of the $FeNi_3$ nanoparticles on mica are shown in Figures 4.2a and 4.2d. The heights of the nanoparticles were determined by acquiring height profiles of individual nanoparticles, such as the example shown in Figure 4.2g. The cursor profile indicates that the nanoparticles measure ~0.8 nm in diameter.

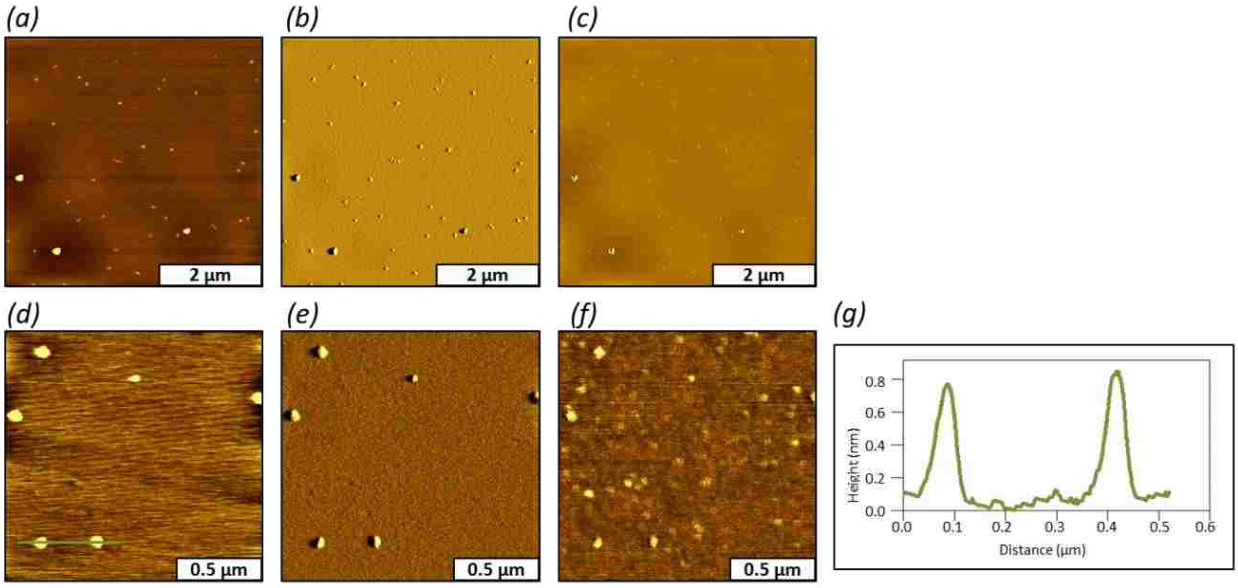

Figure 4.2 Nanoparticles composed of $FeNi_3$ were deposited on mica for analysis with tapping mode AFM. Wide area view of simultaneously-acquired (*a*) topography, (*b*) amplitude, and (*c*) phase images. Zoom-in view of (*d*) topography, (*e*) amplitude, and (*f*) phase frames. (*g*) Cursor profile for the line in ***d***.

The average results of 90 cursor profiles from five AFM images are plotted Figure 4.3. The sizes of the nanoparticles range from 0.2 nm to 1.1 nm nm, with most of the nanoparticles

measuring 0.8 ± 0.2 nm. Since AFM is a local technique, results do not necessarily correspond with the sizes determined from the Debye-Sherrer equation for XRD.

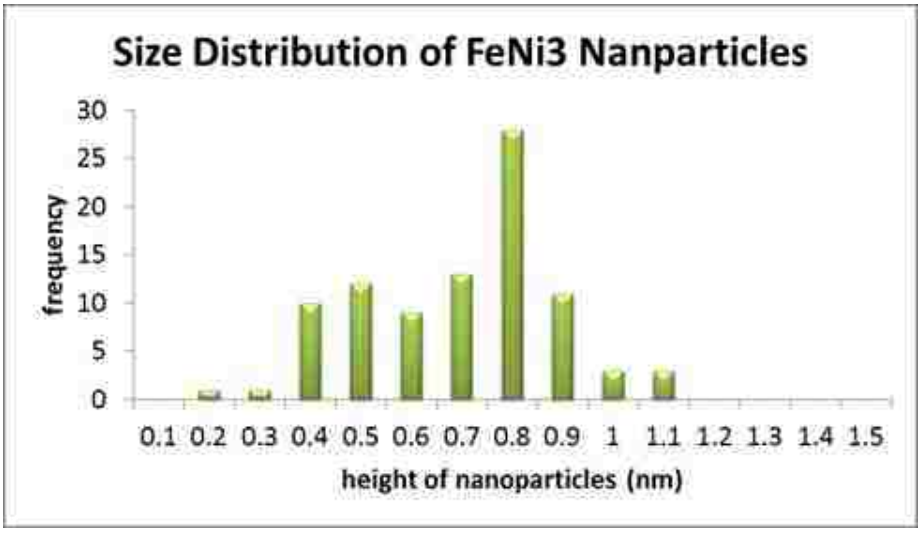

Figure 4.3 Histogram of the heights of $FeNi_3$ nanoparticles determined by AFM.

Transmission electron microscopy (TEM) was used to characterize the nanoparticle dimensions. Results from images acquired with TEM show that nanoparticles synthesized by microwave synthesis self-aggregate into chains of nanoparticles. Two distinct sizes of $FeNi_3$ nanoparticles are noticeable with TEM. Larger aggregates measuring 500 nm or larger are apparent in Figure 4.4a. With greater magnification, smaller nanoparticles within the aggregate clusters can be detected in Figure 4.4b. The sizes of the nanoparticles more closely correlate with dimensions obtained from the Debye-Sherrer equation. A typical energy dispersive X-ray spectrum obtained for $FeNi_3$ nanoparticles is shown in Figure 4.4c for the nanoparticles. The atomic percentages of Fe and Ni in the nanoparticles were found to be 13.8 and 67.6, respectively. The stoichiometric formula for the sample is shown in Figure 4.4d. This data suggests that we have not synthesized the $FeNi_3$ intermetallic, but rather a $FeNi_5$ alloy. However, the presence of iron oxide nanoparticles within a mixture also influences the ratio.

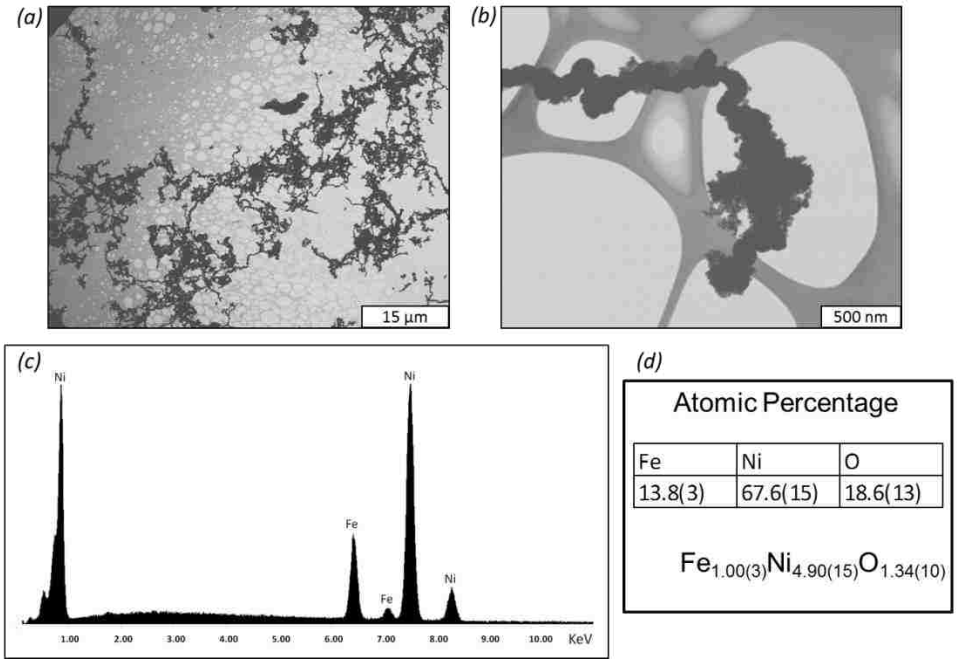

Figure 4.4 Nanoparticles of $FeNi_3$ viewed with TEM micrographs. (*a*) Chaining and aggregation of magnetic nanoparticles; (*b*) magnified view of a cluster of nanoparticles; (*c*) EDX analysis; (*d*) ratio of elemental analysis averaged for the sample.

4.2.2 MSM-AFM of microwave synthesized bimetallic nanoparticles

Nanoparticles composed of $FeNi_3$ that were prepared by microwave synthesis were characterized with MSM, as shown in Figure 4.5. Samples were deposited on mica from dilute solutions of the nanoparticles in deionized water. During MSM imaging, topography, amplitude, and phase images are generated simultaneously in the presence of an applied magnetic field. The magnetic nanoparticles can be distinguished in the topography image as well as in the MSM amplitude and phase channels shown in Figure 4.5a. When the magnetic field was switched off, on, and off again during a single scan the amplitude and phase channels correspondingly changed (Figure 4.5b). The tip was scanned in continuous contact with the sample from left to right in a raster pattern, with the tip advancing at small increments in the y-direction. When the magnetic field was turned off, the nanoparticles did not vibrate, and no contrast was observed in the MSM amplitude and phase frames. When the magnetic field was turned on, changes are

immediately visible in the MSM amplitude and phase images. The area in between the dotted lines represents the points in the linescans where the field was turned on. The contrast disappears when the field is switched off again. The nanoparticles with an average size of 0.8 nm are some of the smallest nanoparticles detected using MSM-AFM.

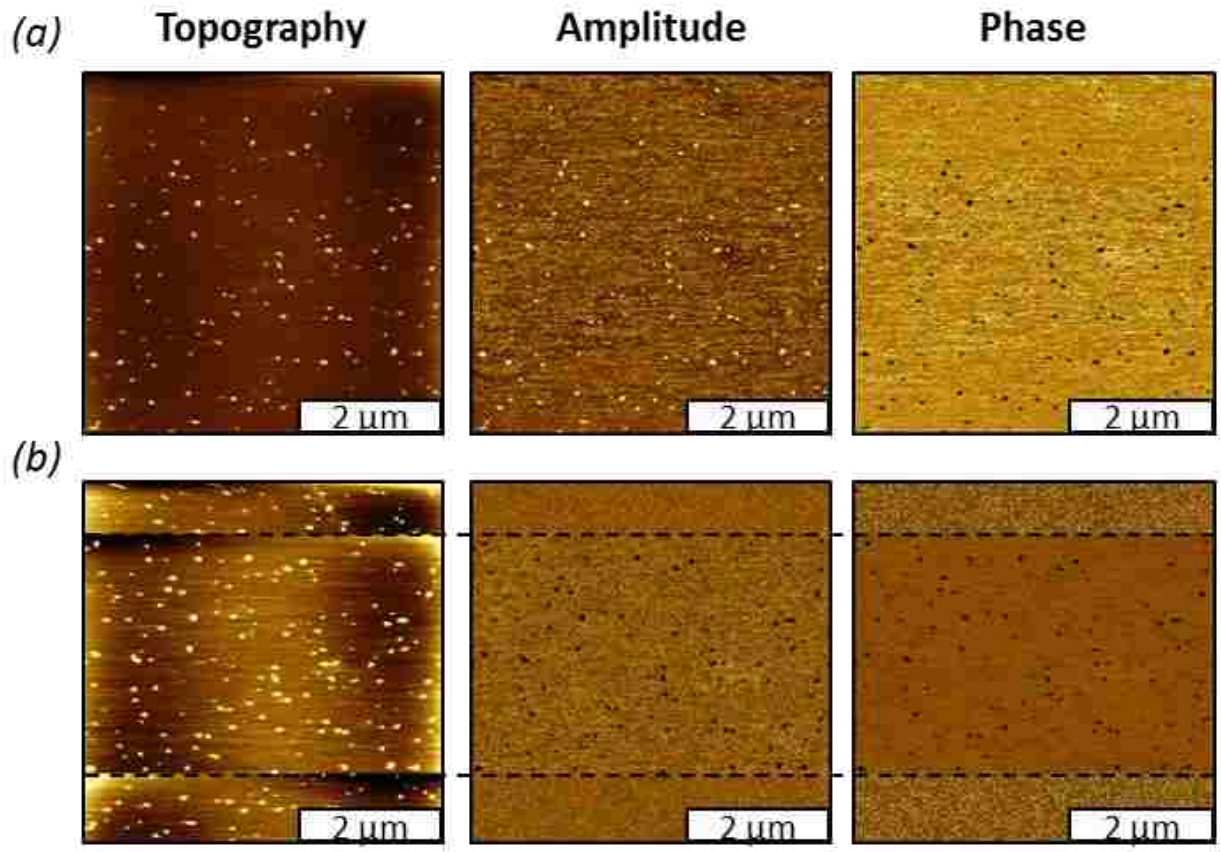

Figure 4.5 Nanoparticles composed of $FeNi_3$ prepared on mica imaged with MSM-AFM. (*a*) A magnetic field of 0.6% was used to acquire MSM images. (*b*) Image acquired while the field was switched off and on.

Trends of the changes in z-displacement with changes in the size of the nanoparticles are shown in Figure 4.6. The plot was generated using cursor profiles from both topography and MSM amplitude images. The x-axis identifies the height of the nanoparticles with respect to the displacement of the AFM probe. Displacement of the AFM probe is calculated from the cursor

profiles from the MSM amplitude images. The trend reveals that larger nanoparticles correspondingly have a greater amplitude response.

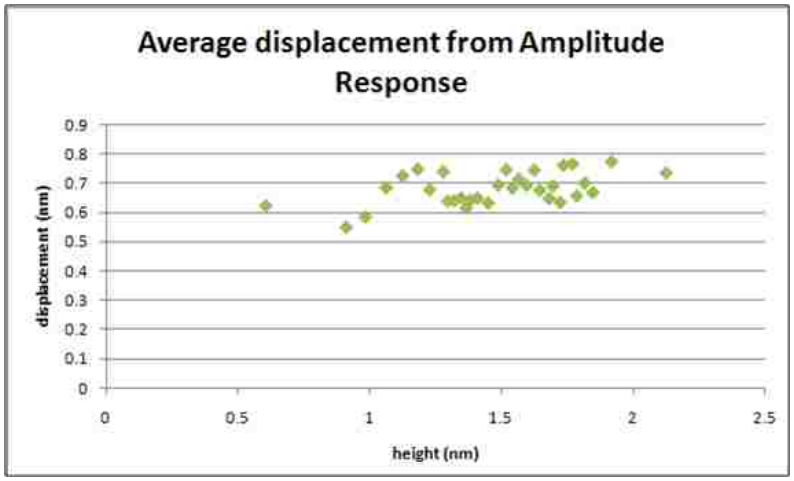

Figure 4.6 Plot of the tip displacement due to nanoparticle vibration generated from cursor profiles of MSM amplitude images.

4.3 Scanning probe characterizations of iron oxide nanoparticles

Iron oxide nanoparticles are important for applications in bioassays,[211, 212] as magnetic contrasts agents for imaging,[154, 165], and as therapeutic agents.[213, 214] The use of iron oxide has become increasingly popular in biomedical applications due to this material's high biocompability and the ease with which the surface can be functionalized.[167] The magnetic properties of iron oxide are tunable depending on both the size and form of the iron oxide synthesized. It is important to understand the magnetic properties of the nanoparticles for magnetic imaging and *in vivo* manipulation for therapeutics.

4.3.1 Characterization of FeO/Fe_3O_4 nanoparticles using tapping mode AFM

A solution of core/shell FeO/Fe_3O_4 shell nanoparticles obtained from Argonne National Lab were deposited on mica using toluene and dried overnight. Tapping-mode AFM was used to characterize the size and morphology of the nanoparticles (Figure 4.7). An aggregate of about 88 closely packed nanoparticles is presented in Figures 4.7a and 4.7b. The dimensions of the

nanoparticles are quite uniform, measuring 18 nm in height, referencing the mica surface as a baseline (Figure 4.7c). The measurement from AFM cursor profiles matches well with data acquired by transmission electron microscopy (TEM).

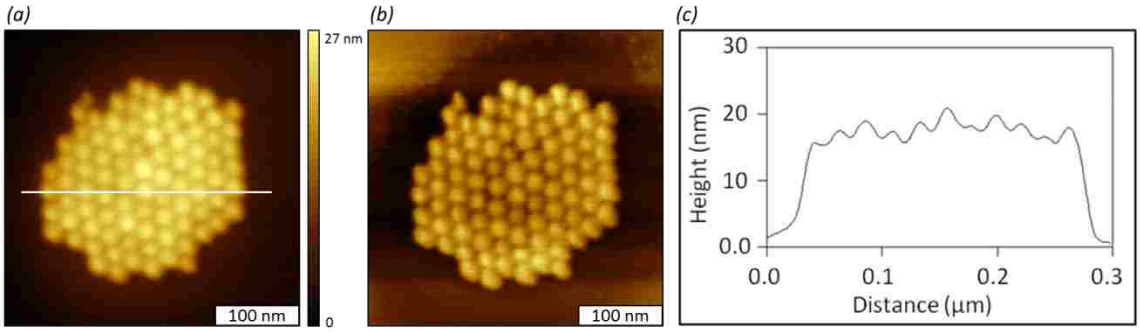

Figure 4.7 Cluster of iron oxide nanoparticles prepared on freshly cleaved mica and imaged with tapping-mode AFM. (*a*) Topography image of a single cluster of nanoparticles; (*b*) corresponding phase image; (*c*) Cursor profile for the white line in ***a***.

Images acquired with TEM indicate that the nanoparticles have a cubic morphology. Alternatively, AFM topographs in Figure 4.7 represent the nanoparticles as spherical shapes, due to tip-sample convolution. The round shape of the AFM probe is outlined rather than the true shape of the nanoparticles. When the nanoparticles were deposited on mica, drying of the toluene solution causes the nanoparticles to aggregate into a closed packed pattern (Figure 4.7). To investigate how FeO/Fe_3O_4 nanoparticles respond to a magnetic flux, the samples prepared on mica substrates were investigated using MSM-AFM.

4.3.2 Magnetic sample modulation investigation of FeO/Fe_3O_4 nanoparticles prepared on mica

Magnetic sample modulation AFM is operated in continuous contact mode using a force setpoint as a feedback. Details of the instrument setup and operation for MSM-AFM is provided in Chapter 3. A solenoid placed underneath the sample stage is used to generate an AC electromagnetic field at the sample. Magnetic domains on the sample vibrate in response to the flux of the oscillating magnetic field. A soft, nonmagnetic tip (k = 0.005 N/m) is scanned across

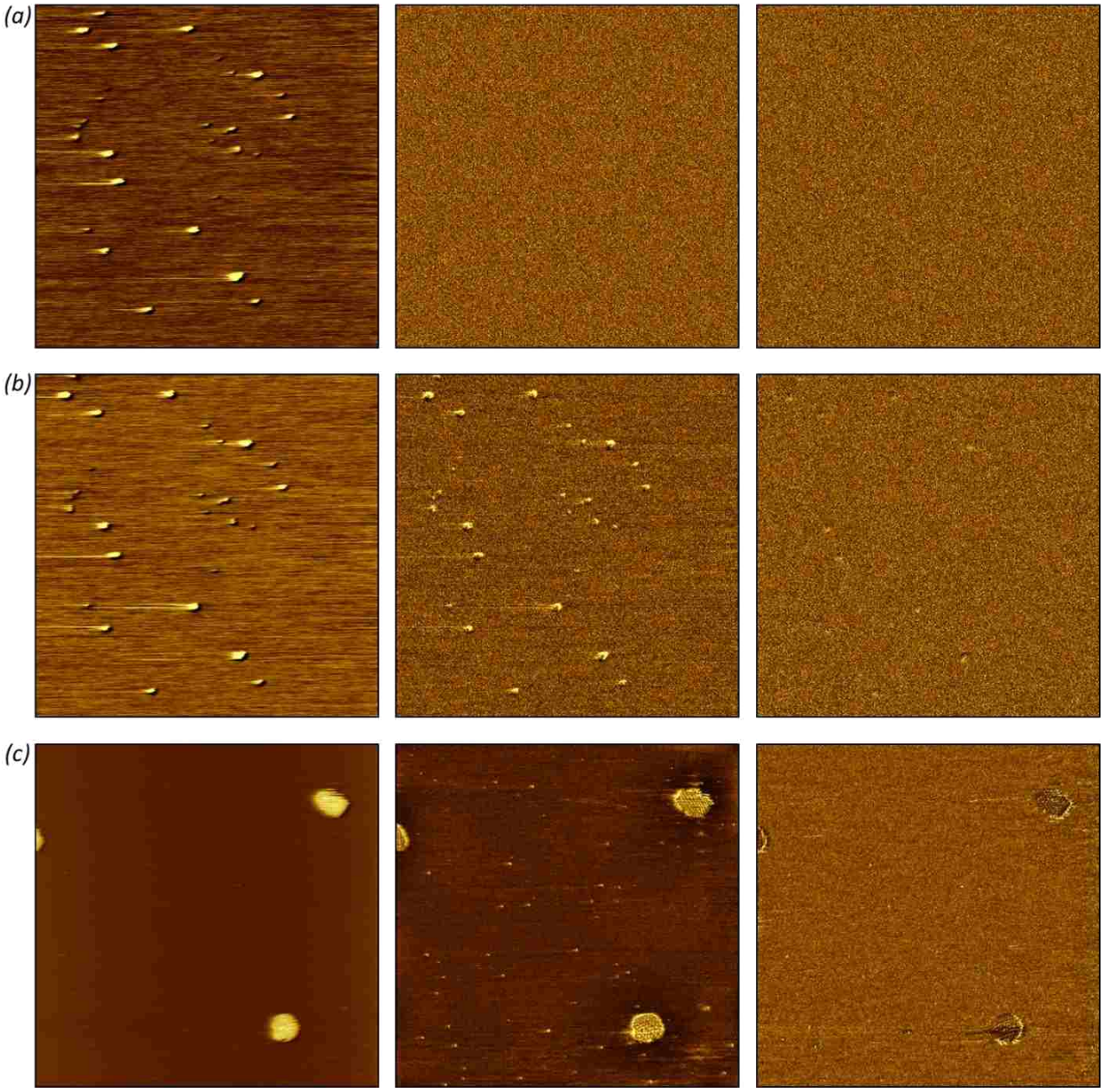

Figure 4.8 Magnetic sample modulation (MSM) images of iron oxide nanoparticles. (*a*) Contact-mode AFM images acquired without a magnetic field (700 × 700 nm^2); (*b*) the same area imaged with MSM-AFM with an oscillating magnetic field; (*c*) Larger view imaged with MSM (2 × 2 μm^2). From left to right, the images correspond to topography, MSM amplitude, and MSM phase.

the surface in contact mode. When the tip comes into contact with the oscillating sample, the tip vibrates in response to the motion of the vibrating sample. Lock-in amplifiers sensitively detect

the amplitude and the phase shift of the AFM tip as it vibrates. Changes of the amplitude and phase of the tip motion provide MSM phase and MSM amplitude images. The operating principle is quite similar to the Force Modulation Microscopy mode of AFM, in which the entire sample is driven to vibrate against the AFM probe to measure elastic response. However, for MSM-AFM, the magnetic domains are selectively driven to vibrate by the external electromagnetic field.

Without applying a magnetic field, the images are essentially contact mode frames. A control sample is shown in Figure 4.8a revealing that MSM-amplitude and MSM-phase channels do not disclose sample information in the absence of a magnetic field. The shapes of the nanoparticles are visible only within the topography frame; however line spikes were produced by the tip pushing the samples across the flat mica substrate. When the magnetic field was turned on at a frequency of 54.1 kHz, the shapes and positions of the magnetic nanoparticles are readily apparent in the MSM amplitude and MSM phase frames (Figure 4.8b). A large area view of the nanoparticles is presented in Figures 4.8c. Within the MSM-amplitude frame there are about 45 smaller nanoparticles visible that cannot be resolved in the topography image.

Characteriztion of the FeO/Fe_3O_4 nanoparticles with dynamic MSM-AFM measurements is presented in Section 3.6.

4.4 Conclusions and future directions

Studies with MSM-AFM will be developed to evaluate how composition and size affect the vibrational response of nanoparticles. Future studies with the synthesis of other oxide and bimetallic systems will be accomplished with MSM-AFM. Mixtures of magnetic nanoparticles with differing composition will be tested to compare resonant signatures that occur in response to

an applied magnetic field. The cooperative effects of proximity and magnetic coupling between adjacent nanoparticles on a surface will be studied with MSM-AFM.

CHAPTER 5: SPATIALLY SELECTIVE SURFACE PLATFORMS FOR BINDING FIBRINOGEN PREPARED BY PARTICLE LITHOGRAPHY WITH ORGANOSILANES[9]*

5.1 Introduction

Surface patterning is essential for the integration of biomolecules into miniature bioelectronic and sensing devices since the sensing element consists of a layer of biomolecules for the capture of target molecules and analytes. Micro- and nanoscale sensing devices require the immobilization of active proteins onto flat substrates.[215-217] Patterning of proteins has been accomplished at the micron level using microcontact printing,[92, 218] photolithography,[219-222] electron beam lithography[223-225] and microfluidic channels.[226, 227] Advancements for patterning proteins at the nanoscale on surfaces of self-assembled monolayers (SAMs) has been achieved using dip-pen nanolithography,[228-232] bias-induced oxidation lithography,[233, 234] imprint lithography[235, 236] and nanografting.[237-240] Innovative approaches for patterning proteins using particle lithography have also been reported, achieving high throughput across areas spanning mm to cm dimensions.[115, 194, 241-245]

In this study, we investigate the immobilization of fibrinogen on designed surfaces of nanopatterned organosilanes. Fibrinogen has a central role in both blood coagulation and blood-based infections and has been intensively studied because of its fundamental role in blood clotting, thrombosis, angiogenesis, wound healing, platelet adhesion and biocompatibility. [246-248] Surface studies using fluorescently-labeled fibrinogen were reported for micro-line patterns of 3-mercaptopropyltriethoxylsilane prepared by photopatterning. [249] Microcontact printing was used to directly stamp patterns of fibrinogen for studies of platelet adhesion and activation.[250]

* Chapter 5 previously appeared as Englade-Franklin, L. E.; Saner, C. K.; Garno, J. C. Spatially selective surface platforms for binding fibrinogen prepared by particle lithography with organosilanes, 2013. It is reprinted by permission of The Royal Society (see page 123).

Micropatterned domains of fibrinogen within a micropatterned surface film of serum albumin were detected using tapping-mode atomic force microscopy (AFM) by Soman et al.[251] Height and phase changes were used to map the regions containing fibrinogen after the patterns were infused with nanogold labels conjugated to antifibrinogen polycolonal antibody.

To further advance to molecular-level investigations of protein binding, technologies to produce even smaller patterns must be developed that enable control over protein density and orientation. Robust immobilization is required for AFM studies to prevent displacement of proteins by the motion of the scanning probe.[252] The chemistry selected for immobilizing biomolecules to surfaces should not use denaturing conditions that destroy the active protein structure. Miniaturization to the nanometer scale offers opportunities for studying surface-mediated biological reactions with AFM, particularly for investigating the parameters which influence mechanisms of protein activity, function and molecular recognition. The resolution of AFM is comparable to that of the electron microscope, however with additional benefits for studying proteins in liquid or ambient environments with minimal sample preparation.[43, 253-256] Studies of the conformational changes of fibrinogen attributed to effects of surface hydrophobicity were reported using AFM in a liquid environment.[257, 258] High-resolution visualization of fibrinogen was achieved with AFM in liquid environments as well as measurements of the adhesion forces of fibrinogen towards different surfaces.[259] Molecular-level resolution was achieved with visualization of the αC region of fibrinogen by Yermolenko et al.[260]

In this investigation, a compositionally patterned Si(111) surface of mercaptosilanes was designed to provide selective sites for the attachment of fibrinogen within a protein resistant matrix of PEG-silane. Previously, we introduced several particle lithography based protocols for patterning organosilanes using steps of vapor deposition, immersion or contact printing.[261, 262]

The surface selectivity of organosilane nanopatterns prepared with particle lithography approaches can be further applied to define the placement of other molecules and nanoparticles.[114, 177] Particle lithography offers advantages for high throughput patterning and enables control of the surface coverage, geometry and lateral dimensions of nanopatterns with relatively inexpensive reagents. However, when backfilling the patterns with a second organosilane, the self-reactive properties of hydroxyl terminated PEG-organosilanes were problematic. When using successive immersion steps in solutions of organosilanes the hydroxyl groups of PEG-silanes were found to cross-react and form mixed surface multilayers.

In this report, details will be disclosed for an innovative strategy of masking areas of a mercaptosilane film to protect small, discrete regions of the surface from cross reaction with PEG-silane. Images acquired with AFM disclose surface changes throughout steps of preparing organosilane patterns, binding fibrinogen and for studying the activity of the immobilized protein for binding anti-fibrinogen. The size of the fibrinogen nanopatterns achieved with particle lithography is on the order of 100 to 200 nanometers, enabling resolution of surface changes at the nanoscale. The simple steps of bench chemistry used for particle lithography protocols are accessible for most laboratories and are well-suited for studies of proteins using small quantities (microliters) of highly dilute protein solutions.

5.2 Materials and methods

5.2.1 Materials and reagents

Pieces of single-side polished Si(111) doped with boron (Ted Pella, Inc., Redding, Ca) were used as substrates. The silicon substrates were cleaned with sulfuric acid (ACS reagent 95%) and hydrogen peroxide (30%) purchased from Sigma-Aldrich. Silane reagents of 2-[methoxy(polyethyleneoxy)propyl] trichlorosilane (PEG-silane) and 3-mercaptopropyl-

trimethoxysilane (MPTMS) were purchased from Gelest (Morrisville, PA) and used without further purification. Anhydrous toluene was obtained from Sigma-Aldrich. A suspension of 500 nm silica mesoparticles was obtained from Fisher Scientific. Monodisperse silica powder (250 nm and 100 nm) was acquired from Fiber Optic Center, Inc. (New Bedford, MA) and prepared in ethanol (ACS grade, Pharmco-Aaper, TX). Deionized water used in experiments and to prepare phosphate buffered saline (PBS, pH 7.4) was obtained from a Direct-Q3 system (18 MΩ, Millipore, Bedford, MA). Bovine fibrinogen was used for surface studies (Sigma Aldrich). For antigen-antibody studies, human fibrinogen and polyclonal rabbit anti-human fibrinogen were acquired and used as received from Calbiochem, La Jolla, CA. Sulfosuccinimidyl-4-(N-maleimidomethyl) cyclohexane-1-carboxylate (sulfo-SMCC) was used as a crosslinking agent for attaching fibrinogen to MPTMS (Thermo Fisher Scientific Inc., Rockford, IL).

5.2.2 Particle lithography procedure

An overview of the steps for particle lithography with organosilanes is shown in Figure 5.1. Silicon substrates (5x5 mm^2) were rinsed with deionized water, dried with argon and placed in a 3:1 (v/v) solution of sulfuric acid and hydrogen peroxide (piranha solution) for cleaning. *The piranha solution should be handled with care, it is highly corrosive.* After 90 min, the substrates were removed from the cleaning solution, rinsed with deionized water and dried under a stream of argon. The substrates were placed on a platform within a sealed reaction vessel containing 400 µL of neat MPTMS. The vessel was heated in an oven at 70 C to generate a vapor of MPTMS (figure 5.1*a*). Over time, the vapor reacted with the silicon substrate to produce a thin film of MPTMS throughout the surface areas of Si(111). After 4 h of exposure to vapor, the samples were removed from the vessel, washed with ethanol, further rinsed by sonication in ethanol for 30 min and then dried under a stream of argon. A suspension of silica mesoparticles was

prepared by adding 0.1 g of dry, powdered mesospheres to 10 mL of ethanol followed by 30 min sonication. Solutions of silica mesoparticles were cleaned by washing four times using centrifugation with resuspension in deionized water. To prepare a surface mask, 10 µL of silica mesoparticles was deposited on the MPTMS/Si sample and dried at 4 C for 16 h. The samples were then treated with UV-ozone for 20 min to oxidize exposed areas between the particle masks (figure 5.1*b*). Molecules of MPTMS within the areas exposed to UV-ozone treatment were decomposed, forming silanol functional groups.[263] Immediately after UV-ozone treatment, the samples were immersed in a 1% (v/v) solution of PEG-silane in anhydrous toluene for 5 h. During the immersion step, the areas exposed to UV-ozone refilled with PEG-silane, whereas the areas underneath the silica spheres with MPTMS remained protected (figure 5.1*c*). Water was used to initially rinse the sample and quench the silanization reaction. Next, the samples were rinsed with ethanol with 30 min sonication to remove the silica mesospheres. A further rinsing step with sonication in water for 30 min ensured complete removal of the mesospheres and then the samples were dried under argon.

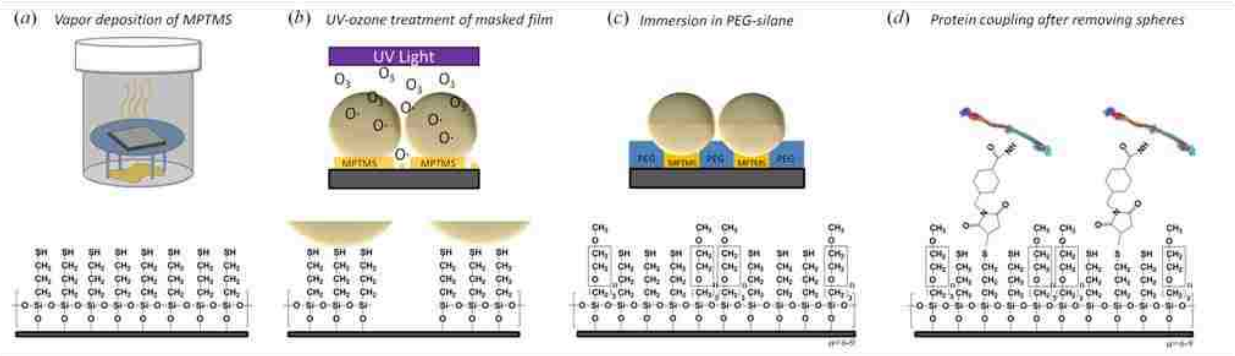

Figure 5.1 Steps for preparing protein nanostructures with particle lithography. (*a*) A surface film of MPTMS was prepared by vapor deposition on Si(111) substrates; (*b*) After coating the MPTMS surface with a mask of silica mesospheres, the samples were treated with UV ozone. (*c*) Samples were immersed in a PEG-silane solution to refill the exposed surface sites with a protein resistive matrix. The mask of silica mesospheres was removed by solvent rinsing. (*d*) Proteins were coupled to MPTMS sites after immersing samples in sulfo-SMCC.

5.2.3 Attachment of fibrinogen to nanopatterned surfaces

The sulfhydryl groups located within the nanopatterned pores of MPTMS were activated through sulfo-SMCC coupling.[264] The samples were submerged in a 1 mM solution of sulfo-SMCC prepared in PBS (pH 7.4) for 1 h. Next, the samples were rinsed with PBS to remove excess sulfo-SMCC. The samples were then immersed in a 0.5 mg/mL solution of fibrinogen in PBS for 50 min. Lysine residues of the protein structure attach covalently to the reactive NHS-ester located on the exposed region of sulfo-SMCC (Figure 5.1d). The samples were rinsed successively with PBS followed by detergent (0.1% solution Tween 20) to remove nonspecifically adsorbed protein.

5.2.4 Antigen-antibody binding studies

Phosphate buffered saline (PBS) was used to rinse the surface of fibrinogen nanopatterns. Next, the samples were immersed in a 0.25 mg/mL solution of anti-fibrinogen in PBS for 30 min. After removal from the antibody solution, samples were rinsed successively with PBS, 0.1% Tween 20 and deionized water. The samples were dried under a stream of argon and then characterized using tapping-mode AFM.

5.2.5 Atomic force microscopy

Scanning probe studies were done with either a model 5420 or 5500 instrument equipped with PicoView v1.8 software (Agilent Technologies, Tempe, AZ). Probes from Applied Nanostructures, (ACTA, resonant frequency 300 kHz, k = 37 N/m) were used for imaging in tapping-mode. Images were processed and analyzed using Gwyddion (version 2.15) which is freely available on the internet and supported by the Czech Metrology Institute.[265] The surface coverage of nanopatterned areas were evaluated using UTHSCA Image Tool software.[266] To

estimate surface coverage, the AFM frames were converted to black and white images by manually selecting a threshold value and counting pixels.

5.3 Results and Discussion

5.3.1 Nanopatterns of MPTMS within a resistive PEG-silane matrix

Images of the surface changes were captured with ambient AFM studies after key reaction steps of organosilane patterning, protein immobilization and antibody binding. Representative images of the MPTMS nanodots within a PEG-silane matrix are shown in Figure 5.2. Images of the clean substrate, MPTMS film and silica mesosphere samples are presented in Appendix D (Figure D1). The silica spheres were completely removed by rinsing steps, to disclose designed nanopatterns of organosilanes. The nanopores are shallower than the surrounding areas of PEG-silane and appear as dark spots (Figure 5.2a). There are 70 nanopores visible within the 5x5 μm^2 topograph, which scales to a surface density of ~10^8 nanopatterns/cm^2, corresponding to 5.1% surface coverage of MPTMS. The MPTMS nanopatterns are produced at the regions of contact that were directly underneath the silica mesospheres which were protected from UV-ozone treatment. The nanopores are spaced regularly at 500 nm intervals, as determined by the periodicity of the mesosphere masks. The diameters of the nanopatterns measure 160 ± 20 nm and reflect the geometry of the areas of close physical contact between the spheres and the Si(111) substrates. The corresponding phase image (Figure 5.2b) further reveals the differences in surface chemistry. The color contrast is reversed for the phase frame, with brighter spots shown for the nanopores terminated with sulfhydryl groups; whereas the surrounding matrix areas of PEG-silane are darker. The phase images result from mapping slight incremental changes in the oscillation of the AFM tip caused by damping of the motion when the tip interacts with the surface. Thus phase images are sensitive maps of

changes in film thickness and tip-surface adhesion. A magnified view of a single nanopore is shown in the AFM topography frame of Figure 5.2c. Within the 500×500 nm^2 frame, the clustered morphology of the surrounding PEG-silane matrix is apparent. The uneven morphology located at the bottom of the nanopore is attributable to the roughness for the underlying MPTMS film. The height of the nanopores measure 3.0 ± 0.3 nm above the matrix areas of PEG-silane (Figure 5.2d). Assuming the MPTMS film is a monolayer with a thickness of 0.7 nm, [267] then the multilayer thickness of the PEG-silane film is ~ 3.7 nm. This suggests that the surrounding film of PEG-silane likely forms a cross-linked bilayer.

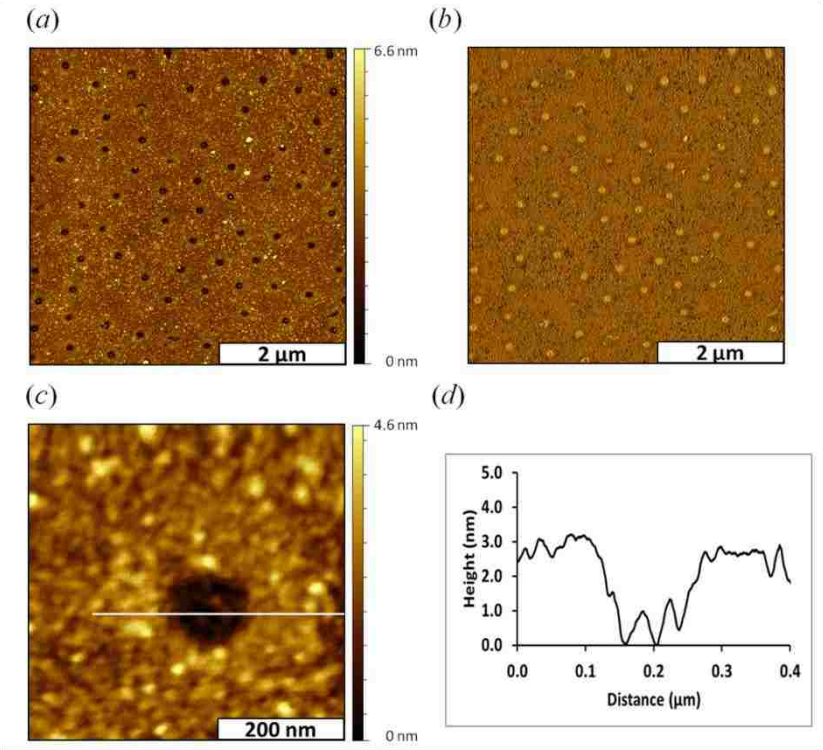

Figure 5.2 Views of MPTMS nanopores obtained with ambient tapping-mode AFM. (*a*) Topograph of the nanopores and (*b*) corresponding phase image. (*c*) Close-up topography view of a single nanopore; (*d*) height profile for the white line in *c*.

The hydroxyl functional groups of PEG-silane are reported to be suitable for designing protein resistant films.[268, 269] There are few surfaces that resist protein adsorption and

considerable research has addressed studies of the mechanisms of protein resistance or adhesion to surfaces.[270-273] Systematic studies have been done to evaluate the molecular characteristics of functionalized SAMs for resisting protein adsorption.[274, 275]

Immersion of PEG-silane films into solutions of organosilanes generated mixed layers and multilayer surface structures which were not spatially selective for patterning proteins (*data not shown)*. The rationale for using UV-ozone treatment to remove selected areas of an organosilane surface layer follows from our studies of the reactivity of PEG-silane with other organosilanes. When using multi-step protocols to generate organosilane nanopatterns, experiments with particle lithography showed that hydroxyl headgroups of PEG-silane surfaces react with other silanes during immersion steps. To prepare MPTMS nanopores, UV-ozone treatment through surface masks was found to provide selectivity in combination with steps of particle lithography and immersion. A strategy for selectively backfilling irradiated sites provides nanoscale control for producing discrete small regions of MPTMS which can then be used with further biochemical steps to isolate and define surface sites for binding protein.

Changing the diameter of the mesoparticles used as masks for surface fabrication provides a way to control the surface coverage and density of the nanopatterns.[116, 119] When using smaller diameters of silica mesoparticles, a greater surface density of nanopatterns can be generated. Further examples of AFM images of MPTMS nanopatterns prepared with different diameters of silica mesospheres are provided in Appendix D (Figure D2).

5.3.2 Spatially selective attachment of fibrinogen to surface sites with MPTMS

Morphology changes are readily apparent for the sample surface after fibrinogen patterning (Figure 5.3). The heights of the nanopatterns have increased, as shown for a representative 5×5 μm^2 topography frame (Figure 5.3a). For the most part, fibrinogen seems to

bind primarily at the sites with MPTMS and negligible adsorbates are located in areas between the taller protein clusters. The arrangement of nanopatterns indicates the sites of small clusters of protein, spaced at intervals of 500 nm. Further examples of fibrinogen nanopatterns with even smaller periodicities are shown in Appendix D (Figure D3). A zoom-in view of a single protein nanodot is presented in Figure 5.3b. The height measures 9 nm above the PEG-silane matrix at the tallest area in the center of the nanopattern (Figure 5.3c). Since the MPTMS nanopatterns were 3.0 nm shorter than the surrounding matrix film, after protein attachment the height increase measures an overall thickness of ~12 nm for the nanopattern.

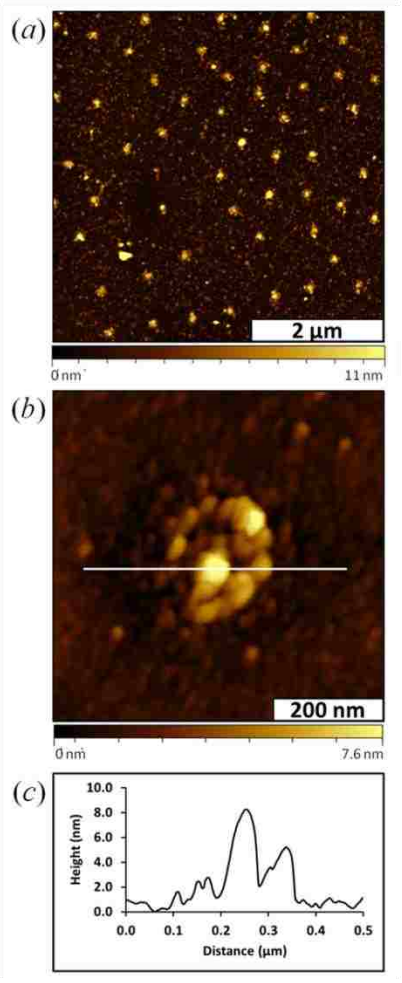

Figure 5.3 Surface changes after binding fibrinogen. (*a*) Fibrinogen attaches at the sites with MPTMS shown with an AFM topograph; (*b*) Magnified view of a single nanostructure with fibrinogen; (*c*) corresponding height profile.

A sulfo-SMCC linker (0.83 nm) was used to couple fibrinogen to the surface of MPTMS nanopatterns, fibrinogen attached selectively at the regions patterned with sulfhydryl moieties (Figure 5.3). When the chemically patterned samples were immersed in a sulfo-SMCC solution for 1 h, the maleimide groups of sulfo-SMCC react with thiol groups at the interface. This produces an activated surface pattern with an NHS-ester that was available for binding protein. When the activated sample was immersed in a solution of fibrinogen, exposed lysine groups of the protein reacted with the NHS-ester to link the protein to the surface. The PEG-silane matrix furnished a protein resistant background to surround and isolate discrete regions of bound protein.

After binding fibrinogen, the change in height of the protein nanopatterns ranged from 9 to 13 nm (average is 11.0 ± 1.1) when including the depth of 3.0 nm from the MPTMS pores. There are multiple exposed lysine residues on each fibrinogen molecule for attaching to the surface. Thus, the protein may attach to the surface with different orientations. Studies with high-resolution AFM images of fibrinogen have been previously reviewed.[254] Trinodular molecules of fibrinogen were reported to measure lengths ranging from 48 to 60 nm, and the width measured 8 to 28 nm. The values measured for the height of fibrinogen ranged from 1.2 to 4.1 nm. For the fibrinogen bound to MPTMS nanopatterns, the thickness of 11.0 ± 1.1 nm most likely corresponds to 3-5 layers of protein assuming a horizontal orientation. The multilayer assembly for fibrinogen has been previously documented.[276, 277] As fibrinogen adsorbs or covalently attaches to a surface, it spreads onto the surface and unfolds. It has been suggested that this unfolding exposes binding sites that initiate self-aggregation.[278]

The surface density and coverage of protein nanopatterns can be controlled at the nanoscale by selecting the diameter of mesospheres used for particle lithography masks.

Mesospheres with a smaller diameter generate a greater number density of smaller-sized nanopatterns; however the overall surface coverage of protein increases. Analysis of AFM images from experiments with different sizes of mesospheres are summarized in Table 5.1. Our studies show that the width of the patterns increased after protein attachment such that the proteins extend beyond the edges of the MPTMS nanodots. In the longest direction, fibrinogen was reported to measure 47 nm;[260] this corresponds to an orientation where the long direction is parallel to the sample surface. Measurements of the diameters of the nanopores before protein attachment suggest that 2 or 3 fibrinogen molecules can fit on a single nanopattern. Particle lithography using smaller spheres likewise generated nanopores with smaller diameters (Table 5.1). Eventually, if the diameter of the nanopatterns can be matched to the size of a single protein, selective patterning of individual proteins on the surface will be achievable.

Table 5.1 Surface coverage of MPTMS and fibrinogen as a function of mesosphere mask size.

silica diameter (nm)	surface coverage MPTMS (%)	surface coverage fibrinogen (%)	pore diameter (nm)
500	5.0	7.8	160±20
250	7.7	9.8	134±19
100	16	17	104±18

5.3.3 Antigen-antibody binding studies

The final biochemical step for the studies with surface nanopatterning was to evaluate the activity of the immobilized fibrinogen for binding IgG. Images were obtained after anti-fibrinogen was added to the sample *ex situ* (Figure 5.4). The heights of the patterns have increased, shown with topography views in Figure 5.4. The periodic arrangement of nanopatterns is preserved, shown in Figure 5.4a, however the nanopatterns are taller after binding anti-

fibrinogen. Most of the antibody binding is localized at the central areas of the nanopatterns. A close-up view of a single nanostructure is shown in Figure 5.4b. The surrounding areas of the matrix have also changed in appearance, indicating that there are adsorbates surrounding the nanopatterns. The nature of the adsorbates, which may be salts, contaminants or non-specifically bound protein or antibody cannot be determined with AFM. The heights of the nanostructures after IgG attachment measured 17 ± 4 nm (including the 3 nm value for original depth of the nanopore). This value indicates an overall increase of 6 nm which matches the approximate dimensions of a single layer of IgG with a side-on orientation.

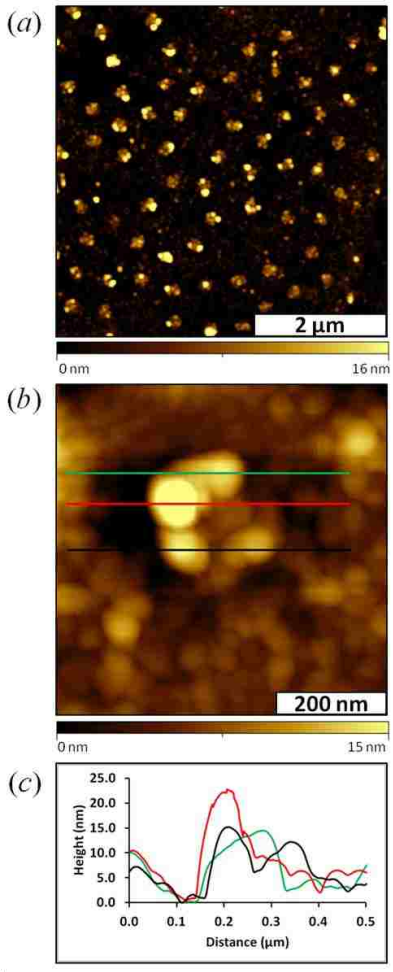

Figure 5.4 Changes of the nanostructures after binding antibody. (*a*) Topography image (5×5 μm^2) acquired in air; (*b*) Single nanostructure of fibrinogen-IgG; (*c*) height profiles after antibody binding.

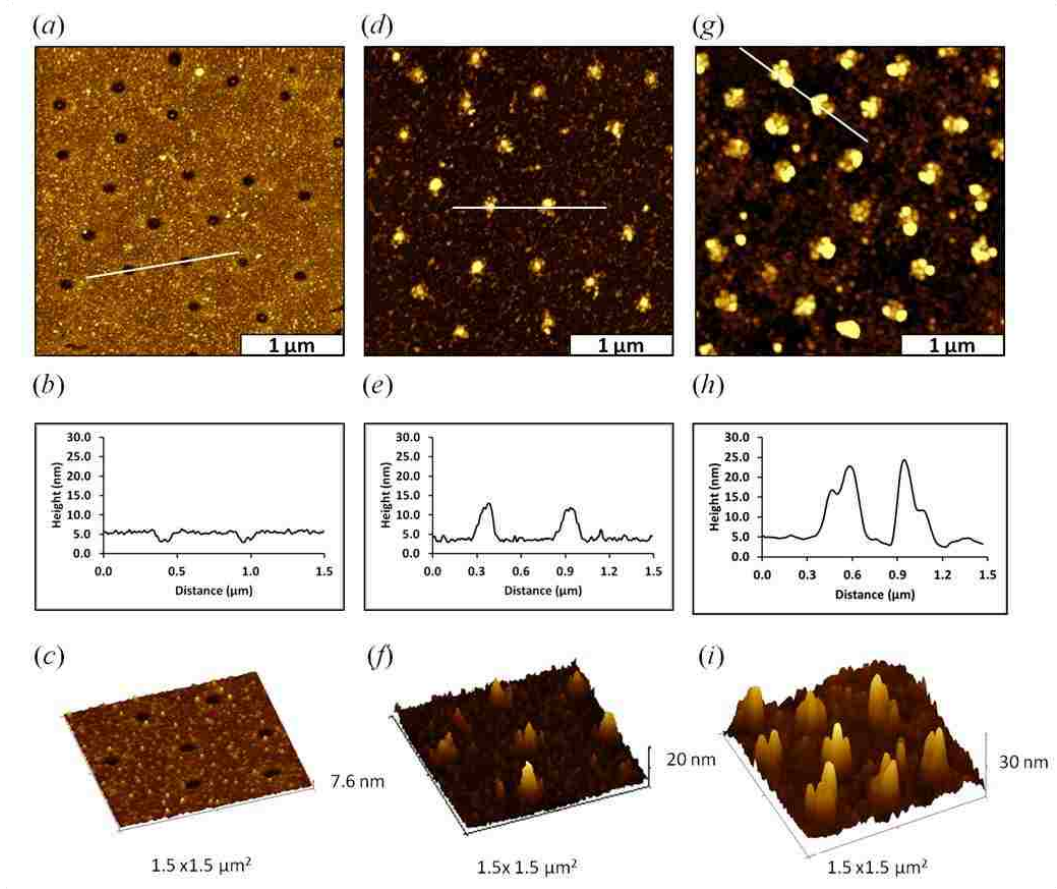

Figure 5.5 Step-by-step changes of the surface during the process of nanofabrication and protein binding. Nanopores of PEG-silane: (*a*) topography, (*b*) cursor profile and (*c*) 3D view. After coupling of fibrinogen to nanopores: (*d*) topography, (*e*) cursor profile and (*f*) 3D representation. After binding anti-fibrinogen to nanopatterns: (*g*) topography; (*h*) corresponding cursor profile and (*i*) 3D image.

To view the overall changes taking place on the designed surface at different points of the nanofabrication and protein binding processes, Figure 5.5 presents a side-by-side comparison of AFM images during key steps of the reactions. The *ex situ* experiments disclose only very local areas of the surface; however the frames are representative of multiple images acquired for different areas throughout the entire sample. The changes in height and lateral dimensions for snapshots at each step are shown in the top row of Figure 5.5. A quantitative comparison of the changes in dimension is shown with representative cursor profiles drawn across the topography frames in the middle row. From left-to-right, the nanopores change from being holes, to forming

isolated islands of fibrinogen, to taller protein-antibody clusters. At each step, the structures became both taller and slightly wider with the addition of fibrinogen and anti-fibrinogen molecules. Smaller regions measuring 1.5×1.5 μm^2 are compared with 3D views in the bottom row of Figure 5.5. The progressive growth in height and width of the nanostructures is apparent and surface selectivity for protein binding is mainly localized to the areas of MPTMS.

A significant advantage for developing particle lithography-based approaches for patterning organosilanes is that high throughput at the scale of millions to billions of nanopatterns can be achieved with only basic steps of the chemical self-assembly. Since organosilanes can be used with glass substrates, the procedures can be scaled to larger micron-scale dimensions for accomplishing protein-binding assays based on fluorescence detection. Future directions planned for AFM-based investigations with this surface protein sensor platform will be to study the interactions of small molecules or DNA with immobilized proteins and to develop more complex biochemical protocols for studies of protein bioactivity.

5.4 Conclusion

The reactivity of nanopatterns of organosilanes can be designed to spatially direct the immobilization of fibrinogen and IgG. Surface changes were monitored after steps of protein immobilization and antibody binding using *ex situ* AFM studies. Changes in the thickness of protein layers after immobilization were evaluated directly using height measurements with AFM, without the need for fluorescent or chemical labeling. Future work will investigate the size-dependent changes of nanopattern size for the effectiveness of protein immobilization, protein activity for binding antibodies *in situ*, as well as the changes in surface morphology within liquid media at different pH/ion concentrations.

CHAPTER 6: SURFACE-DIRECTED SYNTHESIS OF ERBIUM-DOPED YTTRIUM OXIDE NANOPARTICLES USING ORGANOSILANE ZEPTOLITER CONTAINERS

6.1 Introduction

The optical, catalytic, and magnetic properties of bulk materials of rare earth oxides (REO) have been applied commercially in optical displays, alternatives for catalytic converters, or as permanent magnets in disk drives.[279-283] The current challenge for synthesizing nanomaterials with rare earth elements requires synthetic capabilities to achieve high crystallinity and monodispersity of the products. Heating at temperatures in the range of 900-1400 C are necessary to produce crystalline REO nanomaterials.[284] The properties of REO materials greatly depend on achieving a high degree of crystallization for samples.[285] Wet chemistry approaches that are commonly used for preparing metal nanoparticles are not amenable for synthesis with such high temperatures. Methods such as post-annealing to obtain crystallinity for nanomaterials tend to cause sintering of the nanoparticles, and capping agents used to control the shape and size may interfere with the desired catalytic or optical properties of the nanoparticles.[286, 287] To address the limitations of solution-based methods, we have developed a surface-directed procedure for high temperature synthesis, using nanopores within organic films as reaction containers. The matrix film provides a surface platform to spatially segregate small volumes of reagents and is efficiently removed by calcination during heating steps.

At the microscale, the strategy of using a surface template to mold and form nanomaterials has previously been investigated for precipitation of salts and protein solutions. Surface arrangements of microcrystals of (KBr, KH_2PO_4, NaCl, KNO_3, $NaNO_3$, hydroquinone and glycine) were prepared within micropatterned photoresists by Thalladi et al.[288] Micropatterned wells prepared by photolithography were functionalized with thiol chemistry for the crystallization of proteins by Wang et al.[289] Crystals of calcite were grown within

micropatterned self-assembled monolayers (SAMs) prepared by microcontact printing by Aizenburg et al.[290] Using templates prepared with microcontact printing of SAMs, magnetic nanoparticles (cobalt, nickel, ferrites) ranging from 70-460 nm in size were prepared on silicon substrates from nitrate salt deposits after heating to 600 C, demonstrated by Zhong et al.[291] Defined arrangements of magnetic colloids were prepared at the micron scale on glass surfaces by Lyles, et al. using a process of polymer-on-polymer stamping with microcontact printing.[292] Arrays of gold nanoparticles were fabricated on ITO substrates using a method which combined nanoimprint lithography with electrochemical deposition by Ma et al. The crystals produced with methods of photolithography and microcontact printing have the additional advantage of being prepared with well-defined arrangements on surfaces.

Nanoscale patterning of SAMs can be accomplished with particle lithography without using manufactured molds or masks prepared with electron beams to achieve small features.[75, 119, 176] Particle lithography can be used to prepare surface molds of SAMs to define sites for the deposition of nanomaterials and to provide spatial separation during subsequent steps of drying or heating. The photoluminescent properties of $NaYF_4$:Yb,Er rare earth nanoparticles prepared using particle lithography to generate periodically arranged rings of nanoparticles was investigated by Mullen et al.[293] Nanorings of *n*-octadecyltrichlorosilane (OTS) were used as sites to nucleate nanoparticles of small organic molecules such as *n*-docosane, aspirin, and clarithromycin prepared using particle lithography by Wang et al.[294]

Erbium-doped yttrium oxide nanoparticles have interesting luminescent properties such as intense cathodoluminescence and photoluminescence.[285, 295] Nanomaterials of yttrium oxide doped with rare earth elements have been prepared by flame spray pyrolysis (Eu:Y_2O_3),[285] thermal decomposition of a polymeric resin,[296] atomic layer deposition,[297] gas-phase

condensation,[298] flux,[299] combustion,[300-302] solvothermal[303] and hydrothermal methods,[304-310] alkalide reduction,[311] solution-based sol-gel processes,[312] emulsion techniques,[313-315] precipitation,[316-318] and electrochemical[319] methods. Preparation of Y_2O_3:Eu^{3+} nanowires using a template of anodized aluminum oxide that was heated to 800 C was reported by Zhang et al.[320] Ordered arrays of Y_2O_3:Eu^{3+} nanotubes were prepared in anodic alumina membranes by a method of electronic field-assisted deposition.[321]

In this report, nanopores within organosilane self-assembled monolayers (SAMs) that were prepared using particle lithography were used as containers for the surface-directed synthesis of erbium-doped yttrium oxide nanoparticles at high temperatures. The sacrificial surface mold of octadecyltrichlorosilane (OTS) was used to define the deposition of precipitates of rare earth salts from solution as a means to control the size, dispersity and surface density. Successive heating steps were used to crystallize the rare earth oxide (REO) deposits as well as to remove the OTS resist. Our goal was to produce spatially separated nanoparticles of erbium-doped yttrium oxide with a periodicity defined by surface masks of silica mesospheres. Micropatterns that were prepared by capillary filling of PDMS molds provided an approach to optimize the heating protocol for converting yttrium salt precipitates into yttrium oxide. The analysis of sample morphologies, surface density and periodicity was accomplished with atomic force microscopy (AFM).

6.2 Experimental section

6.2.1 Preparation of yttrium precursor solution

A rare earth salt solution comprised of yttrium trichloroacetate was prepared according to a previously published procedure.[322] Yttria powder (15 mmol) was dissolved in concentrated nitric acid (100 mL) by heating to 80 C. After the solid had dissolved the salt solution was

cooled to room temperature. Yttrium hydroxide was then precipitated from solution by adding NH_4OH until basic. The precipitate was isolated by vacuum filtration, washed several times with cold deionized water, and dried with air. A solution of yttrium trichloroacetic acid was prepared by dissolving the hydroxide precipitate in a 25% trichloroacetic acid solution. Just enough of the acid was added to dissolve the precipitate to make a saturated solution of the salt. A second solution was prepared at half of the concentration of the original solution to study the effect of concentration on the size of the nanoparticles.

6.2.2 Micropatterns prepared by capillary filling of PDMS molds

Micron scale patterns of Y_2O_3 were fabricated to provide surface structures for XRD characterizations. Microline patterns of yttrium oxide were prepared from the saturated yttrium salt solution to optimize the heating parameters for yttria synthesis. The method of capillary filling of PDMS molds has been previously demonstrated with solutions of proteins.[226, 227, 323] The capillary filling of microchannels of PDMS molds is also suitable for directing the placement of salt solutions on flat surfaces. Detailed steps for the procedure of capillary filling of PDMS molds are provided in Appendix E, Figure E1.

6.2.3 Nanoparticles of Er-doped Y_2O_3

The procedure for preparing nanoparticles of erbium-doped yttria on a silicon surface is outlined in Figure 6.1. Octadecyltrichlorosilane (OTS) molecules were deposited on a silicon substrate using immersion particle lithography to form nanopores (Figure 6.1a), as previously reported.[176] The nanoscopic reaction vessels were then immersed into a precursor solution of yttrium trichloroacetate doped with erbium cations (3%) for up to 3 h. The sample was removed slowly from the solution at a 90^o angle to selectively fill the nanopores.[324] Upon drying, a tiny precipitate formed within each zeptoliter reaction vessel (Figure 6.1b). The sample was then

heated at 150 C to decompose the acetate to form $Y_2(CO_3)_3$ doped with 3% erbium. The temperature was then increased to 800 C for 8 h for removal of CO_2 to produce nanosized rare earth oxides (Figure 6.1c). The same heating protocol developed for synthesis of micropatterns was used for preparing nanoparticles.

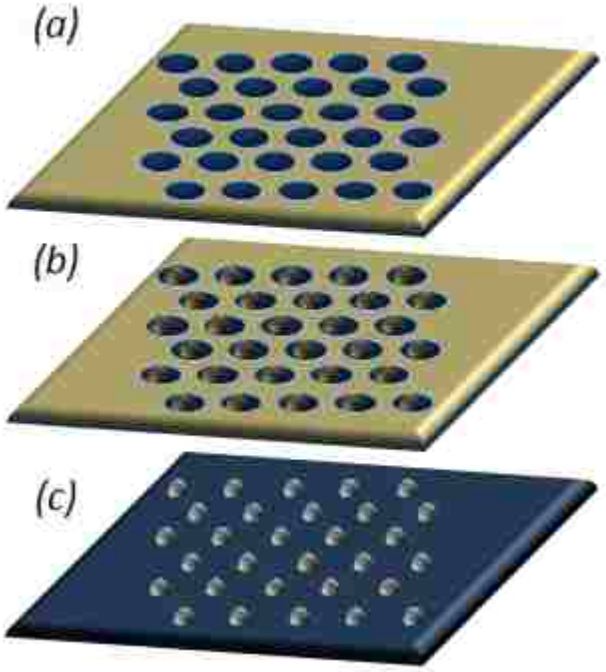

Figure 6.1 Basic steps to prepare a surface array of REO nanoparticles. (*a*) A sacrificial template of organosilane nanopores was prepared by particle lithography. (*b*) The nanopores were filled with a precursor solution of yttrium and erbium salts and dried. (*c*) The organosilane template was removed by heating to produce erbium-doped yttria nanoparticles.

6.3 Results and discussion

6.3.1 Microline patterns of yttrium oxide

The capillary filling approach for surface patterning was used successfully to prepare microparticles with an aligned arrangement as shown in Figure 6.2. The microstructures formed in line patterns were used to evaluate and optimize synthetic conditions (temperature, duration of

heating and atmosphere requirements). The rectangular area of parallel lines indicates the region where the PDMS mold was placed, shown in the scanning electron micrographs in Figure 6.2. The overall area of Si(111) that was covered by the PDMS stamp is shown in Figure 6.2a. The dark square in the center of the image is the area where the PDMS mold was placed on top of the silicon wafer, and the buildup of material on either side of the square indicates where the drops of liquid were placed on the substrate for capillary filling. When a drop of the liquid precursor

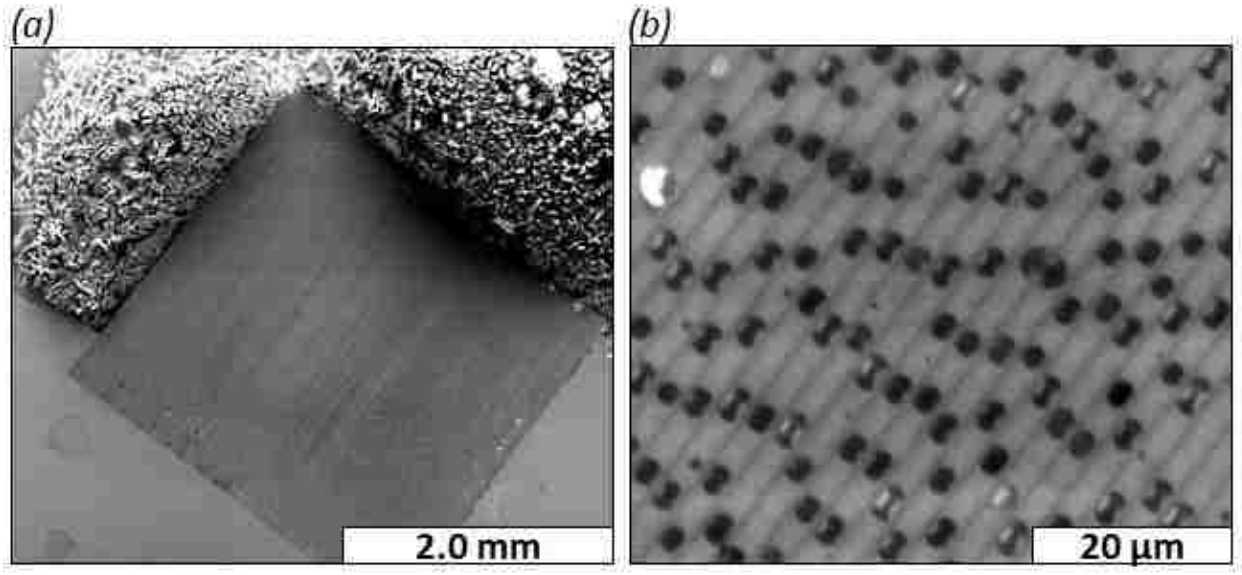

Figure 6.2 Microline surface structures of yttrium oxide prepared using capillary filling of PDMS molds shown with electron micrographs after calcination. **(***a*) Microlines of yttrium oxide produced after heating. (*b*) Close-up view of the microparticles formed inside the PDMS mold.

solution was place at the edge of the stamp, capillary forces drew the rare earth salt solution into the microchannels. As the sample dried, the salts formed line patterns of precipitates inside the channels, the remainder of the solution outside the PDMS stamp precipitated at the edge. After drying, the stamp was removed and the sample was heated to 800 C to convert the yttrium salt to yttrium oxide. Microparticles that were produced within the channels after heating are shown in Figure 6.2b. The elongated shape of the microparticles is produced by the edges of the PDMS channels. Some of the particles reveal a coalescence of two particles within the microchannels to

produce larger microparticles. Additional views of the microparticles acquired with AFM are shown in Figure E2 of Appendix E.

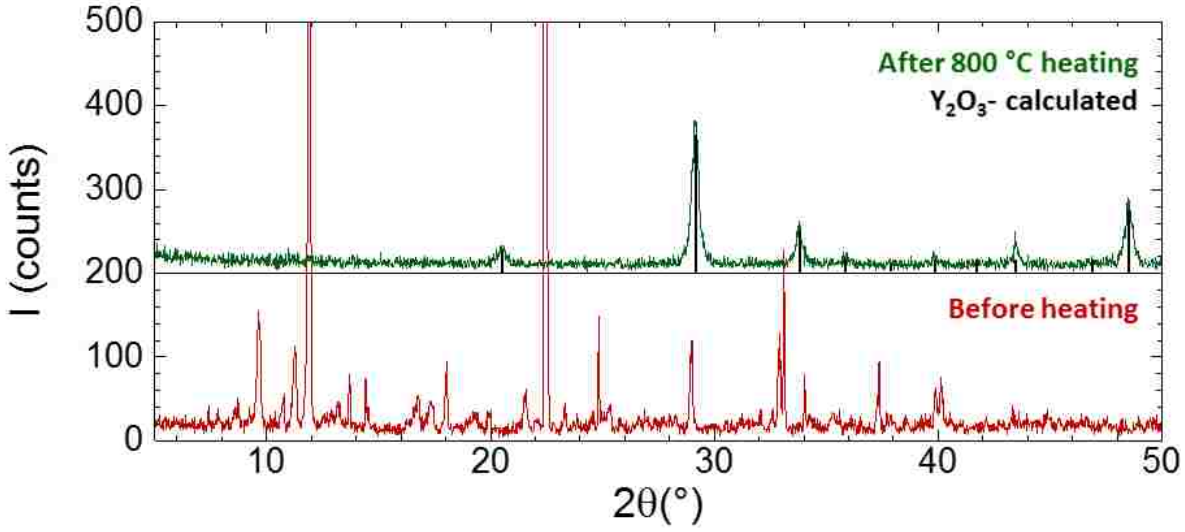

Figure 6.3 Yttrium oxide was formed after heating the sample to 800 C as demonstrated by the XRD results (green spectrum).

There are several advantages for the strategy of microfluidic filling of PDMS molds. Small volumes (less than 10 microliters) of dilute reagent solutions can be used to pattern samples (1×1 cm^2). Also, the PDMS molds can be washed and recycled for preparing replicate samples. The simple steps for micropatterning require little time for preparation, so that multiple samples can be prepared for tuning heating parameters. Changes of the temperature, ramping steps, duration, and cooling for heating the precursor samples will alter the crystallization process and influence the shape (primary face growth), crystallinity and orientation. The heating step also provides a means to remove impurities. These factors become more significant as the dimensions are reduced to progressively smaller dimensions at the scale of nanometers.

The heating profile to form yttrium oxide was optimized and investigated using powder X-ray diffraction for the microline structures. The XRD pattern upon heat treatment is shown in

Figure 6.3. Upon heat treating of the salts at 800 C, highly crystalline particles of Y_2O_3 are formed (green pattern in Figure 6.3).

6.3.2 Zeptoliter reaction vessels

For our approach based on particle lithography, a surface mask of silica mesospheres was used to define the surface coverage of organosilane resists. Monodisperse spherical particles self-assemble on flat surfaces to form periodic structures with designed dimensions and interparticle spacing, which provide a surface mask to define the sites for depositing organosilanes. With particle lithography, billions of nanostructures can be prepared on surfaces with relatively few defects and high reproducibility using basic steps of bench chemistry (mixing, centrifuging, heating and drying). Silica mesoparticles with a diameter of 500 nm were used to prepare the organosilane nanopores shown in Figure 6.4. Measurements with AFM reveal that the spacing between the nanopores measures 505 ± 35 nm, which closely matches the diameter of the silica mesoparticles used as surface masks. The depth of the nanopores measured 1.4 ± 0.1 nm. The long range order and periodicity of the nanopores formed on a silicon surface is evident in a representative topography view in Figure 6.4a. A map of the differences in chemistry between the methyl-terminated OTS film and areas exposed on the silicon substrate is shown with the simultaneously acquired lateral force image of Figure 6.4b. The diameter of the exposed sites of the substrate measured 90 ± 12 nm (n=75), based on measurements from the lateral force frames. At the nanoscale, there are imperfections in the shapes of the nanopores (Figure 6.4b). A close-up view of the shapes and sizes of the nanopores is presented in Figure 6.4c. Details for a single nanopore are shown in Figure 6.4d (200×200 nm^2). Each nanopore is used as a reaction vessel to synthesize individual nanoparticles. Based on size measurements with AFM, the volume of a nanopore measures 10^{-21} L.

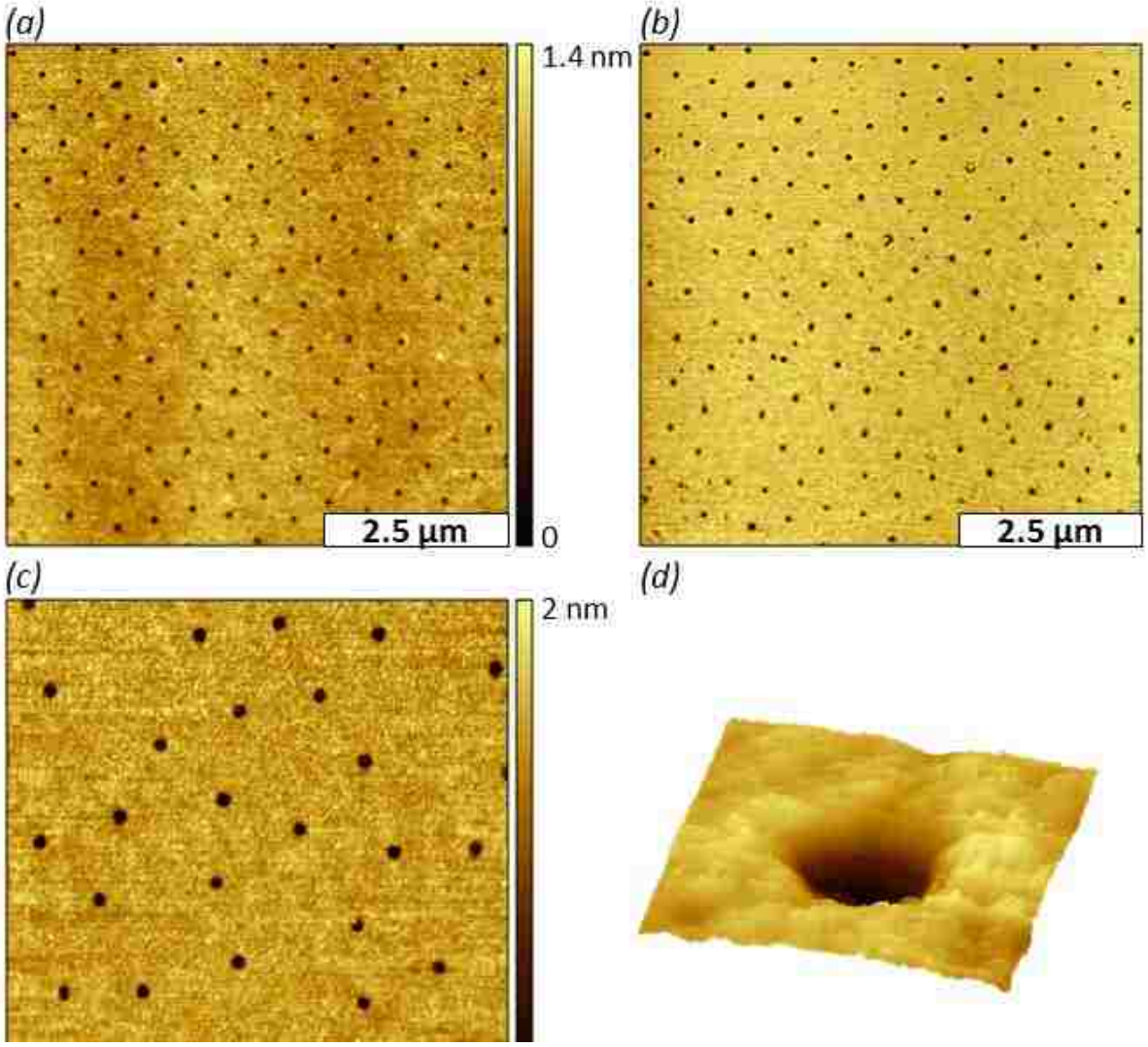

Figure 6.4 Nanopores within an OTS film produced with immersion particle lithography on Si(111). (*a*) Contact-mode topograph acquired in air; (*b*) concurrently acquired lateral force frame for *a*. (*c*) zoom-in view; (*d*) A single nanopore within a 200×200 nm^2 topography frame.

The arrangement and spacing between nanoparticles is determined by the diameter of the silica particles used to fabricate the mask. The surface density of the patterned nanopores can be changed by choosing the diameter of the mesosphere mask. The height of the nanopores is determined by the thickness of the OTS film, which has an expected height of 2.6 nm for a densely pack film.[98, 325] The nature of the substrate, solvent, concentration, temperature and immersion parameters must be optimized to achieve thicker films of OTS.[326] Imperfections at the

nanoscale influence the volume of the nanopore reaction vessels. The size, geometry and dispersity of the synthesized yttria nanoparticles will accordingly be influenced by the flaws in the shapes of the nanopores.

In the next step, the OTS nanopores were filled with the solution of precursor salt. The methyl-terminated film of OTS provided a resist to prevent non-specific adsorption in areas surrounding the nanopores. After the sample was dried, precipitates formed inside the nanopores (Figure 6.5). A small bright dot can be detected within each nanopore surrounded by a protective matrix film of OTS. The surface of OTS surrounding the deposits is slightly rougher, indicating that small residues of the precursor salts persist on the matrix. Nanocrystals are readily identified within the nanopores from the representative height profiles in Figure 6.5b. A small hill was formed in the center of each nanopore where the dried salt residues formed a deposit. A single reaction vessel filled with a precipitate of yttria trichloroacetate is shown in Figure 6.5c. The edges of the OTS nanopores define a clear boundary surrounding the deposited salt. The height of the nanodeposits within the nanopores measured 1.4 ± 0.4 nm, however the baselines at the edges of the nanostructures that were used for AFM cursor measurements likely did not reach the substrate. The areas surrounding the deposits may be partially filled with salts.

Within the representative AFM views of Figure 6.5, the OTS film was an effective resist for preventing attachment of the salts in areas surrounding the nanopores. The nanopores with OTS were filled with the salt solution and the periodic arrangement enables isolation to prevent aggregation when the sample is heated at high temperature. A similarly prepared sample was made using an organosilane terminated with polyethylene glycol groups. The PEG-silane film was not an effective resist for depositing precursor salts; the sample showed deposits located on areas throughout the sample.

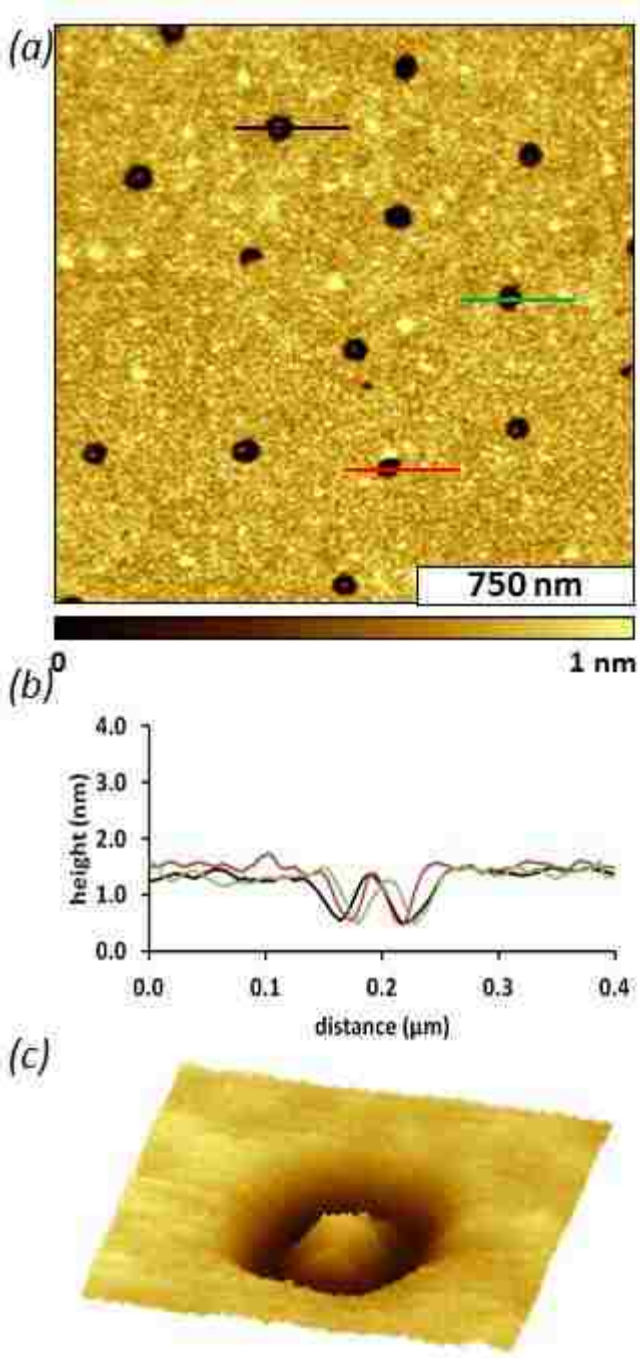

Figure 6.5 Zeptoliter vessels that were filled with rare earth precursor solution and dried. (*a*) Contact-mode topograph acquired in air; (*b*) height profile for the cursor lines in ***a***. (*c*) Magnified view of a single salt deposit (200×200 nm^2).

The sample of dried salt deposits shown in Figure 6.5 was heated to 800 C to produce an array of well-defined nanoparticles on Si(111). During the heating steps, the salt mixture is

restructured into nanocrystals of erbium-doped yttria (Figure 6.6). At high temperatures, the organic film of OTS was removed by calcination. The spacing between the nanoparticles measured 490 ± 37 nm, which corresponds to the diameter of the silica mesospheres used as a surface mask. The example of Figure 6.6 is representative of the high-throughput capabilities of particle lithography for patterning and arranging nanomaterials. Within the 7×7 μm^2 view there are ~ 140 nanoparticles, which scales to a surface density of 10^8 nanoparticles per cm^2. There appears to be small residues in a few areas between the nanoparticles, which most likely are residual salts that attached to OTS. The corresponding FFT of the AFM topography image is presented in the inset of Figure 6.6a, and reflects the periodicity of the sample. Height measurements of four nanoparticles are shown in Figure 6.6b. The nanoparticles range in height from 1 to 4 nm, with the average height measuring 3.8 ± 1.1 nm (n = 66). A single nanoparticle is shown in Figure 6.6c, evidencing clean removal of the OTS film. To test the effect of increased soaking time, another sample was prepared in which the OTS nanopores were immersed for 3 h in the saturated solution (Appendix E, Figure E3). After heating, the height of nanoparticles prepared with longer immersion measured 3.1 ± 0.9 nm (n = 86). Since there was no apparent increase in the size of nanoparticles, we concluded that 1 h immersion was sufficient for filling the nanopores.

The heating process provides a means to obtain the desired product and remove organic contaminants. During heating, the yttrium salt deposited within the nanopores was converted to yttrium oxide according to the XRD characterizations of microstructures prepared under identical heating conditions (Figure 6.2). When samples are heated to high temperatures, there is a possibility of sintering and aggregation of the deposits. The OTS film prevented aggregation of

the nanoparticles during the heating step and was removed completely by calcination at high temperatures. An OTS SAM has been reported to degrade at temperatures starting at 200 C and

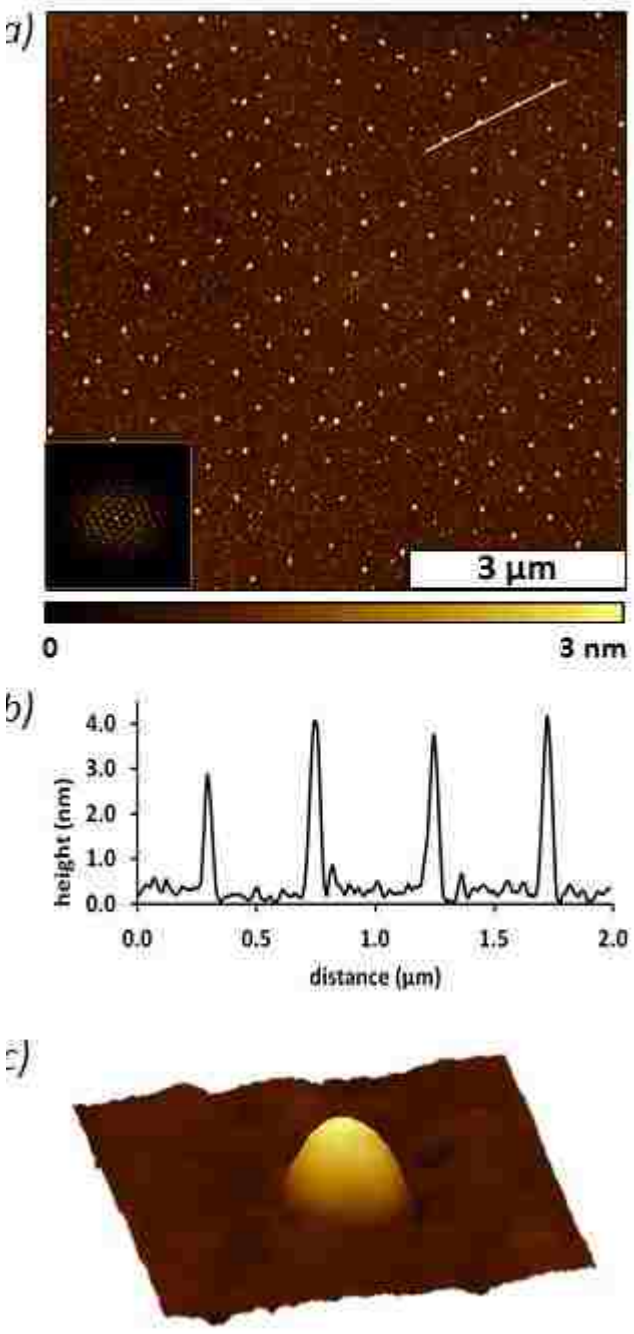

Figure 6.6 Surface arrangement of erbium-doped Y_2O_3 nanoparticles produced by heating. (*a*) Topography image acquired with tapping-mode AFM in air. The inset is the corresponding FFT. (*b*) Height profile for the white line in *a*. (*c*) Magnified topography view (200×200 nm^2) of an individual nanoparticle.

is no longer evident at temperatures of ~480 C according to thermogravimetric analysis.[327] The nature of the substrate is an important consideration for surface-directed synthesis, polished silicon wafers were used in this example. Organosilane SAMs provide flexibility for using substrates such as glass, indium tin oxide, quartz or silicon wafers, which can sustain synthetic steps at high temperatures.

The effect of the salt concentrations in the rare earth solution was tested to evaluate changes in nanoparticle size using a 50% reduction in concentration (Appendix E, Figure E3). After soaking for 1 h at 0.05 *m* concentration, we were unable to locate nanoparticles on the silicon substrate. However, nanoparticles were produced when the immersion time was increased to 3 h. The average height of the nanoparticles produced with lower salt concentration measured 0.5 ± 0.1 nm (n=27). At reduced concentration, the sizes of the nanoparticles were much smaller than those prepared from the saturated solution, using the same platform and dimensions of OTS nanopores as reaction vessels. We are currently investigating the potential of other resist films to use for high temperature synthesis of REO nanoparticles. We anticipate that surface designs with deeper pores will produce larger nanoparticles.

The proximity of neighboring nanoparticles can influence surface properties according to the distance or spacing between adjacent materials. Patterning inorganic materials by surface-templated reactions on small regions of a surface is not a conventional approach for inorganic synthesis. Factors such as dilution, contamination and reproducibility become increasingly significant as the dimensions are reduced. As the spacing between reaction vessels becomes smaller it is possible that aggregation could occur. Future directions for surface-directed synthesis of REO nanomaterials will evaluate if there are spatial limits for the spacing between nanopores. The surface-directed strategy can be extended to other REO and oxide nanoparticles

which require processing at high temperatures to effect crystallization. Designed surface arrangements with periodic spacing will facilitate measurements with individual, discrete crystals with defined surface density and arrangements. In future studies, the catalytic, magnetic, and photophysical properties of the arrays of nanoparticles will be examined as a function of nanoparticle size using scanning probe microscopies and surface spectroscopies.

6.4 Conclusions

We have developed approaches for surface-directed synthesis to prepare microstructures and nanostructures of REO materials. Conventional wet chemistry approaches are not suitable for preparing nanoparticles of rare earth oxides because relatively high temperatures are required that exceed the typical range of boiling solvents. Microstructures were used to evaluate and optimize synthetic conditions for advancing to smaller nanostructures, (e.g. temperature, duration of heating and atmosphere requirements). With particle lithography, nanopores within an organosilane matrix film were generated from a mask of monodisperse silica beads on Si(111). The nanopores were used as zeptoliter-sized reaction vessels to define the sites for surface-directed synthesis. The nanostructured film of organosilanes provided a sacrificial template, which is destroyed when surfaces are heated to high temperatures. However, the arrangement of inorganic deposits persists after heating, and becomes restructured into crystalline nanomaterials. Small volumes of dilute solutions were used to synthesize nanoparticles over areas spanning several cm. Since the approach is based on surface masks of mesospheres, the erbium-doped yttria nanoparticles were synthesized to yield well-defined arrangements conforming to the periodic packing of silica beads.

CHAPTER 7: CONCLUSIONS AND FUTURE PROSPECTUS

Chemically patterned surfaces were used to generate nanoscale surface patterns of organic and inorganic nanomaterials. Nanoscale arrays prepared through inexpensive, high-throughput fabrication methods are necessary for the future of nanoscale devices and sensors. The chemically patterned surfaces were fabricated using a combination of molecular self-assembly and particle lithography. The surface platforms are potentially useful for applications such as biosensors, platforms for in situ investigations, surface supported catalysts, optical filters, and light emitting arrays. The nanoscale patterned surfaces can be tailored to attach a wide variety of nanoscale materials by simply changing the designed surface chemistry. Investigations of the properties of single nanomaterials is possible using AFM in conjunction with the nanoscale arrays.

Nanopores of organosilane SAMs were used as containers to manufacture nanoparticles in a surface directed approach for solid state synthesis. The synthesis took place within confined areas of nanoscopic reaction vessels comprised of organosilanes. Patterns of erbium-doped Y_2O_3 were prepared. In future studies the synthetic method will be extended to fabricate other classes of rare earth nanomaterials with elements such as Gd and Ce. The catalytic, magnetic, and photophysical properties of the arrays of nanoparticles will be examined using scanning probe microscopies and laser spectroscopies.

Chemically functionalized surfaces of well-defined nanoscale dimensions were used as a spatially selective surface template to direct the binding of fibrinogen. The nanopatterns of fibrinogen were tested for the ability to bind antibodies. Measurements with AFM provide a framework for *in situ* studies of biomolecular reactions. The nanoscale platforms enable control of the surface density of protein, and are suitable for applications as biological sensing surfaces.

This strategy of arranging and controlling the orientation of proteins at the nanoscale can improve the selectivity and sensitivity of surface-based protein assays.

Magnetic sample modulation AFM provides capabilities for imaging magnetic nanomaterials. Nanoparticles as small as 0.8 nm have been detected with MSM-AFM. Surface arrays of nanoparticles were used as test platforms to develop dynamic protocols with MSM-AFM. Protocols were developed to evaluate how frequency and magnetic field strength of the applied magnetic field affect the response of the magnetic nanoparticles. The high sensitivity of MSM-AFM for mapping the distribution and locations of magnetic and superparamagnetic nanoparticles should provide a detection mechanism for ultrasensitive assays which use magnetic nanoparticle bioconjugates.

REFERENCES

1. Binnig, G.; Rohrer, H.; Gerber, C.; Weibel, E. Tunneling through a controllable vacuum gap. *Appl. Phys. Lett.* **1982,** *40*, 178.

2. Hansma, P. K.; Elings, V. B.; Marti, O.; Bracker, C. E. Scanning tunneling microscopy and atomic force microscopy - application to biology and technology. *Science* **1988,** *242*, 209.

3. Horber, J. K. H.; Miles, M. J. Scanning probe evolution in biology. *Science* **2003,** *302*, 1002.

4. Nilius, N. Properties of oxide thin films and their adsorption behavior studied by scanning tunneling microscopy and conductance spectroscopy. *Surf. Sci. Rep.* **2009,** *64*, 595.

5. Loos, J. The art of SPM: Scanning probe microscopy in materials science. *Adv. Mater.* **2005,** *17*, 1821.

6. Samori, P. Scanning probe microscopies beyond imaging. *J. Mater. Chem.* **2004,** *14*, 1353.

7. Samori, P.; Rabe, J. P. Scanning probe microscopy explorations on conjugated (macro)molecular architectures for molecular electronics. *J. Phys.-Condens. Mat.* **2002,** *14*, 9955.

8. Englade-Franklin, L. E.; Serem, W. K.; Daniels, S. L.; Garno, J. C. Dynamic magnetic characterizations at the nanoscale: A new mode for AFM imagaing with magnetic sample modulation (MSM-AFM). In *Atmoic Force Microscopy (AFM): Principles, Modes of Operation and Limitations*, Yang, H., Ed. Nova Science Publishers, Inc.: New York, 2014; pp 81.

9. Englade-Franklin, L. E.; Saner, C. K.; Garno, J. C. Spatially selective surface platforms for binding fibrinogen prepared by particle lithography with organosilanes. *Interface Focus* **2013,** *3*.

10. Dunn, R. C. Near-field scanning optical microscopy. *Chem. Rev.* **1999,** *99*, 2891.

11. Eaton, P.; West, P. *Atomic Force Microscopy*. Oxford University Press: New York, 2010.

12. Gewirth, A. A.; Niece, B. K. Electrochemical applications of in situ scanning probe microscopy. *Chem. Rev.* **1997,** *97*, 1129.

13. Hamers, R. J. Scanned probe microscopies in chemistry. *J. Phys. Chem.* **1996,** *100*, 13103.

14. Tseng, A. A.; Notargiacomo, A.; Chen, T. P. Nanofabrication by scanning probe microscope lithography: A review. *J. Vac. Sci. Technol. B* **2005,** *23*, 877.

15. Binnig, G.; Quate, C. F.; Gerber, C. Atomic force microscope. *Phys. Rev. Lett.* **1986,** *56*, 930.

16. Binnig, G.; Rohrer, H.; Gerber, C.; Weibel, E. 7X7 reconstruction on Si(111) resolved in real space. *Phys. Rev. Lett.* **1983,** *50*, 120.

17. Tochihara, H.; Shirasawa, T.; Suzuki, T.; Miyamachi, T.; Kajiwara, T.; Yagyu, K.; Yoshizawa, S.; Takahashi, T.; Tanaka, S.; Komori, F. Scanning tunneling microscopic and spectroscopic studies on a crystalline silica monolayer epitaxially formed on hexagonal SiC(000(1)over-bar) surfaces. *Appl. Phys. Lett.* **2014,** *104*.

18. Skomski, D.; Abb, S.; Tait, S. L. Robust surface nano-architecture by alkali-carboxylate ionic bonding. *J. Am. Chem. Soc.* **2012,** *134*, 14165.

19. Besenbacher, F.; Thostrup, P.; Salmeron, M. The structure and reactivity of surfaces revealed by scanning tunneling microscopy. *MRS Bulletin* **2012,** *37*, 677.

20. Binnig, G.; Rohrer, H. Scanning tunneling microscopy. *Surf. Sci.* **1983,** *126*, 236.

21. Binnig, G.; Gerber, C.; Stoll, E.; Albrecht, T. R.; Quate, C. F. Atomic resolution with atomic force microscope. *Europhys. Lett.* **1987,** *3*, 1281.

22. Meyer, G.; Amer, N. M. Novel optical approach to atomic force microscopy. *Appl. Phys. Lett.* **1988,** *53*, 1045.

23. Alexander, S.; Hellemans, L.; Marti, O.; Schneir, J.; Elings, V.; Hansma, P. K.; Longmire, M.; Gurley, J. An atomic-resolution atomic-force microscope implemented using an optical-lever. *J. Appl. Phys.* **1989,** *65*, 164.

24. Albrecht, T. R.; Akamine, S.; Carver, T. E.; Quate, C. F. Microfabrication of cantilever styli for the atomic force microscope. *J. Vac. Sci. Technol. A* **1990,** *8*, 3386.

25. Anderson, A. S.; Dattelbaum, A. M.; Montano, G. A.; Price, D. N.; Schmidt, J. G.; Martinez, J. S.; Grace, W. K.; Grace, K. M.; Swanson, B. I. Functional PEG-modified thin films for biological detection. *Langmuir* **2008,** *24*, 2240.

26. Xu, S.; Cruchon-Dupeyrat, S. J. N.; Garno, J. C.; Liu, G. Y.; Jennings, G. K.; Yong, T. H.; Laibinis, P. E. In situ studies of thiol self-assembly on gold from solution using atomic force microscopy. *J. Chem. Phys.* **1998,** *108*, 5002.

27. Galdi, N.; Buonerba, A.; Oliva, P.; Oliva, L. Nanostructured ethylene-styrene copolymers. *Polym. Chem.* **2014,** *5*, 3045.

28. Walheim, S.; Boltau, M.; Mlynek, J.; Krausch, G.; Steiner, U. Structure formation via polymer demixing in spin-cast films. *Macromolecules* **1997,** *30*, 4995.

29. Li, Y. M.; Kim, W.; Zhang, Y. G.; Rolandi, M.; Wang, D. W.; Dai, H. J. Growth of single-walled carbon nanotubes from discrete catalytic nanoparticles of various sizes. *J. Phys. Chem. B* **2001,** *105*, 11424.

30. Block, S.; Gloeckl, G.; Weitschies, W.; Helm, C. A. Direct visualization and identification of biofunctionalized nanoparticles using a magnetic atomic force microscope. *Nano Lett.* **2011,** *11*, 3587.

31. Bett, C. K.; Ngunjiri, J. N.; Serem, W. K.; Fontenot, K. R.; Hammer, R. P.; McCarley, R. L.; Garno, J. C. Structure-activity relationships in peptide modulators of beta-amyloid protein aggregation: Variation in alpha,alpha-disubstitution results in altered aggregate size and morphology. *ACS Chemical Neuroscience* **2010,** *1*, 608.

32. Oberhauser, A. F.; Hansma, P. K.; Carrion-Vazquez, M.; Fernandez, J. M. Stepwise unfolding of titin under force-clamp atomic force microscopy. *P Natl. Acad. Sci. USA* **2001,** *98*, 468.

33. Lyubchenko, Y. L.; Shlyakhtenko, L. S. AFM for analysis of structure and dynamics of DNA and protein-DNA complexes. *Methods* **2009,** *47*, 206.

34. Neupane, G. P.; Dhakal, K. P.; Kim, M. S.; Lee, H.; Guthold, M.; Joseph, V. S.; Hong, J.-D.; Kim, J. Simple method of DNA stretching on glass substrate for fluorescence imaging and spectroscopy. *J. Biomed. Opt.* **2014,** *19*, 051210.

35. Pillet, F.; Chopinet, L.; Formosa, C.; Dague, E. Atomic force microscopy and pharmacology: From microbiology to cancerology. *Biochim. Biophys. Acta* **2014,** *1840*, 1028.

36. Lulevich, V.; Zink, T.; Chen, H.-Y.; Liu, F.-T.; Liu, G.-y. Cell mechanics using atomic force microscopy-based single-cell compression. *Langmuir* **2006,** *22*, 8151.

37. Fang, F. Z.; Venkatesh, V. C. Diamond cutting of silicon with nanometric finish. *CIRP Annals - Manufacturing Technology* **1998,** *47*, 45.

38. Goksu, E. I.; Vanegas, J. M.; Blanchette, C. D.; Lin, W. C.; Longo, M. L. AFM for structure and dynamics of biomembranes. *BBA-Biomembranes* **2009,** *1788*, 254.

39. Vorburger, T. V.; Dagata, J. A.; Wilkening, G.; Lizuka, K.; Thwaite, E. G.; Lonardo, P. Industrial uses of STM and AFM. *CIRP Annals - Manufacturing Technology* **1997,** *46*, 597.

40. Tian, T.; Singhana, B.; Englade-Franklin, L. E.; Zhai, X.; Lee, T. R.; Garno, J. C. Surface assembly and nanofabrication of 1,1,1-tris(mercaptomethyl)heptadecane on Au(111) studied with time-lapse atomic force microscopy. *Beilstein J. Nanotech.* **2014,** *5*, 26.

41. Ngunjiri, J.; Garno, J. C. AFM-based lithography for nanoscale protein assays. *Anal. Chem.* **2008,** *80*, 1361.

42. Reviakine, I.; Brisson, A. Formation of supported phospholipid bilayers from unilamellar vesicles investigated by atomic force microscopy. *Langmuir* **2000,** *16*, 1806.

43. Fotiadis, D.; Scheuring, S.; Muller, S. A.; Engel, A.; Muller, D. J. Imaging and manipulation of biological structures with the AFM. *Micron* **2002,** *33*, 385.

44. Allen, M. J.; Hud, N. V.; Balooch, M.; Tench, R. J.; Siekhaus, W. J.; Balhorn, R. Tip-radius-induced artifacts in AFM images of protamine-complexed DNA fibers. *Ultramicroscopy* **1992,** *42*, 1095.

45. Tabet, M. F.; Urban, F. K. Deconvolution of tip affected atomic force microscope images and comparison to Rutherford backscattering spectrometry. *J. Vac. Sci. Technol. B* **1997,** *15*, 800.

46. Markiewicz, P.; Goh, M. C. Simulation of atomic-force microscope tip-sample resonstructionI. *J. Vac. Sci. Technol. B* **1995,** *13*, 1115.

47. Markiewicz, P.; Goh, M. C. Atomic force microscopy probe tip visualization and improvement of images using a simple deconvolution procedure. *Langmuir* **1994,** *10*, 5.

48. Hafner, J. H.; Cheung, C. L.; Woolley, A. T.; Lieber, C. M. Structural and functional imaging with carbon nanotube AFM probes. *Prog. Biophys. Mol. Bio.* **2001,** *77*, 73.

49. Moheimani, S. O. R. Accurate and fast nanopositioning with piezoelectric tube scanners: Emerging trends and future challenges. *Rev. Sci. Instrum.* **2008,** *79*.

50. Binnig, G.; Smith, D. P. E. Single-tube 3-dimensional scanner for scanning tunneling microscopy. *Rev. Sci. Instrum.* **1986,** *57*, 1688.

51. Erlandsson, R.; McClelland, G. M.; Mate, C. M.; Chiang, S. Atomic force microscopy using optical interferometry. *J. Vac. Sci. Technol. A* **1988,** *6*, 266.

52. Peng, Z. Q.; West, P. Crystal sensor for microscopy applications. *Appl. Phys. Lett.* **2005,** *86*.

53. Martin, Y.; Williams, C. C.; Wickramasinghe, H. K. Atomic force microscope–force mapping and profiling on a sub 100-Å scale. *J. Appl. Phys.* **1987,** *61*, 4723.

54. Mate, C. M.; McClelland, G. M.; Erlandsson, R.; Chiang, S. Atomic-scale friction of a tungsten tip on a graphite surface. *Phys. Rev. Lett.* **1987,** *59*, 1942.

55. Maivald, P.; Butt, H. J.; Gould, S. A. C.; Prater, C. B.; Drake, B.; Gurley, J. A.; Elings, V. B.; Hansma, P. K. Using force modulation to image surface elasticities with the atomic force microscope. *Nanotechnology* **1991,** *2*, 103.

56. Kelley, T. W.; Granstrom, E. L.; Frisbie, C. D. Conducting probe atomic force microscopy: A characterization tool for molecular electronics. *Adv. Mater.* **1999,** *11*, 261.

57. Martin, Y.; Wickramasinghe, H. K. Magnetic imaging by force microscopy with 1000-A resolution. *Appl. Phys. Lett.* **1987,** *50*, 1455.

58. Sidles, J. A.; Garbini, J. L.; Bruland, K. J.; Rugar, D.; Zuger, O.; Hoen, S.; Yannoni, C. S. Magnetic-resonance force microscopy. *Rev. Mod. Phys.* **1995,** *67*, 249.

59. Guthner, P.; Dransfeld, K. Local poling of ferroelectric polymers by scanning force microscopy. *Appl. Phys. Lett.* **1992,** *61*, 1137.

60. Martin, Y.; Abraham, D. W.; Wickramasinghe, H. K. High-resolution capacitance measurement and potentiometry by force microscopy. *Appl. Phys. Lett.* **1988,** *52*, 1103.

61. Zhong, Q.; Inniss, D.; Kjoller, K.; Elings, V. B. Fractured polymer silica fiber surface studied by tapping mode atomic-force microscopy. *Surf. Sci.* **1993,** *290*, L688.

62. Han, W. H.; Lindsay, S. M.; Jing, T. W. A magnetically driven oscillating probe microscope for operation in liquids. *Appl. Phys. Lett.* **1996,** *69*, 4111.

63. Daniels, S. L.; Ngunjiri, J. N.; Garno, J. C. Investigation of the magnetic properties of ferritin by AFM imaging with magnetic sample modulation. *Anal. Bioanal. Chem.* **2009,** *394*, 215.

64. Nonnenmacher, M.; Oboyle, M. P.; Wickramasinghe, H. K. Kelvin probe force microscopy. *Appl. Phys. Lett.* **1991,** *58*, 2921.

65. Cappella, B.; Dietler, G. Force-distance curves by atomic force microscopy. *Surf. Sci. Rep.* **1999,** *34*, 1.

66. Radmacher, M.; Cleveland, J. P.; Fritz, M.; Hansma, H. G.; Hansma, P. K. Mapping interaction forces with the atomic-force microscope. *Biophys. J.* **1994,** *66*, 2159.

67. Balzer, B. N.; Micciulla, S.; Dodoo, S.; Zerball, M.; Gallei, M.; Rehahn, M.; v Klitzing, R.; Hugel, T. Adhesion property profiles of supported thin polymer films. *ACS Appl. Mater. Interfaces* **2013,** *5*, 6300.

68. Razvag, Y.; Gutkin, V.; Reches, M. Probing the interaction of individual amino acids with inorganic surfaces using atomic force spectroscopy. *Langmuir* **2013,** *29*, 10102.

69. Bujalowski, P. J.; Oberhauser, A. F. Tracking unfolding and refolding reactions of single proteins using atomic force microscopy methods. *Methods* **2013,** *60*, 151.

70. Reeves, K. J.; Hou, J.; Higham, S. E.; Sun, Z.; Trzeciakowski, J. P.; Meininger, G. A.; Brown, N. J. Selective measurement and manipulation of adhesion forces between cancer cells and bone marrow endothelial cells using atomic force microscopy. *Nanomedicine* **2013,** *8*, 921.

71. Guo, S.; Li, N.; Lad, N.; Desai, S.; Akhremitchev, B. B. Distributions of parameters and features of multiple bond ruptures in force spectroscopy by atomic force microscopy. *J. Phys. Chem. C* **2010,** *114*, 8755.

72. Lyles, V.; Serem, W.; Yu, J.-J.; Garno, J. Surface characterization using atomic force microscopy (AFM) in liquid environments. In *Surface Science Techniques*, Bracco, G.; Holst, B., Eds. Springer Berlin Heidelberg: 2013; Vol. 51, pp 599.

73. Ascoli, C.; Dinelli, F.; Frediani, C.; Petracchi, D.; Salerno, M.; Labardi, M.; Allegrini, M.; Fuso, F. Normal and lateral forces in scanning force microscopy. *J. Vac. Sci. Technol. B* **1994,** *12*, 1642.

74. Rogers, B.; York, D.; Whisman, N.; Jones, M.; Murray, K.; Adams, J. D.; Sulchek, T.; Minne, S. C. Tapping mode atomic force microscopy in liquid with an insulated piezoelectric microactuator. *Rev. Sci. Instrum.* **2002,** *73*, 3242.

75. Li, J. R.; Garno, J. C. Elucidating the role of surface hydrolysis in preparing organosilane nanostructures via particle lithography. *Nano Lett.* **2008,** *8*, 1916.

76. Tamayo, J.; García, R. Relationship between phase shift and energy dissipation in tapping-mode scanning force microscopy. *Appl. Phys. Lett.* **1998,** *73*, 2926.

77. Martínez, N.; García, R. Measuring phase shifts and energy dissipation with amplitude modulation atomic force microscopy. *Nanotechnology* **2006,** *17*, S167.

78. Tamayo, J.; García, R. Deformation, contact time, and phase contrast in tapping mode scanning force microscopy. *Langmuir* **1996,** *12*, 4430.

79. Bar, G.; Thomann, Y.; Brandsch, R.; Cantow, H. J.; Whangbo, M. H. Factors affecting the height and phase images in tapping mode atomic force microscopy. Study of phase-separated polymer blends of poly(ethene-co-styrene) and poly(2,6-dimethyl-1,4-phenylene oxide). *Langmuir* **1997,** *13*, 3807.

80. Leclère, P.; Lazzaroni, R.; Brédas, J. L.; Yu, J. M.; Dubois, P.; Jérôme, R. Microdomain morphology analysis of block copolymers by atomic force microscopy with phase detection imaging. *Langmuir* **1996,** *12*, 4317.

81. van den Berg, R.; de Groot, H.; van Dijk, M. A.; Denley, D. R. Atomic force microscopy of thin triblock copolymer films. *Polymer* **1994,** *35*, 5778.

82. Ulman, A. Formation and structure of self-assembled monolayers. *Chem. Rev.* **1996,** *96*, 1533.

83. Schreiber, F. Structure and growth of self-assembling monolayers. *Prog. Surf. Sci.* **2000,** *65*, 151.

84. Ewers, B. W.; Batteas, J. D. Molecular dynamics simulations of alkylsilane monolayers on silica nanoasperities: Impact of surface curvature on monolayer structure and pathways for energy dissipation in tribological contacts. *J. Phys. Chem. C* **2012,** *116*, 25165.

85. Cheng, H.; Hu, Y. Influence of chain ordering on frictional properties of self-assembled monolayers (SAMs) in nano-lubrication. *Adv. Colloid. Interfac.* **2012,** *171*, 53.

86. Samanta, D.; Sarkar, A. Immobilization of bio-macromolecules on self-assembled monolayers: methods and sensor applications. *Chem. Soc. Rev.* **2011,** *40*, 2567.

87. Nuzzo, R. G.; Allara, D. L. Adsorption of bifunction organic disulfides on gold surfaces. *J. Am. Chem. Soc.* **1983,** *105*, 4481.

88. Love, J. C.; Estroff, L. A.; Kriebel, J. K.; Nuzzo, R. G.; Whitesides, G. M. Self-assembled monolayers of thiolates on metals as a form of nanotechnology. *Chem. Rev.* **2005,** *105*, 1103.

89. Duwez, A. S. Exploiting electron spectroscopies to probe the structure and organization of self-assembled monolayers: a review. *J. Electron Spectrosc.* **2004,** *134*, 97.

90. Aizenberg, J.; Black, A. J.; Whitesides, G. H. Oriented growth of calcite controlled by self-assembled monolayers of functionalized alkanethiols supported on gold and silver. *J. Am. Chem. Soc.* **1999,** *121*, 4500.

91. Garno, J. C.; Zangmeister, C. D.; Batteas, J. D. Directed electroless growth of metal nanostructures on patterned self-assembled monolayers. *Langmuir* **2007,** *23*, 7874.

92. Kane, R. S.; Takayama, S.; Ostuni, E.; Ingber, D. E.; Whitesides, G. M. Patterning proteins and cells using soft lithography. *Biomater.* **1999,** *20*, 2363.

93. Vallant, T.; Kattner, J.; Brunner, H.; Mayer, U.; Hoffmann, H. Investigation of the formation and structure of self-assembled alkylsiloxane monolayers on silicon using in situ attenuated total reflection infrared spectroscopy. *Langmuir* **1999,** *15*, 5339.

94. Li, J. R.; Garno, J. C. Elucidating the role of surface hydrolysis in preparing organosilane nanostructures via particle lithography. *Nano Lett.* **2008,** *8*, 1916.

95. Mathauer, K.; Frank, C. W. Binary self-assembled monolayers as prepared by successive adsorption of alkyltrichlorosilanes. *Langmuir* **1993,** *9*, 3446.

96. Grabar, K. C.; Freeman, R. G.; Hommer, M. B.; Natan, M. J. Preparation and characterization of Au colliod monolayers. *Anal. Chem.* **1995,** *67*, 735.

97. Kurth, D. G.; Bein, T. Thin-films of (3-aminoproply)triethoxysilane on aluminum oxide and gold substrates. *Langmuir* **1995,** *11*, 3061.

98. Tillman, N.; Ulman, A.; Schildkraut, J. S.; Penner, T. L. Incorporation of phenoxy groups in self-assembled monolayers on trichlorosilane derivatives - Effects on film thickness, wettability, and molecular-orientation. *J. Am. Chem. Soc.* **1988,** *110*, 6136.

99. Mutin, P. H.; Guerrero, G.; Vioux, A. Hybrid materials from organophosphorus coupling molecules. *J. Mater. Chem.* **2005,** *15*, 3761.

100. Legrange, J. D.; Markham, J. L.; Kurkjian, C. R. Effects of surface hydration on the deposition of silane monolayers on silica. *Langmuir* **1993,** *9*, 1749.

101. McGovern, M. E.; Kallury, K. M. R.; Thompson, M. Role of solvent on the silanization of glass with octadecyltrichlorosilane. *Langmuir* **1994,** *10*, 3607.

102. Sagiv, J. Organized monolayers by adsorption .1. Formation and structure of oleophobic mixed monolayers on solid-surfaces. *J. Am. Chem. Soc.* **1980,** *102*, 92.

103. Lercel, M. J.; Craighead, H. G.; Parikh, A. N.; Seshadri, K.; Allara, D. L. Sub-10 nm lithography with self-assembled monolayers. *Appl. Phys. Lett.* **1996,** *68*, 1504.

104. Golzhauser, A.; Eck, W.; Geyer, W.; Stadler, V.; Weimann, T.; Hinze, P.; Grunze, M. Chemical nanolithography with electron beams. *Adv. Mater.* **2001,** *13*, 806.

105. Wang, D. W.; Thomas, S. G.; Wang, K. L.; Xia, Y. N.; Whitesides, G. M. Nanometer scale patterning and pattern transfer on amorphous Si, crystalline Si, and SiO2 surfaces using self-assembled monolayers. *Appl. Phys. Lett.* **1997,** *70*, 1593.

106. Mirkin, C. A.; Hong, S. H.; Demers, L. Dip-pen nanolithography: Controlling surface architecture on the sub-100 nanometer length scale. *Chem Phys Chem* **2001,** *2*, 37.

107. Xu, S.; Miller, S.; Laibinis, P. E.; Liu, G. Y. Fabrication of nanometer scale patterns within self-assembled monolayers by nanografting. *Langmuir* **1999,** *15*, 7244.

108. Kramer, S.; Fuierer, R. R.; Gorman, C. B. Scanning probe lithography using self-assembled monolayers. *Chem. Rev.* **2003,** *103*, 4367.

109. Ingert, D.; Pileni, M. P. Nanocrystals used as masks for nanolithography. *J. Phys. Chem. B* **2003,** *107*, 9617.

110. Snyder, C. E.; Yake, A. M.; Feick, J. D.; Velegol, D. Nanoseale functionalization and site-specific assembly of colloids by particle lithography. *Langmuir* **2005,** *21*, 4813.

111. Xia, Y. N.; Rogers, J. A.; Paul, K. E.; Whitesides, G. M. Unconventional methods for fabricating and patterning nanostructures. *Chem. Rev.* **1999,** *99*, 1823.

112. Deckman, H. W.; Dunsmuir, J. H. Natural lithography. *Appl. Phys. Lett.* **1982,** *41*, 377.

113. Hulteen, J. C.; Vanduyne, R. P. Nanosphere lithography - A materials general fabrication process for periodic particle array surfaces. *J. Vac. Sci. Technol. A* **1995,** *13*, 1553.

114. Lewandowski, B. R.; Kelley, A. T.; Singleton, R.; Li, J. R.; Lowry, M.; Warner, I. M.; Garno, J. C. Nanostructures of cysteine-coated CdS nanoparticles produced with "two-particle" lithography. *J. Phys. Chem. C* **2009,** *113*, 5933.

115. Taylor, Z. R.; Patel, K.; Spain, T. G.; Keay, J. C.; Jernigen, J. D.; Sanchez, E. S.; Grady, B. P.; Johnson, M. B.; Schmidtke, D. W. Fabrication of protein dot arrays via particle lithography. *Langmuir* **2009,** *25*, 10932.

116. Lusker, K. L.; Yu, J. J.; Garno, J. C. Particle lithography with vapor deposition of organosilanes: A molecular toolkit for studying confined surface reactions in nanoscale liquid volumes. *Thin Solid Films* **2011,** *519*, 5223.

117. Haynes, C. L.; Van Duyne, R. P. Dichroic optical properties of extended nanostructures fabricated using angle-resolved nanosphere lithography. *Nano Lett.* **2003,** *3*, 939.

118. Haynes, C. L.; Van Duyne, R. P. Nanosphere lithography: A versatile nanofabrication tool for studies of size-dependent nanoparticle optics. *J. Phys. Chem. B* **2001,** *105*, 5599.

119. Li, J. R.; Lusker, K. L.; Yu, J. J.; Garno, J. C. Engineering the spatial selectivity of surfaces at the nanoscale using particle lithography combined with vapor deposition of organosilanes. *ACS nano* **2009,** *3*, 2023.

120. Lusker, K. L.; Li, J.-R.; Garno, J. C. Nanostructures of functionalized gold nanoparticles prepared by particle lithography with organosilanes. *Langmuir* **2011,** *in press*, ASAP.

121. Kelley, A. T.; Serem, W. K.; Daniels, S. L.; Englade-Franklin, L. E.; Morrison, G.; Flurry, N.; Chan, J. Y.; Garno, J. C. Vibrational response of FeNi3 nanoparticles to the flux of a modulated electromagnetic field detected by contact-mode atomic force microscopy. *J. Phys. Chem. C* **2013,** *117*, 18768.

122. Giessibl, F. J. Advances in atomic force microscopy. *Rev. Mod. Phys.* **2003,** *75*, 949.

123. Rugar, D.; Mamin, H. J.; Guethner, P.; Lambert, S. E.; Stern, J. E.; McFadyen, I.; Yogi, T. Magnetic force microscopy - General principles and application to longitudinal recording media. *J. Appl. Phys.* **1990,** *68*, 1169.

124. Puntes, V. F.; Gorostiza, P.; Aruguete, D. M.; Bastus, N. G.; Alivisatos, A. P. Collective behaviour in two-dimensional cobalt nanoparticle assemblies observed by magnetic force microscopy. *Nat. Mater.* **2004,** *3*, 263.

125. Schonenberger, C.; Alvarado, S. F. Understanding magnetic force microscopy. *Z. Phys. B-Condens. Mat.* **1990,** *80*, 373.

126. Hartmann, U. Magnetic force microscopy. *Annu. Rev. Mater. Sci.* **1999,** *29*, 53.

127. Winzer, M.; Kleiber, M.; Dix, N.; Wiesendanger, R. Fabrication of nano-dot- and nano-ring-arrays by nanosphere lithography. *Appl. Phys. A* **1996,** *63*, 617.

128. Chao, S. H.; Dougherty, W. M.; Garbini, J. L.; Sidles, J. A. Nanometer-scale magnetic resonance imaging. *Rev. Sci. Instrum.* **2004,** *75*, 1175.

129. Kuehn, S.; Hickman, S. A.; Marohn, J. A. Advances in mechanical detection of magnetic resonance. *J. Chem. Phys.* **2008,** *128*.

130. Degen, C. L.; Poggio, M.; Mamin, H. J.; Rettner, C. T.; Rugar, D. Nanoscale magnetic resonance imaging. *P. Natl. Acad. Sci. USA* **2009,** *106*, 1313.

131. Mamin, H. J.; Poggio, M.; Degen, C. L.; Rugar, D. Nuclear magnetic resonance imaging with 90-nm resolution. *Nat. Nanotechnol.* **2007,** *2*, 301.

132. Rugar, D.; Yannoni, C. S.; Sidles, J. A. Mechanical detection of magnetic-resonance. *Nature* **1992,** *360*, 563.

133. Daniels, S.; Ngunjiri, J.; Garno, J. Investigation of the magnetic properties of ferritin by AFM imaging with magnetic sample modulation. *Anal. Bioanal. Chem.* **2009,** *394*, 215.

134. Li, J. R.; Lewandowski, B. R.; Xu, S.; Garno, J. C. Detecting the magnetic response of iron oxide capped organosilane nanostructures using magnetic sample modulation and atomic force microscopy. *Anal. Chem.* **2009,** *81*, 4792.

135. Ge, G. L.; Han, D.; Lin, D. Y.; Chu, W. G.; Sun, Y. X.; Jiang, L.; Ma, W. Y.; Wang, C. MAC mode atomic force microscopy studies of living samples, ranging from cells to fresh tissue. *Ultramicroscopy* **2007,** *107*, 299.

136. Canetta, E.; Adya, A. K. Atomic force microscopy : applications to nanobiotechnology. *J. Indian Chem. Soc.* **2005,** *82*, 1147.

137. Han, W. H.; Dlakic, M.; Zhu, Y. W. J.; Lindsay, S. M.; Harrington, R. E. Strained DNA is kinked by low concentrations of Zn^{2+}. *P. Natl. Acad. Sci. USA* **1997,** *94*, 10565.

138. Leuba, S. H.; Lindsay, S. M. Magnetically driven oscillating probe ("MAC mode") scanning force microscopy (SFM) of chromatin fibers in aqueous buffer. *Biophys. J.* **1998,** *74*, A71.

139. Zhang, Z.; Hammel, P. C.; Wigen, P. E. Observation of ferromagnetic resonance in a microscopic sample using magnetic resonance force microscopy. *Appl. Phys. Lett.* **1996,** *68*, 2005.

140. Bausch, A. R.; Ziemann, F.; Boulbitch, A. A.; Jacobson, K.; Sackmann, E. Magnetic-resonance force microscopy. *Rev. Mod. Phys.* **1995,** *67*, 249.

141. Porthun, S.; Abelmann, L.; Lodder, C. Magnetic force microscopy of thin film media for high density magnetic recording. *J. Magn. Magn. Mater.* **1998,** *182*, 238.

142. Hehn, M.; Padovani, S.; Ounadjela, K.; Bucher, J. P. Nanoscale magnetic domain structures in epitaxial cobalt films. *Phys. Rev. B* **1996,** *54*, 3428.

143. Belliard, L.; Miltat, J.; Thiaville, A.; Dubois, S.; Duvail, J. L.; Piraux, L. Observing magnetic nanowires by means of magnetic force microscopy. *J. Magn. Magn. Mater.* **1998,** *190*, 1.

144. Qin, D. H.; Lu, M.; Li, H. L. Magnetic force microscopy of magnetic domain structure in highly ordered Co nanowire arrays. *Chem. Phys. Lett.* **2001,** *350*, 51.

145. Grutter, P.; Rugar, D.; Mamin, H. J.; Castillo, G.; Lin, C. J.; McFadyen, I. R.; Valletta, R. M.; Wolter, O.; Bayer, T.; Greschner, J. Magnetic force microscopy with batch-fabricated force sensors. *J. Appl. Phys.* **1991,** *69*, 5883.

146. Fischer, P. B.; Wei, M. S.; Chou, S. Y. Ultrahigh-resolution magnetic force microscope tip fabricated using electron-beam lithography. *J. Vac. Sci. Technol. B* **1993,** *11*, 2570.

147. Kim, D.; Chung, N. K.; Allen, S.; Tendler, S. J. B.; Park, J. W. Ferritin-based new magnetic force microscopic probe detecting 10 nm sized magnetic nanoparticles. *ACS Nano* **2012,** *6*, 241.

148. Liu, X.; Isomura, S.; Morisako, A. Magnetic force microscope probes with high resolution by soft magnetic vortex. *IEEE Trans. Magn.* **2012,** *48*, 3673.

149. Serem, W.; Varotto, A.; Castro, G.; Drain, C. M.; Garno, J. C. Magnetic properties of metal nanoparticles investigated by AFM combined with magnetic sample modulation. *Abstr. Pap. Am. Chem. S.* **2008,** *235*.

150. Gibbs, M. R. J. Nanomagnetism - nascent or fully formed? *Curr. Opin. Solid State Mater. Sci* **2003,** *7*, 83.

151. Roduner, E. Size matters: why nanomaterials are different. *Chem. Soc. Rev.* **2006,** *35*, 583.

152. Lu, A. H.; Salabas, E. L.; Schuth, F. Magnetic nanoparticles: Synthesis, protection, functionalization, and application. *Angew. Chem. Int. Edit.* **2007,** *46*, 1222.

153. Douglass, D. C.; Cox, A. J.; Bucher, J. P.; Bloomfield, L. A. Magnetic-properties of free cobalt and gadolinium clusters. *Phys. Rev. B* **1993,** *47*, 12874.

154. Bonnemain, B. Superparamagnetic agents in magnetic resonance imaging: Physicochemical characteristics and clinical applications - A review. *J. Drug Target.* **1998,** *6*, 167.

155. Berry, C. C.; Curtis, A. S. G. Functionalisation of magnetic nanoparticles for applications in biomedicine. *J. Phys. D: Appl. Phys.* **2003,** *36*, R198.

156. Hyeon, T. Chemical synthesis of magnetic nanoparticles. *Chem. Commun.* **2003**, 927.

157. Frey, N. A.; Peng, S.; Cheng, K.; Sun, S. Magnetic nanoparticles: synthesis, functionalization, and applications in bioimaging and magnetic energy storage. *Chem. Soc. Rev.* **2009,** *38*, 2532.

158. Darling, S. B.; Bader, S. D. A materials chemistry perspective on nanomagnetism. *J. Mater. Chem.* **2005,** *15*, 4189.

159. Terris, B. D.; Thomson, T. Nanofabricated and self-assembled magnetic structures as data storage media. *J. Phys. D: Appl. Phys.* **2005,** *38*, R199.

160. Sousa, M. H.; Tourinho, F. A.; Depeyrot, J.; da Silva, G. J.; Lara, M. C. F. L. New electric double-layered magnetic fluids based on copper, nickel, and zinc ferrite nanostructures. *J. Phys. Chem. B* **2001,** *105*, 1168.

161. Shen, L.; Laibinis, P. E.; Hatton, T. A. Bilayer surfactant stabilized magnetic fluids: Synthesis and interactions at interfaces. *Langmuir* **1998,** *15*, 447.

162. Roger, J.; Pons, J. N.; Massart, R.; Halbreich, A.; Bacri, J. C. Some biomedical applications of ferrofluids. *Eur. Phys. J. Appl. Phys* **1999,** *5*, 321.

163. Morup, S. Superferromagnetic nanostructures. *Hyperfine Interactions* **1994,** *90*, 171.

164. Pankhurst, Q. A.; Connolly, J.; Jones, S. K.; Dobson, J. Applications of magnetic nanoparticles in biomedicine. *J. Phys. D: Appl. Phys.* **2003,** *36*, R167.

165. Wang, Y. X. J.; Hussain, S. M.; Krestin, G. P. Superparamagnetic iron oxide contrast agents: physicochemical characteristics and applications in MR imaging. *Eur. Radiol.* **2001,** *11*, 2319.

166. Mornet, S.; Vasseur, S.; Grasset, F.; Duguet, E. Magnetic nanoparticle design for medical diagnosis and therapy. *J. Mater. Chem.* **2004,** *14*, 2161.

167. Bulte, J. W. M.; Kraitchman, D. L. Iron oxide MR contrast agents for molecular and cellular imaging. *NMR Biomed.* **2004,** *17*, 484.

168. Chang, E.; Chalikonda, S.; Friedl, J.; Xu, H.; Phan, G. Q.; Marincola, F. M.; Alexander, H. R.; Bartlett, D. L. Targeting vaccinia to solid tumors with local hyperthermia. *Hum. Gene Ther.* **2005,** *16*, 435.

169. Ito, A.; Shinkai, M.; Honda, H.; Yoshikawa, K.; Saga, S.; Wakabayashi, T.; Yoshida, J.; Kobayashi, T. Heat shock protein 70 expression induces antitumor immunity during intracellular hyperthermia using magnetite nanoparticles. *Cancer Immunol. Immun.* **2003,** *52*, 80.

170. Latham, A. H.; Williams, M. E. Controlling transport and chemical functionality of magnetic nanoparticles. *Acc. Chem. Res.* **2008,** *41*, 411.

171. Jun, Y.-W.; Seo, J.-W.; Cheon, A. Nanoscaling laws of magnetic nanoparticles and their applicabilities in biomedical sciences. *Acc. Chem. Res.* **2008,** *41*, 179.

172. Herdt, A. R.; Kim, B.-S.; Taton, T. A. Encapsulated magnetic nanoparticles as supports for proteins and recyclable biocatalysts. *Bioconjugate Chem.* **2007,** *18*, 183.

173. Chu, M. Q.; Song, X.; Cheng, D.; Liu, S. P.; Zhu, J. Preparation of quantum dot-coated magnetic polystyrene nanospheres for cancer cell labelling and separation. *Nanotechnology* **2006,** *17*, 3268.

174. Berry, C. C. Progress in functionalization of magnetic nanoparticles for applications in biomedicine. *J. Phys. D: Appl. Phys.* **2009,** *42*.

175. Bedanta, S.; Kleemann, W. Supermagnetism. *J. Phys. D: Appl. Phys.* **2009,** *42*.

176. Saner, C. K.; Lusker, K. L.; LeJeune, Z. M.; Serem, W. K.; Garno, J. C. Self-assembly of octadecyltrichlorosilane: Surface structures formed using different protocols of particle lithography. *Beilstein J. Nanotech.* **2012,** *3*, 114.

177. Lusker, K. L.; Li, J.-R.; Garno, J. C. Nanostructures of functionalized gold nanoparticles prepared by particle lithography with organosilanes. *Langmuir* **2011,** *27*, 13269.

178. Samson, J.; Varotto, A.; Nahirney, P. C.; Toschi, A.; Piscopo, I.; Drain, C. M. Fabrication of metal nanoparticles using toroidal plasmid DNA as a sacrificial mold. *ACS Nano* **2009,** *3*, 339.

179. Cushing, B. L.; Kolesnichenko, V. L.; O'Connor, C. J. Recent advances in the liquid-phase syntheses of inorganic nanoparticles. *Chem. Rev.* **2004,** *104*, 3893.

180. Bilecka, I.; Niederberger, M. Microwave chemistry for inorganic nanomaterials synthesis. *Nanoscale* **2010,** *2*, 1358.

181. Gerbec, J. A.; Magana, D.; Washington, A.; Strouse, G. F. Microwave-enhanced reaction rates for nanoparticle synthesis. *J. Am. Chem. Soc.* **2005,** *127*, 15791.

182. Leonelli, C.; Mason, T. J. Microwave and ultrasonic processing: Now a realistic option for industry. *Chem. Eng. Process.* **2010,** *49*, 885.

183. Tsuji, M.; Hashimoto, M.; Nishizawa, Y.; Kubokawa, M.; Tsuji, T. Microwave-assisted synthesis of metallic nanostructures in solution. *Chem. - Eur. J.* **2005,** *11*, 440.

184. Liao, Q. L.; Tannenbaum, R.; Wang, Z. L. Synthesis of $FeNi_3$ alloyed nanoparticles by hydrothermal reduction. *J. Phys. Chem. B* **2006,** *110*, 14262.

185. Antony, H.; Peulon, S.; Legrand, L.; Chaussé, A. Electrochemical synthesis of lepidocrocite thin films on gold substrate--EQCM, IRRAS, SEM and XRD study. *Electrochim. Acta* **2004,** *50*, 1015.

186. Huber, D. L. Synthesis, properties, and applications of iron nanoparticles. *Small* **2005,** *1*, 482.

187. Daniels, S. L.; Serem, W. K.; Garno, J. C. Ferritin as a model nanomaterial: Nanolithography and scanning probe microscopy studies *J. Nano. Lett.* **2012,** *2*.

188. Fankuchen, I. Ferritin V. X-ray diffraction data on ferritin and apoferritin. *J. Biol. Chem.* **1943,** *150*, 57.

189. Hampton, J. K. Hemoglobin iron as a stimulus for the production of ferritin. *Fed. Proc.* **1949,** *8*, 67.

190. Kleinwachter, V. X-ray diffraction study of ferritin-interpretation of low-angle scattering. *Arch. Biochem. Biophys.* **1964,** *105*, 352.

191. Theil, E. C.; Matzapetakis, M.; Liu, X. Ferritins: iron/oxygen biominerals in protein nanocages. *J. Biol. Inorg. Chem.* **2006,** *11*, 803.

192. St Pierre, T. G.; Bell, S. H.; Dickson, D. P. E.; Mann, S.; Webb, J.; Moore, G. R.; Williams, R. J. P. Mossbauer spectrosopic studies of the cores of human, limpet and bacterial ferritins. *Biochim. Biophys. Acta* **1986,** *870*, 127.

193. Schreiber, S.; Savla, M.; Pelekhov, D. V.; Iscru, D. F.; Selcu, C.; Hammel, P. C.; Agarwal, G. Magnetic force microscopy of superparamagnetic nanoparticles. *Small* **2008,** *4*, 270.

194. Garno, J. C.; Amro, N. A.; Wadu-Mesthrige, K.; Liu, G.-Y. Production of periodic arrays of protein nanostructures using particle lithography. *Langmuir* **2002,** *18*, 8186.

195. Ngunjiri, J. N.; Daniels, S. L.; Li, J. R.; Serem, W. K.; Garno, J. C. Controlling the surface coverage and arrangement of proteins using particle lithography. *Nanomedicine* **2008,** *3*, 529.

196. Li, J. R.; Henry, G. C.; Garno, J. C. Fabrication of nanopatterned films of bovine serum albumin and staphylococcal protein A using latex particle lithography. *Analyst* **2006,** *131*, 244.

197. Axford, D. N.; Davis, J. J. Electron flux through apo- and holoferritin. *Nanotechnology* **2007,** *18*.

198. Jun, Y. W.; Huh, Y. M.; Choi, J. S.; Lee, J. H.; Song, H. T.; Kim, S.; Yoon, S.; Kim, K. S.; Shin, J. S.; Suh, J. S.; Cheon, J. Nanoscale size effect of magnetic nanocrystals and their utilization for cancer diagnosis via magnetic resonance imaging. *J. Am. Chem. Soc.* **2005,** *127*, 5732.

199. Leslie-Pelecky, D. L.; Rieke, R. D. Magnetic properties of nanostructured materials. *Chem. Mat.* **1996,** *8*, 1770.

200. Ferrando, R.; Jellinek, J.; Johnston, R. L. Nanoalloys: From theory to applications of alloy clusters and nanoparticles. *Chem. Rev.* **2008,** *108*, 845.

201. Neeleshwar, S.; Chen, C. L.; Tsai, C. B.; Chen, Y. Y.; Chen, C. C.; Shyu, S. G.; Seehra, M. S. Size-dependent properties of CdSe quantum dots. *Phys. Rev. B* **2005,** *71*.

202. Lu, X. G.; Liang, G. Y.; Zhang, Y. M. Synthesis and characterization of magnetic FeNi3 particles obtained by hydrazine reduction in aqueous solution. *Mater. Sci. Eng. B-Adv.* **2007,** *139*, 124.

203. Zhou, X. M.; Wei, X. W. Single crystalline $FeNi_3$ dendrites: Large scale synthesis, formation mechanism, and magnetic properties. *Cryst. Growth & Des.* **2009,** *9*, 7.

204. Wang, H. Z.; Li, J. G.; Kou, X. L.; Zhang, L. Synthesis and characterizations of size-controlled $FeNi_3$ nanoplatelets. *J. Chryst. Growth* **2008,** *310*, 3072.

205. Pastoriza-Santos, I.; Liz-Marzan, L. M. Formation of PVP-protected metal nanoparticles in DMF. *Langmuir* **2002,** *18*, 2888.

206. Tu, W. X.; Liu, H. F. Rapid synthesis of nanoscale colloidal metal clusters by microwave irradiation. *J. Mater. Chem.* **2000,** *10*, 2207.

207. Abdelsayed, V.; Aljarash, A.; El-Shall, M. S.; Al Othman, Z. A.; Alghamdi, A. H. Microwave synthesis of bimetallic nanoalloys and CO oxidation on ceria-supported nanoalloys. *Chem. Mat.* **2009,** *21*, 2825.

208. Reverchon, E.; Adami, R. Nanomaterials and supercritical fluids. *J. Supercrit. Fluids* **2006,** *37*, 1.

209. Byrappa, K.; Adschiri, T. Hydrothermal technology for nanotechnology. *Prog. Cryst. Growth Ch.* **2007,** *53*, 117.

210. CNJ, W. *Adv. X-ray Analys.* **1964,** *7*, 46.

211. Osaka, T.; Matsunaga, T.; Nakanishi, T.; Arakaki, A.; Niwa, D.; Iida, H. Synthesis of magnetic nanoparticles and their application to bioassays. *Anal. Bioanal. Chem.* **2006,** *384*, 593.

212. Gupta, A. K.; Gupta, M. Synthesis and surface engineering of iron oxide nanoparticles for biomedical applications. *Biomater.* **2005,** *26*, 3995.

213. Weinstein, J. S.; Varallyay, C. G.; Dosa, E.; Gahramanov, S.; Hamilton, B.; Rooney, W. D.; Muldoon, L. L.; Neuwelt, E. A. Superparamagnetic iron oxide nanoparticles: diagnostic magnetic resonance imaging and potential therapeutic applications in neurooncology and central nervous system inflammatory pathologies, a review. *J. Cereb. Blood Flow Metab.* **2010,** *30*, 15.

214. Teja, A. S.; Koh, P. Y. Synthesis, properties, and applications of magnetic iron oxide nanoparticles. *Prog. Crystal Growth Char. Mater.* **2009,** *55*, 22.

215. Blawas, A. S.; Reichert, W. M. Protein patterning. *Biomater.* **1998,** *19*, 595.

216. Yang, G.; Garno, J. C.; Liu, G.-Y. Scanning probe-based lithography for production of biological and organic nanostructures on surfaces. In *Comprehensive Nanoscience and Technology*, Andrews, D.; Scholes, G.; Wiederrecht, G., Eds. Elsevier B. V.: Amsterdam, 2010.

217. Ngunjiri, J. N.; Li, J.-R.; Garno, J. C. Nanolithography: Towards fabrication of nanodevices for life sciences. In *Nanodevices for the Life Sciences*, Kumar, C. S. S. R., Ed. Wiley-VCH: Weinheim, 2006.

218. Renault, J. P.; Bernard, A.; Bietsch, A.; Michel, B.; Bosshard, H. R.; Delamarche, E.; Kreiter, M.; Hecht, B.; Wild, U. P. Fabricating arrays of single protein molecules on glass using microcontact printing. *J. Phys. Chem. B* **2003,** *107*, 703.

219. Adams, J.; Tizazu, G.; Janusz, S.; Brueck, S. R. J.; Lopez, G. P.; Leggett, G. J. Large-area nanopatterning of self-assembled monolayers of alkanethiolates by interferometric lithography. *Langmuir* **2010,** *26*, 13600.

220. Dontha, N.; Nowall, W. B.; Kuhr, W. G. Generation of biotin/avidin/enzyme nanostructures with maskless photolithography. *Anal. Chem.* **1997,** *69*, 2619.

221. Blawas, A. S.; Oliver, T. F.; Pirrung, M. C.; Reichert, W. M. Step-and-repeat photopatterning of protein features using caged-biotin-BSA: Characterization and resolution. *Langmuir* **1998,** *14*, 4243.

222. Chen, X. Y.; Su, Y. D.; Ajeti, V.; Chen, S. J.; Campagnola, P. J. Cell adhesion on micro-structured fibronectin gradients fabricated by multiphoton excited photochemistry. *Cell Mol. Bioen.* **2012,** *5*, 307.

223. Ballav, N.; Thomas, H.; Winkler, T.; Terfort, A.; Zharnikov, M. Making protein patterns by writing in a protein-repelling matrix. *Angew. Chem. Int. Edit.* **2009,** *48*, 5833.

224. Jeyachandran, Y. L.; Zharnikov, M. Comprehensive analysis of the effect of electron irradiation on oligo(ethylene glycol) terminated self-assembled monolayers applicable for specific and nonspecific patterning of proteins. *J. Phys. Chem. C* **2012,** *116*, 14950.

225. Kolodziej, C. M.; Kim, S. H.; Broyer, R. M.; Saxer, S. S.; Decker, C. G.; Maynard, H. D. Combination of integrin-binding peptide and growth factor promotes cell adhesion on electron-beam-fabricated patterns. *J. Am. Chem. Soc.* **2012,** *134*, 247.

226. Delamarche, E.; Bernard, A.; Schmid, H.; Bietsch, A.; Michel, B.; Biebuyck, H. Microfluidic networks for chemical patterning of substrate: Design and application to bioassays. *J. Am. Chem. Soc.* **1998,** *120*, 500.

227. Patel, N.; Sanders, G. H. W.; Shakesheff, K. M.; Cannizzaro, S. M.; Davies, M. C.; Langer, R.; Roberts, C. J.; Tendler, S. J. B.; Williams, P. M. Atomic force microscopic analysis of highly defined protein patterns formed by microfluidic networks. *Langmuir* **1999,** *15*, 7252.

228. Lee, K. B.; Park, S. J.; Mirkin, C. A.; Smith, J. C.; Mrksich, M. Protein nanoarrays generated by dip-pen nanolithography. *Science* **2002,** *295*, 1702.

229. Lee, S. W.; Oh, B.-K.; Sanedrin, R. G.; Salaita, K.; Fujigaya, T.; Mirkin, C. A. Biologically active protein nanoarrays generated using parallel dip-pen nanolithography. *Adv. Mater*. **2006,** *18*, 1133.

230. Hyun, J.; Ahn, S. J.; Lee, W. K.; Chilkoti, A.; Zauscher, S. Molecular recognition-mediated fabrication of protein nanostructures by dip-pen lithography. *Nano Lett.* **2002,** *2*, 1203.

231. Choi, D.-S.; Yun, S.-H.; An, Y.-C.; Lee, M.-J.; Kang, D.-G.; Chang, S.-I.; Kim, H.-K.; Kim, K.-M.; Lim, J.-H. Nanopatterning proteins with a stamp tip for dip-pen nanolithography. *Biochip J.* **2007,** *1*, 200.

232. Lee, K. B.; Lim, J.-H.; Mirkin, C. A. Protein nanostructures formed via direct-write dip-pen nanolithography. *J. Am. Chem. Soc.* **2003,** *125*, 5588.

233. Jianhua Gu, C. M. Y., Sha Li, and Chengzhi Cai Nanometric protein arrays on protein-resistant monolayers on silicon surfaces. *J. Am. Chem. Soc.* **2004,** *126*, 8098.

234. Qin, G.; Gu, J.; Liu, K.; Xiao, Z.; Yam, C. M.; Cai, C. Conductive AFM patterning on oligo(ethylene glycol)-terminated alkyl monolayers on silicon substrates: Proposed mechanism and fabrication of avidin patterns. *Langmuir* **2011,** *27*, 6987.

235. Hoff, J. D.; Cheng, L. J.; Meyhofer, E.; Guo, L. J.; Hunt, A. J. Nanoscale protein patterning by imprint lithography. *Nano Lett.* **2004,** *4*, 853.

236. Subramani, C.; Cengiz, N.; Saha, K.; Gevrek, T. N.; Yu, X.; Jeong, Y.; Bajaj, A.; Sanyal, A.; Rotello, V. M. Direct fabrication of functional and biofunctional nanostructures through reactive imprinting. *Adv. Mater.* **2011,** *23*, 3165.

237. Tan, Y. H.; Liu, M.; Nolting, B.; Go, J. G.; Gervay-Hague, J.; Liu, G. Y. A nanoengineering approach for investigation and regulation of protein immobilization. *ACS Nano* **2008,** *2*, 2374.

238. Wadu-Mesthrige, K.; Amro, N. A.; Garno, J. C.; Xu, S.; Liu, G.-Y. Fabrication of nanometer-sized protein patterns using atomic force microscopy and selective immobilization. *Biophys. J.* **2001,** *80*, 1891.

239. Liu, M.; Amro, N. A.; Liu, G.-Y. Nanografting for surface physical chemistry *Annu. Rev. Phys. Chem.* **2008,** *59*, 367.

240. Ngunjiri, J. N.; Stark, D. J.; Tian, T.; Briggman, K. A.; C., G. J. Immobilization of proteins on carboxylic acid-functionalized nanopatterns. *Anal. Bioanal. Chem.* **2012,** *ASAP*, in press.

241. Li, J.-R.; Henry, G. C.; Garno, J. C. Fabrication of nanopatterned films of bovine serum albumin and staphylococcal protein A using latex particle lithography. *Analyst* **2006,** *131*, 244.

242. Ngunjiri, J. N.; Daniels, S. L.; Li, J.-R.; Serem, W. K.; Garno, J. C. Controlling the surface coverage and arrangement of proteins using particle lithography. *Nanomedicine* **2008,** *3*, 529.

243. Taylor, Z. R.; Keay, J. C.; Sanchez, E. S.; Johnson, M. B.; Schmidtke, D. W. Independently controlling protein dot size and spacing in particle lithography. *Langmuir* **2012,** *28*, 9656.

244. Cai, Y.; Ocko, B. M. Large-scale fabrication of protein nanoarrays based on nanosphere lithography. *Langmuir* **2005,** *21*, 9274.

245. Satriano, C.; Fragala, M. E.; Aleeva, Y. Ultrathin and nanostructured ZnO-based films for fluorescence biosensing applications. *J. Colloid Interface Sci.* **2012,** *365*, 90.

246. Lord, S. T. Fibrinogen and fibrin: scaffold proteins in hemostasis. *Curr. Opin, Hematol.* **2007,** *14*, 236.

247. Roach, P.; Eglin, D.; Rohde, K.; Perry, C. C. Modern biomaterials: a review-bulk properties and implications of surface modifications. *J. Mater. Sci.-Mater. Med.* **2007,** *18*, 1263.

248. Horbett, T. A. Principles underlying the role of adsorbed plasma- proteins in blood interactions with foreign materials. *Cardiovasc. Pathol.* **1993,** *2*, S137.

249. Liu, J.; Hlady, V. Chemical pattern on silica surface prepared by UV irradiation of 3-mercaptopropyltriethoxy silane layer: Surface characterization and fibrinogen adsorption. *Colloid Surface B* **1996,** *8*, 25.

250. Corum, L. E.; Hlady, V. The effect of upstream platelet-fibrinogen interactions on downstream adhesion and activation. *Biomater.* **2012,** *33*, 1255.

251. Soman, P.; Rice, Z.; Siedlecki, C. A. Immunological identification of fibrinogen in dual-component protein films by AFM imaging. *Micron* **2008,** *39*, 832.

252. Okusa, H.; Kurihara, K.; Kunitake, T. Chemical modification of molecularly smooth mica surface and protein attachment. *Langmuir* **1994,** *10*, 3577.

253. Kasemo, B. Biological surface science. *Surf. Sci.* **2002,** *500*, 656.

254. Averett, L. E.; Schoenfisch, M. H. Atomic force microscope studies of fibrinogen adsorption. *Analyst* **2010,** *135*, 1201.

255. Lal, R.; John, S. A. Biological applications of atomic force microscopy *Am. J. Physiol.* **1994,** *266*, C1.

256. Santos, N. C.; Castanho, M. An overview of the biophysical applications of atomic force microscopy. *Biophys. Chem.* **2004,** *107*, 133.

257. Tunc, S.; Maitz, M. F.; Steiner, G.; Vazquez, L.; Pham, M. T.; Salzer, R. In situ conformational analysis of fibrinogen adsorbed on Si surfaces. *Colloid Surface B* **2005,** *42*, 219.

258. Agnihotri, A.; Siedlecki, C. A. Time-dependent conformational changes in fibrinogen measured by atomic force microscopy. *Langmuir* **2004,** *20*, 8846.

259. Xu, L. C.; Siedlecki, C. A. Atomic force microscopy studies of the initial interactions between fibrinogen and surfaces. *Langmuir* **2009,** *25*, 3675.

260. Yermolenko, I. S.; Lishko, V. K.; Ugarova, T. P.; Magonov, S. N. High-resolution visualization of fibrinogen molecules and fibrin fibers with atomic force microscopy. *Biomacromolecules* **2011,** *12*, 370.

261. Saner, C. K.; Lusker, K. L.; LeJeune, Z. M.; Serem, W. K.; Garno, J. C. Self-assembly of octadecyltrichlorosilane: Surface structures formed using different protocols of particle lithography. *Beilstein J Nanotechnol.* **2012,** *3*, 114.

262. Li, J.-R.; Garno, J. C. Elucidating the role of surface hydrolysis in preparing organosilane nanostructures via particle lithography. *Nano Lett.* **2008,** *8*, 1916.

263. Uosaki, K.; Quayum, M. E.; Nihonyanagi, S.; Kondo, T. Decomposition processes of an organic monolayer formed on Si(111) via a silicon-carbon bond induced by exposure to UV irradiation or ozone. *Langmuir* **2004,** *20*, 1207.

264. Zhang, X. C.; Kumar, S.; Chen, J. H.; Teplyakov, A. V. Covalent attachment of shape-restricted DNA molecules on amine-functionalized Si(111) surface. *Surf. Sci.* **2009,** *603*, 2445.

265. Necas, D. K. Gwyddion 2.25. http://gwyddion.net/.

266. Wilxox, C. *ImageTool*, University of Texas Health Science Center (UTHSCSA): San Antonio, TX, 1996.

267. Hu, M. H.; Noda, S.; Okubo, T.; Yamaguchi, Y.; Komiyama, H. Structure and morphology of self-assembled 3-mercaptopropyltrimethoxysilane layers on silicon oxide. *Appl. Surf. Sci.* **2001,** *181*, 307.

268. Jo, S.; Park, K. Surface modification using silanated poly(ethylene glycol)s. *Biomater.* **2000,** *21*, 605.

269. Prime, K. L.; Whitesides, G. M. Adsorption of proteins onto surfaces containing end-attached oligo(ethylene oxide) - a model system using self-assembled monolayers. *J. Am. Chem. Soc.* **1993,** *115*, 10714.

270. Chapman, R. G.; Ostuni, E.; Takayama, S.; Holmlin, R. E.; Yan, L.; Whitesides, G. M. Surveying for surfaces that resist the adsorption of proteins. *J. Am. Chem. Soc.* **2000,** *122*, 8303.

271. Ostuni, E.; Chapman, R. G.; Liang, M. N.; Meluleni, G.; Pier, G.; Ingber, D. E.; Whitesides, G. M. Self-assembled monolayers that resist the adsorption of proteins and the adhesion of bacterial and mammalian cells. *Langmuir* **2001,** *17*, 6336.

272. Holmlin, R. E.; Chen, X.; Chapman, R. G.; Takayama, S.; Whitesides, G. M. Zwitterionic SAMs that resist nonspecific adsorption of protein from aqueous buffer. *Langmuir* **2001,** *17*, 2841.

273. Luk, Y.-Y.; Kato, M.; Mrksich, M. Self-assembled monolayers of alkanethiolates presenting mannitol groups are inert to protein adsorption and cell attachment. *Langmuir* **2000,** *16*, 9604.

274. Ostuni, E.; Chapman, R. G.; Holmlin, R. E.; Takayama, S.; Whitesides, G. M. A survey of structure–property relationships of surfaces that resist the adsorption of protein. *Langmuir* **2001,** *17*, 5605.

275. Herrwerth, S.; Eck, W.; Reinhardt, S.; Grunze, M. Factors that determine the protein resistance of oligoether self-assembled monolayers – Internal hydrophilicity, terminal hydrophilicity, and lateral packing density. *J. Am. Chem. Soc.* **2003,** *125*, 9359.

276. Yermolenko, I. S.; Gorkun, O. V.; Fuhrmann, A.; Podolnikova, N. P.; Lishko, V. K.; Oshkadyerov, S. P.; Lord, S. T.; Ros, R.; Ugarova, T. P. The assembly of nonadhesive fibrinogen matrices depends on the alpha C regions of the fibrinogen molecule. *J. Biol. Chem.* **2012,** *287*, 41979.

277. Steiner, G.; Tunc, S.; Maitz, M.; Salzer, R. Conformational changes during protein adsorption. FT-IR spectroscopic imaging of adsorbed fibrinogen layers. *Anal. Chem.* **2007,** *79*, 1311.

278. Yermolenko, I. S.; Fuhrmann, A.; Magonov, S. N.; Lishko, V. K.; Oshkadyerov, S. P.; Ros, R.; Ugarova, T. P. Origin of the nonadhesive properties of fibrinogen matrices probed by force spectroscopy. *Langmuir* **2010,** *26*, 17269.

279. Ronda, C. R.; Jüstel, T.; Nikol, H. Rare earth phosphors: fundamentals and applications. *J. Alloy Comp.* **1998,** *275–277*, 669.

280. Trovarelli, A. Catalytic properties of ceria and CeO_2-containing materials. *Catal. Rev.* **1996,** *38*, 439.

281. Rosynek, M. P. Catalytic properties of rare-earth oxides. *Catal. Rev. Sci. Eng.* **1977,** *16*, 111.

282. Koehler, W. C. Magnetic properties of rare-earth metals and alloys. *J. Appl. Phys.* **1965,** *36*, 1078.

283. Nesbitt, E. A. New permanent magnet materials containing rare-earth metals. *J. Appl. Phys.* **1969,** *40*, 1259.

284. Yan, Z.-G.; Yan, C.-H. Controlled synthesis of rare earth nanostructures. *J. Mater. Chem.* **2008,** *18*, 5046.

285. Dosev, D.; Guo, B.; Kennedy, I. M. Photoluminescence of Eu^{3+}: Y_2O_3 as an indication of crystal structure and particle size in nanoparticles synthesized by flame spray pyrolysis. *J. Aerosol Sci.* **2006,** *37*, 402.

286. Niu, Z.; Li, Y. Removal and utilization of capping agents in nanocatalysis. *Chem. Mat.* **2014,** *26*, 72.

287. Thomson, T.; Lee, S. L.; Toney, M. F.; Dewhurst, C. D.; Ogrin, F. Y.; Oates, C. J.; Sun, S. Agglomeration and sintering in annealed FePt nanoparticle assemblies studied by small angle neutron scattering and X-ray diffraction. *Phys. Rev. B* **2005,** *72*, 064441.

288. Thalladi, V. R.; Whitesides, G. M. Crystals of crystals: Fabrication of encapsulated and ordered two-dimensional arrays of microcrystals. *J. Am. Chem. Soc.* **2002,** *124*, 3520.

289. Wang, L.; Lee, M. H.; Barton, J.; Hughes, L.; Odom, T. W. Shape-control of protein crystals in patterned microwells. *J. Am. Chem. Soc.* **2008,** *130*, 2142.

290. Aizenberg, J.; Black, A. J.; Whitesides, G. M. Control of crystal nucleation by patterned self-assembled monolayers. *Nature* **1999,** *398*, 495.

291. Zhong, Z. Y.; Gates, B.; Xia, Y. N.; Qin, D. Soft lithographic approach to the fabrication of highly ordered 2D arrays of magnetic nanoparticles on the surfaces of silicon substrates. *Langmuir* **2000,** *16*, 10369.

292. Lyles, B. F.; Terrot, M. S.; Hammond, P. T.; Gast, A. P. Directed patterned adsorption of magnetic beads on polyelectrolyte multilayers on glass. *Langmuir* **2004,** *20*, 3028.

293. Mullen, T. J.; Zhang, M.; Feng, W.; El-khouri, R. J.; Sun, L.-D.; Yan, C.-H.; Patten, T. E.; Liu, G.-y. Fabrication and characterization of rare-earth-doped nanostructures on surfaces. *ACS Nano* **2011,** *5*, 6539.

294. Wang, S.; Sobczynski, D. J.; Jahanian, P.; Xhahysa, J.; Mao, G. A supra-monolayer nanopattern for organic nanoparticle array deposition. *ACS Appl. Mater. Interfaces* **2013,** *5*, 2699.

295. Mao, Y.; Guo, X.; Tran, T.; Wang, K. L.; Shih, C. K.; Chang, J. P. Luminescent properties of ensemble and individual erbium-doped yttrium oxide nanotubes. *J. Appl. Phys.* **2009,** *105*.

296. Pires, A. M.; Serra, O. A.; Heer, S.; Gudel, H. U. Low-temperature upconversion spectroscopy of nanosized Y_2O_3 : Er,Yb phosphor. *J. Appl. Phys.* **2005,** *98*.

297. Fard, H. R.; Becker, N.; Hess, A.; Pashayi, K.; Proslier, T.; Pellin, M.; Borca-Tasciuc, T. Thermal conductivity of Er^{+3}:Y_2O_3 films grown by atomic layer deposition. *Appl. Phys. Lett.* **2013,** *103*.

298. Eilers, H. Synthesis and characterization of nanophase yttria co-doped with erbium and ytterbium. *Mater. Lett.* **2006,** *60*, 214.

299. Hyppanen, I.; Holsa, J.; Kankare, J.; Lastusaari, M.; Pihlgren, L. Up-conversion luminescence properties of Y_2O_2S:Yb^{3+},Er^{3+} nanophosphors. *Opt. Mater.* **2009,** *31*, 1787.

300. Capobianco, J. A.; Vetrone, F.; D'Alesio, T.; Tessari, G.; Speghini, A.; Bettinelli, M. Optical spectroscopy of nanocrystalline cubic Y_2O_3 : Er^{3+} obtained by combustion synthesis. *Phys. Chem. Chem. Phys.* **2000,** *2*, 3203.

301. Anh, T. K.; Minh, L. Q.; Vu, N.; Huong, T. T.; Huong, N. T.; Barthou, C.; Strek, W. Nanomaterials containing rare-earth ions Tb, Eu, Er and Yb: preparation, optical properties and application potential. *J. Lumin.* **2003,** *102*, 391.

302. Capobianco, J. A.; Vetrone, F.; Boyer, J. C.; Speghini, A.; Bettinelli, M. Enhancement of red emission ($^4F_{9/2}$ --> $^4I_{15/2}$) via upconversion in bulk and nanocrystalline cubic Y_2O_3 : Er^{3+}. *J. Phys. Chem. B* **2002,** *106*, 1181.

303. Yin, S.; Shinozaki, M.; Sato, T. Synthesis and characterization of wire-like and near-spherical Eu_2O_3-doped Y_2O_3 phosphors by solvothermal reaction. *J. Lumin.* **2007,** *126*, 427.

304. Chandra, S.; Deepak, F. L.; Gruber, J. B.; Sardar, D. K. Synthesis, morphology, and optical characterization of nanocrystalline Er^{3+}:Y_2O_3. *J. Phys. Chem. C* **2010,** *114*, 874.

305. Wang, X.; Li, Y. D. Rare-earth-compound nanowires, nanotubes, and fullerene-like nanoparticles: Synthesis, characterization, and properties. *Chem. Eur. J.* **2003,** *9*, 5627.

306. Fang, Y. P.; Xu, A. W.; You, L. P.; Song, R. Q.; Yu, J. C.; Zhang, H. X.; Li, Q.; Liu, H. Q. Hydrothermal synthesis of rare earth (Tb, Y) hydroxide and oxide nanotubes. *Adv. Funct. Mater.* **2003,** *13*, 955.

307. Mao, J.; Huang, R.; Ostroumov, K. L.; Wang, J. P.; Chang, J. Synthesis and Luminescence Properties of Erbium-Doped Y_2O_3 Nanotubes. *J. Phys. Chem. C* **2008,** *112*, 2278.

308. De, G. H.; Qin, W. P.; Zhang, J. S.; Zhang, J. H.; Wang, Y.; Cao, C. Y.; Cui, Y. Upconversion luminescence properties of Y_2O_3 : Yb^{3+}, Er^{3+} nanostructures. *J. Lumin.* **2006,** *119*, 258.

309. Tang, Q.; Liu, Z. P.; Li, S.; Zhang, S. Y.; Liu, X. M.; Qian, Y. T. Synthesis of yttrium hydroxide and oxide nanotubes. *J. Cryst. Growth* **2003,** *259*, 208.

310. Zhenxiu, X.; Zhanglian, H.; Qichao, Z.; Lixia, P.; Pengyue, Z. Preparation and luminescence properties of Y_2O_3: Eu^{3+} nanorods via post annealing process. *J. Rare Earth* **2006,** *24*, 111.

311. Nelson, J. A.; Brant, E. L.; Wagner, M. J. Nanocrystalline Y_2O_3 : Eu phosphors prepared by alkalide reduction. *Chem. Mat.* **2003,** *15*, 688.

312. Wu, G. S.; Lin, Y.; Yuan, X. Y.; Xie, T.; Cheng, B. C.; Zhang, L. D. A novel synthesis route to Y_2O_3 :Eu nanotubes. *Nanotechnol.* **2004,** *15*, 568.

313. Pang, Q.; Shi, J. X.; Liu, Y.; Xing, D. S.; Gong, M. L.; Xu, N. S. A novel approach for preparation of Y_2O_3 : Eu^{3+} nanoparticles by microemulsion-microwave heating. *Mat. Sci. Eng. B-Solid* **2003,** *103*, 57.

314. Lee, M. H.; Oh, S. G.; Yi, S. C. Preparation of Eu-doped Y_2O_3 luminescent nanoparticles in nonionic reverse microemulsions. *J. Colloid Interface Sci.* **2000,** *226*, 65.

315. Hirai, T.; Orikoshi, T.; Komasawa, I. Preparation of Y_2O_3 : Yb,Er infrared-to-visible conversion phosphor fine particles using an emulsion liquid membrane system. *Chem. Mat.* **2002,** *14*, 3576.

316. Venkatachalam, N.; Yamano, T.; Hemmer, E.; Hyodo, H.; Kishimoto, H.; Soga, K. Er^{3+} - Doped Y_2O_3 nanophosphors for near-infrared fluorescence bioimaging applications. *J. Am. Ceram. Soc.* **2013,** *96*, 2759.

317. Silver, J.; Martinez-Rubio, M. I.; Ireland, T. G.; Fern, G. R.; Withnall, R. The effect of particle morphology and crystallite size on the upconversion luminescence properties of erbium and ytterbium co-doped yttrium oxide phosphors. *J. Phys. Chem. B* **2001,** *105*, 948.

318. Zhang, J.; Wang, S. W.; Rong, T. J.; Chen, L. D. Upconversion luminescence in Er^{3+} doped and Yb^{3+}/Er^{3+} codoped yttria nanocrystalline powders. *J. Am. Ceram. Soc.* **2004,** *87*, 1072.

319. Rajasekharan, V. V.; Buttry, D. A. Electrochemical synthesis of yttrium oxide nanotubes. *Chem. Mat.* **2006,** *18*, 4541.

320. Zhang, J. L.; Hong, G. Y. Synthesis and photoluminescence of the Y_2O_3 : Eu^{3+} phosphor nanowires in AAO template. *J. Solid State Chem.* **2004,** *177*, 1292.

321. Yang, L.; Tang, Y.; Chen, X.; Li, Y.; Cao, X. Synthesis of Eu^{3+} doped Y_2O_3 nanotube arrays through an electric field-assisted deposition method. *Mater. Chem. Phys.* **2007,** *101*, 195.

322. Dragoo, A. L.; Domingues, L. P. Preparation of high-density ceria-yttria ceramics. *J. Am. Ceram. Soc.* **1982,** *65*, 253.

323. Delamarche, E.; Bernard, A.; Schmid, H.; Michel, B.; Biebuyck, H. Patterned delivery of immunoglobulins to surfaces using microfluidic networks *Science* **1997,** *276*, 779.

324. Jackman, R. J.; Duffy, D. C.; Ostuni, E.; Willmore, N. D.; Whitesides, G. M. Fabricating large arrays of microwells with arbitrary dimensions and filling them using discontinuous dewetting. *Anal. Chem.* **1998,** *70*, 2280.

325. Wasserman, S. R.; Tao, Y. T.; Whitesides, G. M. Structure and reacitivity of alkylsiloxane monolayers formed by reactions of alkyl trichlorosilanes on silicon substractes. *Langmuir* **1989,** *5*, 1074.

326. Wen, K.; Maoz, R.; Cohen, H.; Sagiv, J.; Gibaud, A.; Desert, A.; Ocko, B. M. Postassembly chemical modification of a highly ordered organosilane multilayer: New insights into the structure, bonding, and dynamics of self-assembling silane monolayers. *ACS Nano* **2008,** *2*, 579.

327. Kim, H. K.; Lee, J. P.; Park, C. R.; Kwak, H. T.; Sung, M. M. Thermal decomposition of alkylsiloxane self-assembled monolayers in air. *J. Phys. Chem. B* **2003,** *107*, 4348.

APPENDIX A: LETTERS OF PERMISSION

Publication Cooperation

1 message

Nova.Main@novapublishers.com <Nova.Main@novapublishers.com> Mon, Apr 28, 2014 at 8:17 AM

To: Lauren Englade <lengla5@tigers.lsu.edu>

Dear Dr. Englade-Franklin,

Good day. Thank you for your email message. We are happy to grant you permission to use the material free of charge in dissertation provided a credit to Nova is given each time.

Nova Science Publishers Credit Line Information

[Reprinted from: publication, title, vol. number, title of article/chapter, page numbers, copyright (year) and author(s). The statement, with permission from Nova Science Publishers, Inc. should also be noted].

Sincerely,
Stella Rosa

Administrative Assistant to Nadya Gotsiridze-Columbus
Nova Science Publishers, Inc.
400 Oser Avenue, Suite 1600
Hauppauge, NY 11788 USA
Tel: 631- 231-7269, Fax: 631-231-8175
Nova.Main@novapublishers.com

At 10:46 AM 4/25/2014, Lauren Englade wrote:

Dear Nova Publishers,

I am requesting a letter of permission to reprint from Nova Publishers on the chapter I have written for the book entitled Atomic Force Miscroscopy: Principles, Modes of Operation and Limitations - Chapter 3 entitled -

Dynamic Magnetic Characterizations at the Nanoscale: A New Mode for AFM Imaging with Magnetic Sample Modulation (MSM-AFM)
(Lauren E. Englade-Franklin, Wilson K. Serem, Stephanie L. Daniels, and Jayne C. Garno, Department of Chemistry, Louisiana State University, Baton Rouge, LA, USA)

I would like to include the chapter in my dissertation to be submitted to Louisiana State University in both print and electronic format. Please advise if there are any additional forms that need to be submitted.

Thank you for your time.

Best regards,
Lauren

RE: Highwire Press Permissions Request

1 message

Permissions <permissions@royalsociety.org> Fri, Apr 25, 2014 at 6:28 AM
To: "lengla5@lsu.edu" <lengla5@lsu.edu>

The Royal Society is pleased to grant permission for use of the material below, subject to the following conditions:

1. Full acknowledgement is given to the original source, with full details of the author(s), title, figure/page numbers, year of publication and the publisher.
2. The permission of the author(s) or the author's estate is obtained where practical.
3. The material is to be used only as described in your email and this permission is granted for one-time use only.

Yours sincerely

Jennifer
Editorial Administrator

_____

From: lengla5@lsu.edu <lengla5@lsu.edu>
Sent: 24 April 2014 19:28
To: Permissions; undefined@hwmaint14.highwire.org
Subject: Highwire Press Permissions Request

Citation:Englade-Franklin et al. 3 (3)
Journal:Interface Focus

Requester information:
Firstname: Lauren
Lastname: Englade-Franklin
Telephone:
Fax number:
Email: lengla5@lsu.edu Address:
Description: I would appreciate your permission to use this material as part of my Ph.D dissertation which will be in print and electronic format from Louisiana State University.

APPENDIX B: PARTICLE LITHOGRAPHY USING UV/OZONE TREATMENT

An approach for preparing surface nanopatterns was developed (Chapter 5) for preparing samples with reactive organosilanes such as PEG-silane. Often the headgroups of organosilanes react with molecules selected for surface patterning to form disorganized structures. The steps described as follows will enable surface patterning of SAMs with reactive endgroups.

Steps for critical cleaning of silicon substrates

1. Wash pieces of precut silicon wafers using deionized water (18 MΩ). Dry the substrates using ultrapure argon, and place them in a clean glass jar. Make sure the substrates are separated from each other, and do not touch. The polished side of the wafer should be placed face up in the jar.
2. Do this step in a laboratory fume hood. While wearing acid-resistant gloves and safety glasses, measure 9 mL of concentrated sulfuric acid and add to the jar. Add 3 mL of 30 % hydrogen peroxide to the jar and immediately place a cap on the jar. Soak the substrates in the piranha solution for 1.5 h. Piranha solution is highly reactive and should be prepared in the hood using protective clothing. It is critical that silicon substrates be cleaned before to organosilane deposition. The piranha cleaning solution removes organic contaminants and facilitates the formation of an oxide layer.
3. Using tweezers, remove the substrates from the solution, rinse with copious amounts of deionized water, and store in deionized water. Samples should be used the same day when cleaned.

Deposition of an organosilane thin film via heated vapor deposition

4. Rinse substrates with water and dry with ultrapure argon. Place the substrates in a plastic vessel containing 400 µL neat mercaptopropyltrimethoxysilane (MPTMS) (or whichever

silane is chosen for areas inside the nanopores). Make sure the substrate does not come into physical contact with the neat silane solution (you can use an aluminum weigh boat or aluminum foil to make a tray for isolating the liquid from the substrate). To generate a vapor, place the sample in a 70 C oven for 4 h. This step will generate a thin film of organosilane on the substrate. When using MPTMS, sulfhydryl groups with be present at the interface after heated vapor deposition.

5. Remove the sample from the vessel using tweezers and rinse with copious amounts of ethanol. Sonicate the substrate in a fresh ethanol solution for 15 min and dry with ultrapure argon. Samples are now ready for deposition of a mesosphere mask.

Steps for washing the silica mesoparticles

6. Using a micropipette, measure a volume of the mesoparticle suspension needed for the number of substrates to be patterned (about 20 µL per substrate). Place the solution in a 1.5 mL centrifuge tube and fill the tube with deionized water. Gently vortex the solution to mix the beads with the water. Prepare a counterbalance centrifuge tube containing an equivalent volume of water.
7. Centrifuge the suspension for 10 min at 16,000 rpm. Discard the supernatant and refill the tube with water. Gently vortex the solution to resuspend the mesospheres.
8. Repeat the cycle three times. This step removes residual surfactants and charge stabilizers present in the original solution of mesoparticles.
9. After the final centrifuging step, resuspend the silica particles in deionized water using the original sample volume from beginning in step 6. The final concentration of the silica particles will remain unchanged from the commercially available concentration.

Generation of the mesosphere mask

10. Deposit 10 µL of the silica particles onto the MPTMS covered substrate (for the Ted Pella 5×5 mm substrates) making sure the coverage is even. A greater volume may be needed for larger substrates. Dry the sample at 4 C overnight (~ 15 h). Dry the mask at a lower temperature to slow the evaporation of water to enable better packing of the silica beads on the MPTMS film.

Deposition of the matrix silane film

11. After removing the sample from the refrigerator, place it in the UV-ozone generator for 20 min to oxidize the unmasked areas of the MPTMS film. Areas directly in contact with the silica particles are protected from oxidation during irradiation.
12. After removing the sample from the UV-ozone generator, immediately place the sample in a glass jar containing a 1 % solution of PEG-silane in toluene (or whichever silane desired for the matrix). Leave the sample in the organosilane solution for 5 h.

Removal of the template

13. Using tweezers remove the samples from the glass jar and immediately rinse with copious amounts of deionized water. Sonicate the sample in ethanol for 3 min.
14. Sonicate the samples in fresh ethanol for 10 min. Continue to change solutions alternating from ethanol to water every 10 min. Continue to do this until the mask is completely removed (usually 3-5 washes). The last sonication step should be done in water.
15. After drying, the samples are ready for imaging.

APPENDIX C: SURFACE-TEMPLATING METHOD FOR SYNTHESIZING RARE EARTH OXIDE NANOPARTICLES

An approach for preparing surface arrangements of rare earth oxide (REO) nanoparticles was developed (Chapter 6) using surface templates of organosilane nanopatterns. The organosilane nanopatterns provided a surface mask for spatially distributing the placement of small volumes of reagents. After the solutions were dried, dried deposits of precursor salts were heated to form well-defined arrangements of REO nanocrystals.

Preparation of a stock solution of REO precursor salts

1. Heat 50 mL of concentrated nitric acid to 80 C using a hot plate in a fume hood. Dissolve 0.0075 mol of yttrium oxide in the nitric acid. Erbium oxide can be dissolved in the acid if desired (3 % doping concentration). Once the solution is clear, remove it from the hot plate and cool to room temperature.
2. Add NH_4OH until the solution registers as basic using pH paper. At alkaline pH, the yttrium hydroxide will form a precipitate in the solution. Filter the precipitate by vacuum filtration and wash with deionized water. Dry the precipitate in air to form a powder.
3. Prepare a 25 % trichloroacetic acid (TCAA) solution in water. Use this solution to prepare a saturated solution of the yttrium hydroxide powder. Add small volumes of the TCAA solution to just dissolve the yttrium hydroxide powder (~ 88 g). The saturated solution of yttrium trichloroacetate (YTCA) can be further diluted if needed.

Particle lithography procedure to prepare nanopores within a hydrophobic matrix film

Procedure for cleaning silicon substrates

4. Wash precut silicon wafers using deionized water (18 MΩ). Dry the substrates using ultrapure argon, and place the pieces into a clean glass jar.

5. Complete this step in a laboratory fume hood. While wearing acid-resistant gloves and safety glasses, add 9 mL of concentrated sulfuric acid to the jar. Carefully add 3 mL of 30 % hydrogen peroxide to the jar and place the cap on the jar quickly. Soak the substrates in the piranha solution for 1.5 h. Piranha solution is highly reactive and should be prepared in the hood using acid-resistant personal protective clothing.
6. Remove the substrates from the Piranha solution using tweezers, rinse with copious amounts of deionized water, and store in water. Samples should be used the same day as cleaned.

Steps for washing silica mesoparticles using centrifugation

7. Using a micropipette, measure a volume of the mesoparticle suspension sufficient for the number of substrates to be prepared (about 20 µL per substrate). Place the solution in a 1.5 mL centrifuge tube and fill with deionized water. Gently vortex the solution to mix the beads with water. Prepare a counterbalance centrifuge tube containing an equivalent volume of water.
8. Centrifuge the suspension for 10 min at 16,000 rpm. Discard the supernatant and refill the tube with water. Gently vortex the solution until the beads are resuspended.
9. Repeat step the washing/centrifuge cycle three times to remove residual surfactants and charge stabilizers present in the original mesoparticle suspension.
10. After the final centrifuging step, resuspend the silica particles in deionized water using the original sample volume.

Fabrication of a surface mask for nanolithography

11. Deposit 10 µL of the silica particles onto the clean silicon substrate, to ensure complete surface coverage for the 5×5 mm substrates (Ted Pella). Larger pieces of substrates will require a larger volume of sample.

12. Dry the sample in ambient conditions until it is dry in appearance (~ 4-6 h). After drying, place the substrate in a 150 C oven overnight.

Preparation of a hydrophobic resist film of organosilane

13. After removing the substrates from the oven, place the samples into a glass jar containing 0.1% octadecyltrichlorosilane (OTS) in bicyclohexyl for 7 h.
14. Remove the samples from the glass jar using tweezers and immediately rinse with copious amounts of deionized water. Sonicate the sample in ethanol for 3 min. Use fresh solvents for rinsing steps with sonication to prevent any residual OTS molecules from depositing within the nanopores after the mask is removed.
15. Sonicate the samples in fresh ethanol for 10 min. Continue to change solutions alternating from ethanol to water every 10 min. Continue rinsing the sample until the mask is completely removed (usually 3-5 washes). Complete a final rinsing and sonication step in deionized water.
16. Dry the samples with ultrapure argon, samples are then ready for AFM experiments.

Inserting the precursor solutions of yttrium salt inside the nanopores

17. Place the OTS sample into a saturated solution of yttrium in trichloroacetic acid and sonicate for 5 min. Leave the sample in the solution for up to 3 h.
18. Using tweezers, remove the sample slowly in a vertical position and place in a flat orientation to dry in a petri dish under ambient conditions. After drying, the samples are ready for AFM imaging.

Steps for solid state synthesis of yttria nanocrystals

19. Place the dried sample into an oven and set up a temperature profile.

20. The heating profile should ramp to 150 C over 2 h and hold for 3 h. Ramp at 50 C per hour to 800 C for 13 h and hold at 800 C for 8 h followed by cooling. The heating steps will convert the nanoparticles to yttria and remove the OTS film. After cooling the sample is ready for AFM imaging.

APPENDIX D: SUPPLEMENTAL INFORMATION FOR SPATIALLY SELECTIVE SURFACE PLATFORMS FOR BINDING FIBRINOGEN PREPARED BY PARTICLE LITHOGRAPHY WITH ORGANOSILANES[9]*

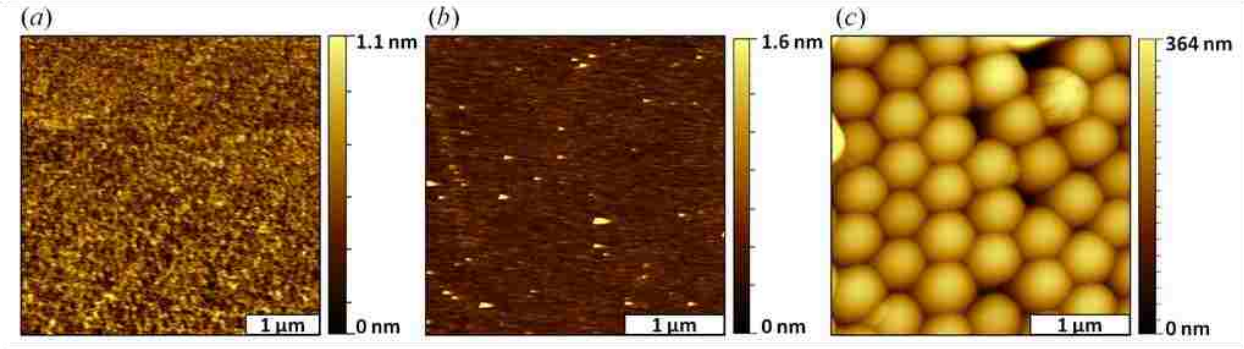

Figure D1 Control samples for steps that are not shown in the article viewed with AFM topographs. (*a*) A clean silicon substrate with a surface roughness of 0.9 nm, image was acquired in air using contact mode AFM. (*b*) After MTPMS deposition, the roughness measured 1.8 nm; image acquired with tapping-mode. (*c*) After the silica mesospheres were deposited on MPTMS film (tapping-mode image).

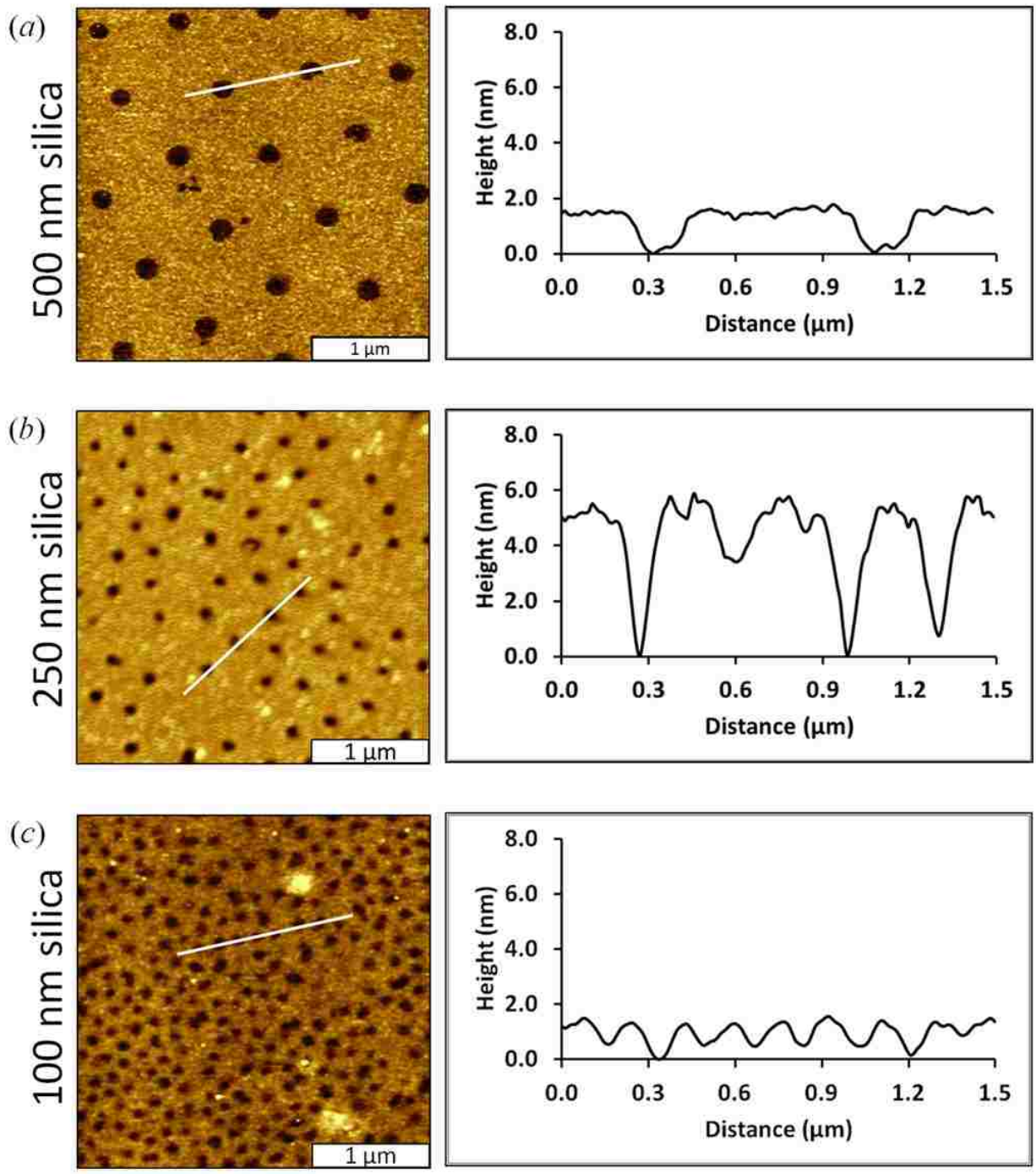

Figure D2 Representative AFM topography images and cursor profiles of organosilane nanopatterns prepared on Si(111) using different diameters of silica mesospheres. Samples were prepared using the same protocol as with Figure 3.2, the nanopores are regions with MPTMS surrounded by PEG-silane.

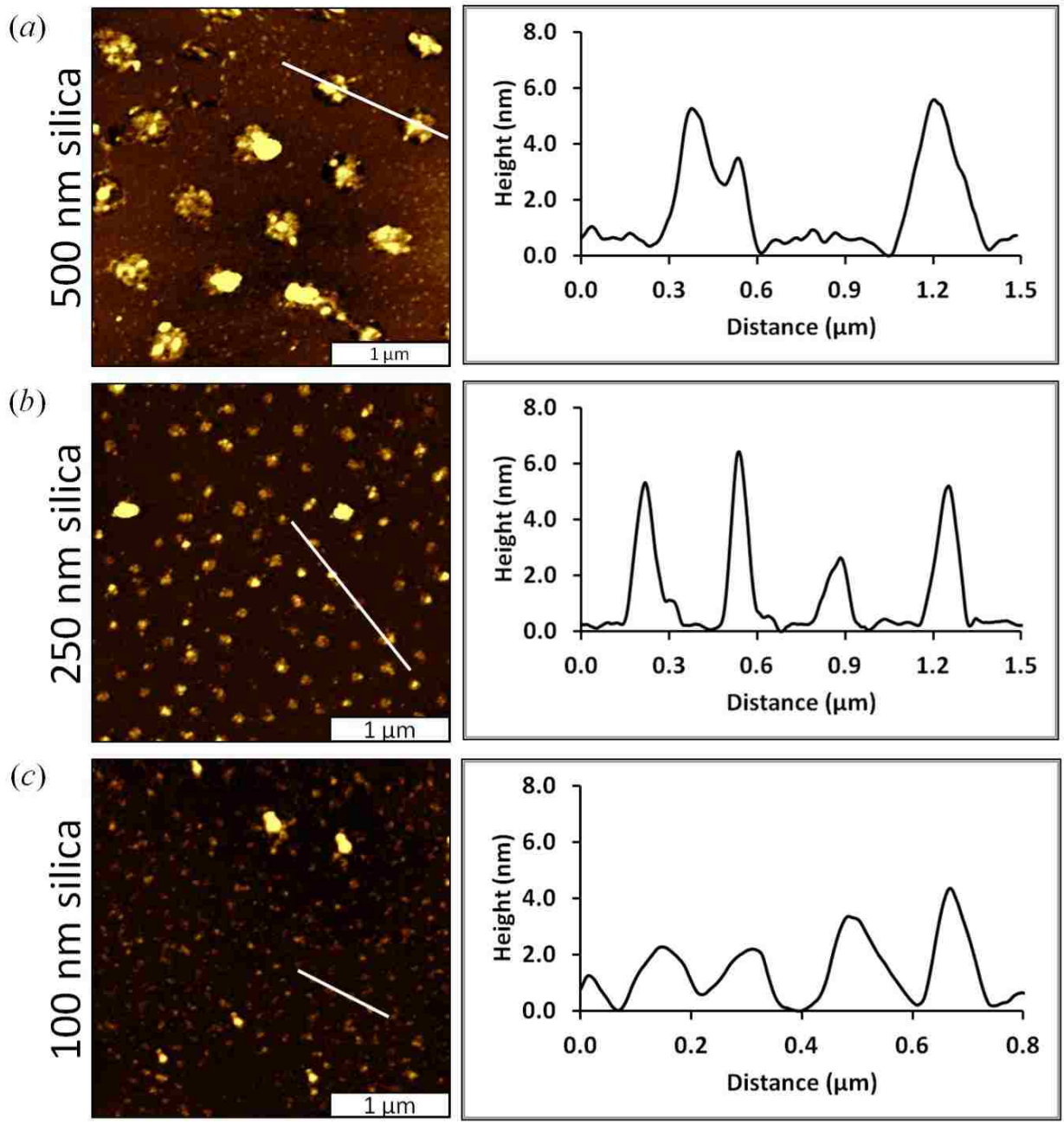

Figure D3 Representative AFM topography views of nanopatterns after coupling fibrinogen to sites with MTPMS, achieved with samples prepared using different sizes of silica mesospheres for particle lithography masks.

APPENDIX E: SUPPLEMENTAL INFORMATION FOR SURFACE-DIRECTED SYNTHESIS OF ERBIUM-DOPED YTTRIUM OXIDE NANOPARTICLES WITHIN ORGANOSILANE ZEPTOLITER CONTAINERS

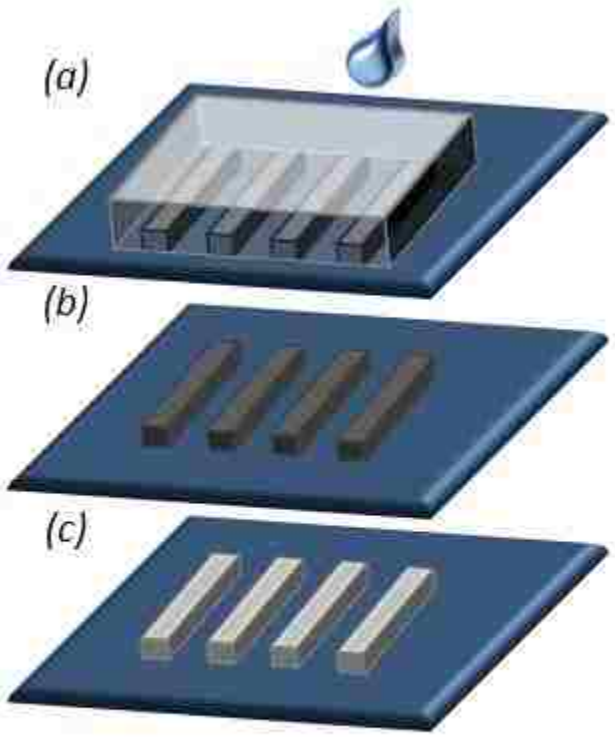

Figure E1 Steps to prepare microstructures of precursor salts using capillary filling of PDMS molds. (*a*) A PDMS mold with line micropatterns was placed on the substrate. A drop of the precursor solution was placed at the entrance of the microchannels. (*b*) After drying (~24 h), the PDMS mold was removed to reveal microline patterns of salt deposits. (*c)* Heating to 800 C converts the deposits of erbium and yttrium salts to erbium-doped yttrium oxide microstructures.

Microstructures were fabricated as a proof-of-concept to enable a convenient platform for optimizing the temperatures for the solid state synthesis of erbium-doped yttrium oxide microstructures. The Si(111) substrates were treated with UV-ozone for 20 min to remove contaminants. A polydimethysiloxane (PDMS) mold patterned with 3 μm channels was placed

on the silicon wafer (Figure E1a). The PDMS mold was fabricated by curing a film of Sylgard elastomer (Dow Corning, Midland, MI) on an AFM calibration grid (NT-MDT, Moscow, Russia). A drop of the solution of yttrium trichloroacetic acid (10 μL) was placed next to the PDMS mold near the openings of the microchannels. Within a few minutes, the liquid was drawn into the conduits by capillary force to completely fill the length of the microchannel (Figure E1a). The surfaces of the PDMS mold that are in contact with the substrate do not conduct liquid, only the open areas within the channels fill with reagents. The sample was dried in ambient conditions for 24 h. After removing the stamp, salt deposits had formed within the microchannels (Figure E1b). The sample was heated to 150 C for 3 h to decompose the acid to form $Y_2(CO_3)_3$. The carbonate was further decomposed to Y_2O_3 by heating to 800 C overnight (Figure E1c). After drying the samples, the substrate retains a micropatterned arrangement of the precursor salts according to the defined arrangement of microline patterns. Preparation of solid yttria microstructures was confirmed with X-ray powder diffraction on a Bruker AXS D8 Advance X-ray diffractometer equipped with a Cu K_α source. Data were collected over the range of 2 theta of 5 to 80 ° with step size of 0.02° at 2 s count time. The micropatterns of erbium-doped Y_2O_3 were imaged using an FEI Quanta 200 scanning electron microscope. The micron sized relief structures were used to evaluate and optimize synthetic conditions for advancing to smaller nanostructures, (e.g. temperature, duration of heating and atmosphere requirements).

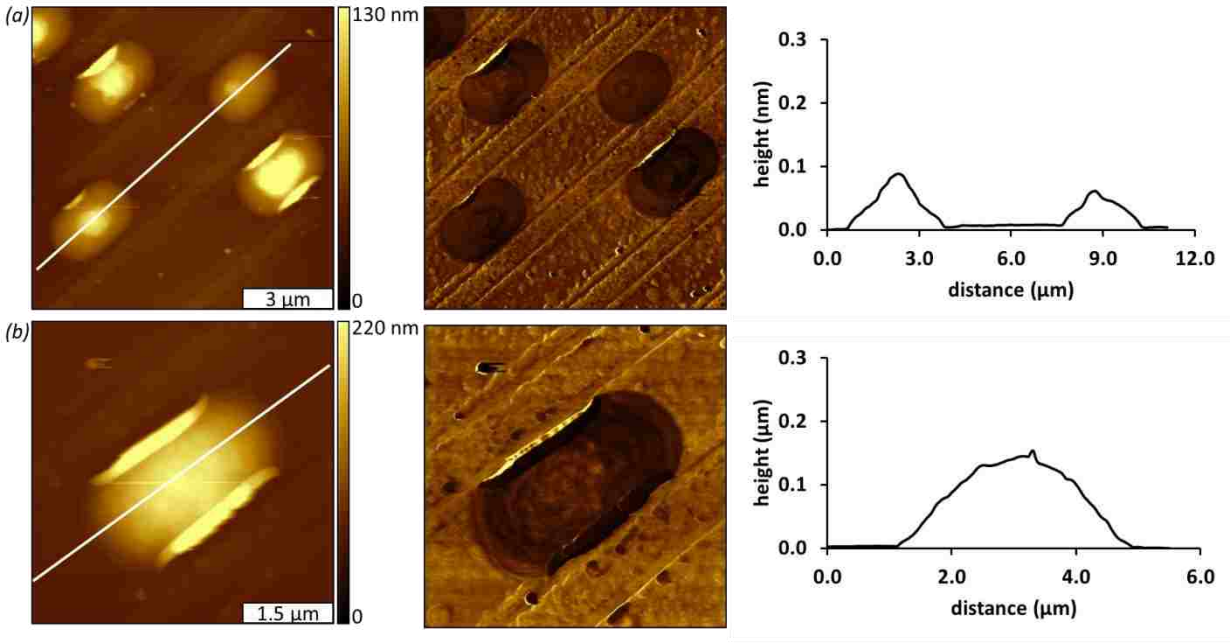

Figure E2 Microparticles of erbium-doped Y_2O_3 prepared from capillary filling after heating, imaged by contact mode AFM in air. (*a*) Four microparticles formed inside of the channels of the PDMS mold are visible in the AFM topography (left) and corresponding lateral force image (center). A cursor profile across two microparticles is shown on the right. (*b*) A single microparticle shown within a 5×5 μm^2 AFM topography frame (left); lateral force image (center); and cursor profile (right). The shape of the channels within the PDMS mold influence the geometries of the microparticles: an elongated shape was produced with flat sides formed against the walls of the channels.

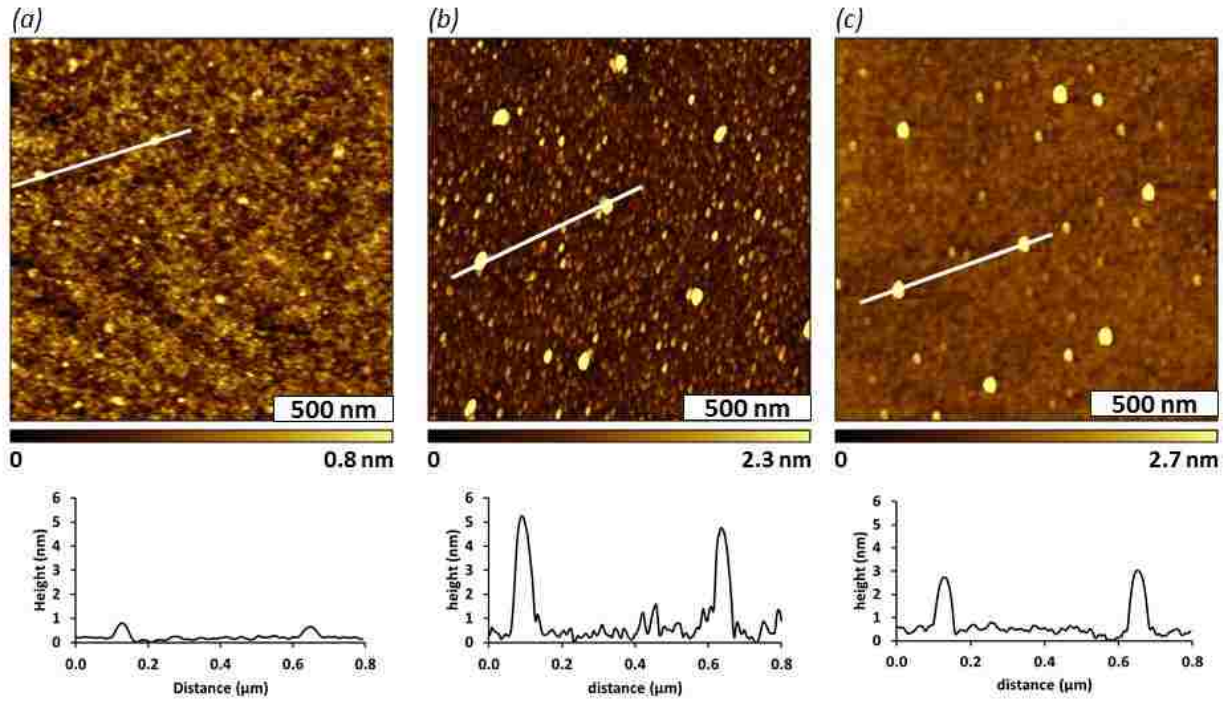

Figure E3 Nanoparticles of erbium-doped Y_2O_3 prepared at selected concentrations and immersion intervals. Organosilane nanopores were immersed in precursor salt solutions for varying times for each of the above samples. (*a*) Smaller nanoparticles were prepared at 0.05 *m* concentration, measuring 0.5 ± 0.1 nm (n = 27) after 3 h immersion. (*b*) The nanoparticles prepared from substrates soaked for 1 h in saturated salt solution measured 3.8 ± 1.1 nm in height (n = 66). (*c*) A sample soaked in saturation salt solution for 3 h produced nanoparticles with an average height of 3.1 ± 0.9 nm (n = 86).

VITA

Lauren Englade-Franklin is a native of Louisiana and was born in Lafayette, LA in 1987. Her interest in chemistry stemmed from a high school chemistry class with Mr. Don Hattier. She received her bachelor's degree in chemistry with a minor in biology from Louisiana Tech University in May 2009. During her time at Louisiana Tech, she participated in undergraduate research under Dr. Sven Eklund for one year and was selected for a short summer REU program through the LSU Health and Sciences in New Orleans. In the Fall of 2009, she began doctoral studies at Louisiana State University where she joined Dr. Jayne C. Garno's group. Thus far at LSU, Lauren has published a first author publication and a book chapter. Two additional first author mansucripts are in submission. Lauren is co-author of two publications and at least three additional shared manuscripts are in preparation. Lauren presented original research at both regional and national conferences including two talks, seven first-author poster presentations, and nine co-authored posters. Lauren directed senior thesis research for three LSU undergraduate students in chemistry. One of her undergraduates, Asenath Francis, won two poster awards for her studies with scanning probe characterizations of gold nanoparticles. Lauren has taught undergraduate laboratories at LSU for six semesters and won a Teaching Award in 2012 for the analytical instrumentation lab, the competitive TA scholar awards recognize excellence for teaching undergraduates. The degree of Doctor of Philosophy will be conferred at the Summer 2014 Commencement, Louisiana State University, Baton Rouge, LA.